Technologies for Protein Analysis and Tissue Engineering, with Applications in Cancer

Thesis by

Udi Benjamin Vermesh

In Partial Fulfillment of the Requirements

for the Degree of

Doctor of Philosophy

California Institute of Technology

Pasadena, California

2011

(Defended October 4, 2010)

A man should look for what is, and not for what he thinks should be.

-Albert Einstein

Acknowledgements

This thesis would not have been possible without the support and guidance of a multitude of mentors, colleagues, friends, and family. I would first like to thank my advisor, Jim Heath, whose big picture ideas and the drive to make a large impact on the scientific community allowed the research projects contained within this thesis to come to fruition. His scientific zeal truly inspired me. I would also like to thank Professor Paul Mischel and Dr. Tim Cloughesy for providing indispensable knowledge and for making it possible for my colleagues and me to perform clinical trials in the fight against cancer.

I would like to thank my brother and fellow graduate student, Ophir Vermesh, for working side-by-side with me every day and pushing me to achieve. I enjoyed the quality time I got to spend with my brother, and I look forward to him having a great scientific and medical career. Thanks to Jang Wook Choi for helping lead the nanofluidics project with me. He taught me the ins and outs of micro- and nanofabrication with his patient, meticulous nature and allowed me to get my bearings in the lab when I was first starting my graduate research.

I'm thankful to John Nagarah, whose creative and thorough advice helped me look at solving scientific problems in a whole new light. I also enjoyed the conversations we shared and his ability to display humor even during the tough times. I'd like to thank Rong Fan for teaching me how to develop mathematical models to describe physical phenomena in my research. His expert knowledge in nanofluidics is truly remarkable.

I would also like to thank Professor David Tirrell, Professor Mory Gharib, and Professor Robert Grubbs for agreeing to be members on my thesis committee. I would

like to thank Diane Clark Robinson and Kevin Kan for their efforts in making sure the lab always ran smoothly. I would also like to thank Tiffany Huang and Shawn Sarkaria at UCLA for facilitating the glioblastoma project, specifically for their help in determining an appropriate plasma protein panel for detecting this cancer. Thanks to my fellow graduate student colleagues Chao Ma and Kiwook Hwang for assisting me in the tissue engineering research. I'd also like to thank fellow colleagues Kaycie Butler and Ann Cheung for the light-hearted conversations we exchanged.

Finally, I'd like to thank my parents. They instilled in me virtues of hard work, decency, and a thirst for knowledge. Without their direction, I would not have become an individual capable of becoming a good scientist. Most importantly, they allowed me the freedom to choose whatever life would bring the most happiness for me.

Abstract

The first part of this thesis describes electrolyte transport through an array of 20 nm wide, 20 μm long SiO_2 nanofluidic transistors. At sufficiently low ionic strength, the Debye screening length exceeds the channel width, and ion transport is limited by the negatively charged channel surfaces. At source-drain biases > 5 V, the current exhibits a sharp, nonlinear increase, with a 20 − 50-fold conductance enhancement. This behavior is attributed to a breakdown of the zero-slip condition. Implications for peptide sequencing as well as energy conversion devices are discussed.

The next part describes a technology for the detection of the highly aggressive brain cancer glioblastoma multiforme (GBM). In general, proteomic approaches have shown great promise in recent years for correctly classifying and diagnosing cancer patients. However, no large antibody-based microarray studies have yet been conducted to evaluate and validate plasma molecular signatures for detection of glioblastoma and monitoring of its response to therapy. In this study, we compared plasma samples from 46 glioblastoma patients (72 total samples) with those of 47 healthy controls with respect to the plasma levels of 35 different proteins known to be generally associated with tumor growth, survival, invasion, migration, and immune regulation. Average-linkage hierarchical clustering of the patient data stratified the two groups effectively, permitting accurate assignment of test samples into either GBM or healthy control groups with a sensitivity and specificity as high as 90 % and 94 %, respectively (when test samples within unbiased clusters were removed). The accuracy of these assignments improved (sensitivity and specificity as high as 94 % and 96 %, respectively) when the cluster

analysis was repeated on increasingly trimmed sets of proteins that exhibited the most statistically significant ($p < 0.05$) differential expression. The diagnostic accuracy was also higher for test samples that fell into more homogeneous clusters. Intriguingly, test samples that fell within perfectly homogeneous clusters (all members belonging to the same group) could be diagnosed with 100 % accuracy. Using the same 35-protein panel, we then analyzed plasma samples from GBM patients who were treated with the chemotherapeutic drug Avastin (Bevacizumab) in an effort to stratify patients based on treatment-responsiveness. Specifically, we compared 52 samples from 25 patients who exhibited tumor recurrence with 51 samples from 21 patients who did not exhibit recurrence. Again, several proteins were highly differentially expressed and cluster analysis provided effective stratification of patients between these two groups (sensitivity and specificity of 90 % and 96 %, respectively).

Finally, single-cell resolution patterning of tissue engineered structures is demonstrated. The proper functioning of engineered constructs for tissue and organ transplantation requires positioning different cell types in anatomically precise arrangements that mimic their configurations in native tissues. Toward this end, microfabrication strategies have facilitated great strides in cell micropatterning in recent years, but these technologies are still limited in that they can typically only pattern one or two cell types at a time with feature sizes that are larger than a single cell. We present a patterning methodology that allows for high-density, multiplexed patterning of distinct cell types on glass at single-cell resolution. The technique involves two microfluidic-patterning steps run perpendicularly to each other in which “anchor” oligos are first laid down on a polylysine-coated glass substrate followed by binding of “bridging” oligos

containing both an anchor-complementary sequence and a unique sequence that can bind to an oligo-functionalized cell. In this manner, dense arrays of 3 x 3 and 3 x 1 DNA grids can be patterned and then converted into cell arrays. As a proof-of-concept, both a neuron-astrocyte construct and a pancreatic islet construct containing 2 distinct islet cell types were patterned separately as a dense array of cell grids. Once fixed in a hydrogel matrix, layers of patterned cells were then stacked to form 3-D tissue engineered constructs.

Table of Contents

List of Figures and Tables

Chapter 1

Chapter 2

Chapter 3

Chapter 4

Chapter 1

Introduction

1.1 Protein Analysis and Proteomics

The last decade has witnessed substantial advancements in technologies developed for faster and more comprehensive protein sequencing[1-3], analysis of protein structure and function[4,5], and profiling of proteins involved in human diseases such as cancer[6-8]. Efforts to determine increasingly complex sequences and structures of proteins within a rapid timeframe have been led by improvements in mass spectrometry[6,9], a technology that has proven far superior to the days when the Edman Degradation was the only method for sequencing peptides. To help gain insight into the molecular basis of diseases, technologies such as the enzyme-linked immunosorbent assay (ELISA)[10], and gel chromatography[11], as well as mass spectrometry, have allowed for the analysis of large amounts of protein data, proving indispensable in detecting protein expression from human tissue and blood. Indeed, the field of proteomics owes its existence to these technologies.

However, the shortcomings of these analytical devices are beginning to be realized as the need for measuring ever increasing amounts of biological information will require higher throughput and lower cost processes. As such, the field has pushed toward miniaturization of these technologies to the micro- and nanoscale[7,12]. Using inexpensive, yet robust materials to build biochips will allow information on protein sequences, structures, and functions to increase by orders of magnitude. At the same time, these analyses would occur a great deal faster than current methods allow.

These microchip technologies would also boost large scale proteomic studies, which would be especially useful in treating cancer, since gaining information about the disease depends on understanding interactions between many proteins[13,14]. For example, the rapid detection of the levels of thousands of human blood proteins at low cost could be realized in a minimally invasive at home diagnostic device for the early detection of cancer. By the same token, a related device could help diagnose a multitude of diseases in the third world, where access to healthcare is limited.

In both the academic setting and the biotechnology industry, processes that require entire laboratories could be scaled down to the size of a chip. At the same time, the extensive parallelization enabled by such small devices would vastly increase throughput.

1.2 Nanoscale Protein Sequencing Devices

As researchers have worked on elucidating the structures and functions of proteins, simple nanoscale devices have been designed toward sequencing these proteins faster and more efficiently, without the need for fluorescent labels and expensive optical devices for imaging. Some examples of these contraptions include fabricated nanopores[15-17] (**Figure 1.1**) and nanofluidic channels[18-20] (**Figure 1.2**), as well as synthetic and naturally occurring nanoporous materials integrated into new designs[21] (**Figure 1.3**).

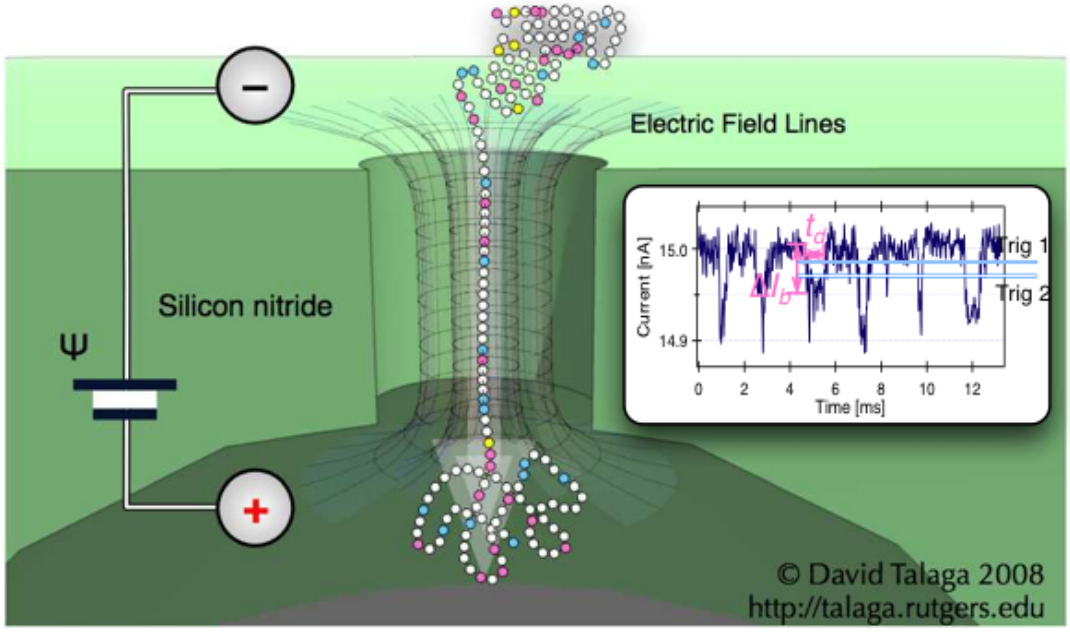

Figure 1.1. Schematic of a nanopore measurement. Single proteins translocating through the nanopores decrease the conductivity by replacing electrolyte. This is detected by a transient drop in current as illustrated by the inset. The levels present during an event and their duration are analyzed to determine the size, shape, and charge of the protein. *Courtesy of the Talaga Group, Dept. of Chemistry and Chemical Biology, Rutgers.*

Metal electrodes are usually attached to either side of the nanopores or nanochannels, and voltage biases between the electrodes modulate the electric field within. As these technologies are refined, it is anticipated that the interaction of the

electric field with charges along an unknown biomolecule could result in an electrical readout that would identify the analyte. Multiple efforts are currently underway on using these devices to sequence DNA molecules rapidly and in real time, with the expectation that entire genomes could be sequenced at low cost. The personal genetic codes obtained could advance personalized medicine by the creation of new drugs capable of treating far more specific illnesses, and they could help determine a person's predisposition to particular diseases.

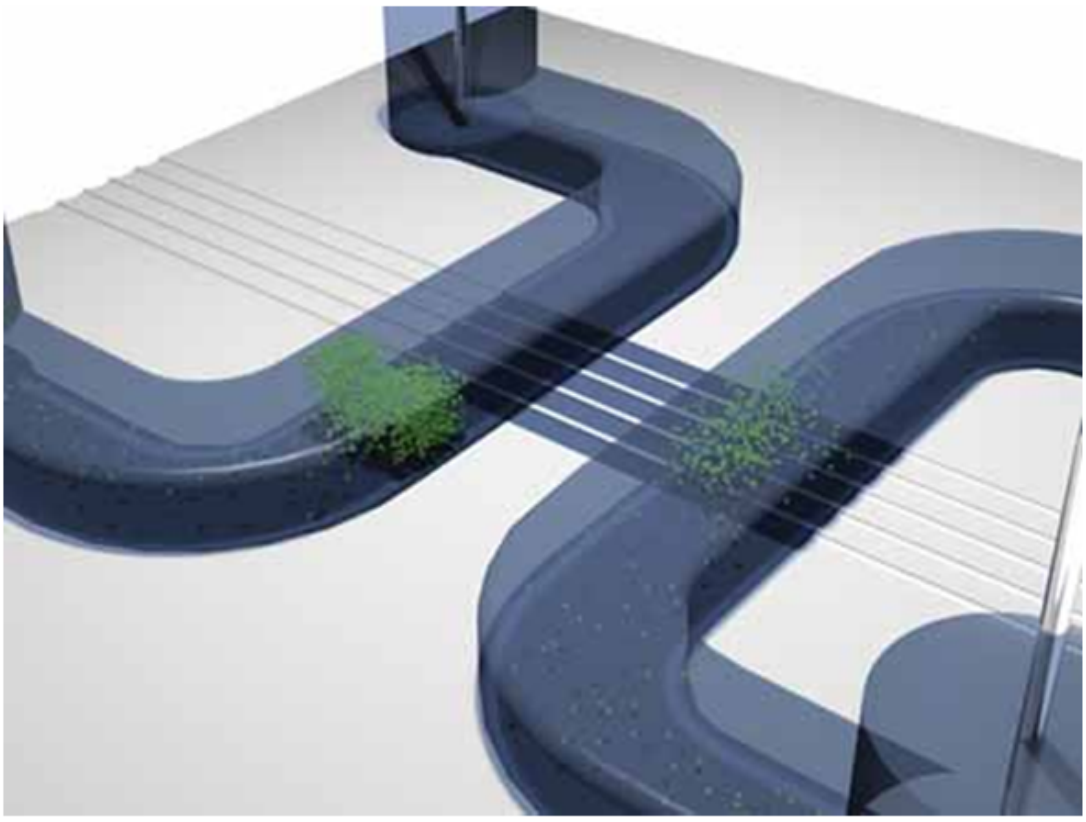

Figure 1.2. Schematic of an array of nanofluidic channels. Multiple nanochannels are positioned between two microfluidic channels. By inserting an electrically charged analyte into the fluidic system, current can be read across the nanochannels when a voltage is applied. Adapted from Adv. Mater. **2008**, 20, 3011–3016.

However, as research into personalized medicine has progressed, it has moved toward identifying protein signatures to diagnose human diseases. Accordingly, in the near future, protein sequencing devices will have to follow suit and find applications in the analysis of proteins rather than DNA.

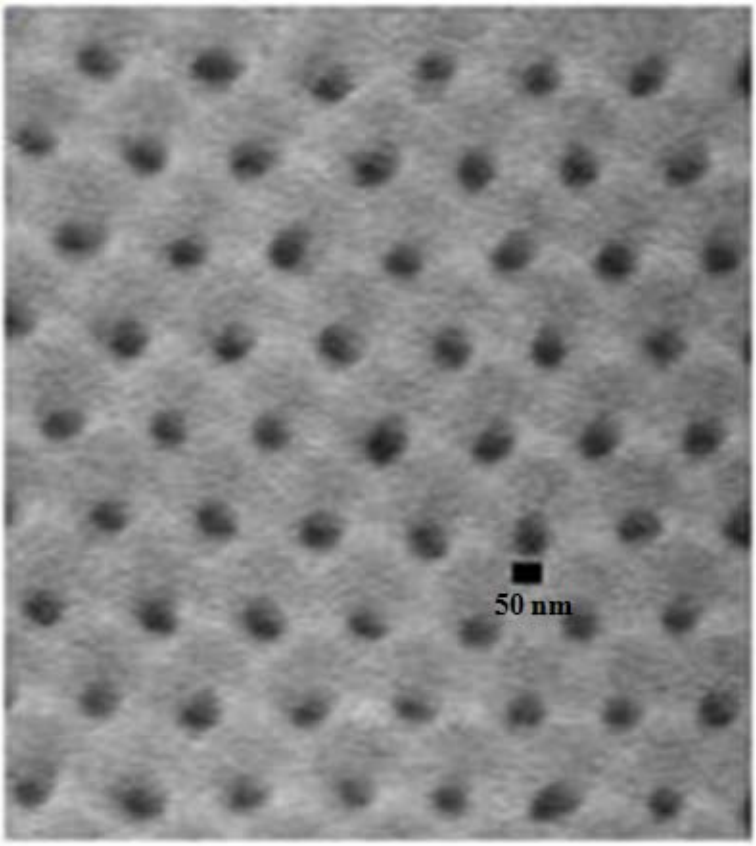

Figure 1.3. Nanoporous material sample. A dense matrix of well oriented porous channels in aluminum oxide is shown. *Courtesy of the Shpyrko Group, Dept. of Physics, UCSD.*

1.3 Plasma Protein Profiling for the Detection of Cancer

The rapid expansion of the field of proteomics has made it necessary to develop technologies capable of analyzing complex proteomes, specifically the levels and interactions of differentially expressed proteins in the human body. In particular, the ability to measure these on a systemic level in a noninvasive and cost-effective manner has brought great interest to the detection of cancer biomarkers found in the blood[22-25].

The current gold standard for the high sensitivity identification and measurement of proteins found in plasma, the blood component in which proteins are dissolved, is the sandwich ELISA[26]. In this assay, a layer of capture antibodies specific to the antigen of interest adheres to a solid support, usually contained within a 96 well microtiter plate. Another layer of detection antibodies conjugated to an enzyme "sandwiches" the antigen, and the addition of an enzyme substrate quantifies the level of antigen. Although the standard ELISA exhibits great sensitivity, its drawback is that it can only measure a relatively small number of analytes, as each well is devoted to one protein. Therefore, its limitations in cancer diagnostics are becoming more apparent as most cancers are now known to affect large panels of proteins rather than any single marker.

The recent advent of multiplexed platforms for protein detection, such as antibody microarrays (**Figure 1.4**), has shown great promise for large scale plasma protein profiling[6,26-28]. The method of detection is similar to the ELISA, as antigens are sandwiched between two layers of antibodies. However, the capture antibodies are immobilized on-chip, using either microarray spotters or microfluidic flow patterning, to create spots a few hundred microns in diameter. Thus, it is possible to create hundreds of separate protein detection regions in an area equal to that of a typical ELISA well. Furthermore, the detection antibodies can be conjugated to fluorescent molecules or covalently linked to nanoparticles, resulting in even higher sensitivity. Streamlined variations of such multiplexed devices will prove vital in the early stage detection of multiple types of cancer.

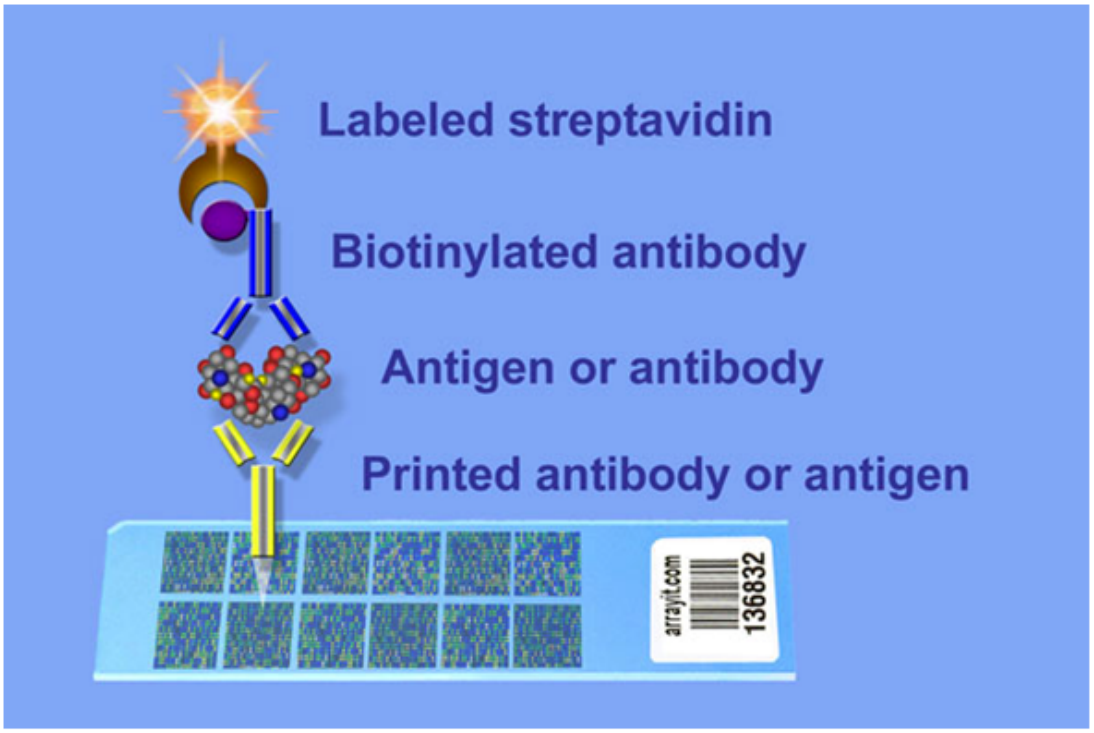

Figure 1.4. Antibody microarray. Capture antibodies are first printed onto a glass substrate , resulting in spots a few hundred microns in diameter. All subsequent steps are identical to those performed in an ELISA with the exception that a fluorescent signal is used to quantify the antigen rather than an enzymatic reaction. *Courtesy of Arrayit Corporation.*

1.4 Thesis Synopsis

The overall theme of this thesis centers on the development of new technologies for high throughput analysis of proteins. Chapter 2 begins with a description of the construction of silica nanofluidic channels using semiconductor fabrication methods and concludes with their applications to peptide sequencing. The entire nanochannel device consists of an array of 20 nm-wide, 20 μm-long channels in close proximity to a gate electrode along with microfluidic channels that cross perpendicularly at the nanochannel ends. Ionic solutions, such as potassium chloride (KCl), and peptide solutions, such as polylysine and polyaspartate, are flowed into the device, and source-drain biases are

applied across the nanochannels to study the characteristics of the current produced by the particular charged species. For KCl, at sufficiently low ionic strength, the Debye screening length exceeds the channel width, and ion transport is limited by the negatively charged silica channel surfaces so that only positively charged species can flow through the channels. At source-drain biases > 5 V, the current exhibits a sharp, nonlinear increase, with a 20 – 50-fold conductance enhancement. This behavior is attributed to a breakdown of the zero-slip condition. This phenomenon results in amino acid specific I-V traces when aspartate and lysine monomer solutions are added separately, which shows great promise for the use of nanofluidic channel devices for high throughput protein sequencing and structure determination. Chapter 2 has been taken in part from © *Nano Lett.*, **2009**, 9(4), 1315-1319[29].

Chapter 3 delves into the field of proteomics and presents a diagnostic device for the detection of differentially expressed proteins in the blood of patients with glioblastoma multiforme (GBM), the most common and aggressive class of brain cancer in humans. The device architecture improves on recently developed antibody microarrays in terms of device stability and longevity and consists of DNA encoded antibody libraries (DEAL), whereby orthogonal sets of anchor single-stranded DNA oligomers are spotted onto polylysine borosilicate slides and their complementary oligomers are conjugated to antibodies and hybridized to the anchor strands. Plasma samples from both GBM patients and healthy controls are positioned onto the array, followed by the addition of secondary antibodies and fluorescent markers to allow detection of the levels of cancer biomarkers. The chapter then discusses investigations into the effects of the vascular endothelial growth factor (VEGF) inhibitor Avastin on the

plasma protein profile of glioblastoma patients with actively growing tumors vs. non-growing tumors.

Lastly, Chapter 4 presents a variation on the DEAL technology for the creation of ultra-high density oligonucleotide arrays for the assembly of tissue engineered structures with single cell resolution. The creation of oligonucleotide spots 10 μm x 10 μm in size and 30 μm in pitch is achieved using a microfluidic flow patterning technique to arrange single-stranded bridge oligo sequences onto complementary anchor sequences. Cells are then coded with single-stranded oligos complementary to specific bridge sequences and allowed to hybridize. Single cell resolution patterns of human neurons and astrocytes and, separately, mouse pancreatic islet cells are illustrated and shown to be viable. The advantage of such a technology is that it has the potential to allow for the assembly of any tissue from scratch in virtually any pattern imaginable.

1.5 References

1. Steen, H.; Mann, M. The abc's (and xyz's) of peptide sequencing. *Nature Rev*., **2004**, 5, 699-711.

2. Horn, D. M.; Zubarev, R. A.; McLafferty, F. W. Automated *de novo* sequencing of proteins by tandem high-resolution mass spectrometry. *Proc. Natl. Acad. Sci. USA*, **2000**, 97, 10313–10317.

3. Munchbach, M.; Quadroni, M.; Miotto, G.; James, P. Quantitation and facilitated *de novo* sequencing of proteins by isotopic N-terminal labeling of peptides with a fragmentation-directing moiety. *Anal. Chem.*, ***2000***, 72, 4047-4057.

4. Drenth, J. *Principles of Protein X-Ray Crystallography*. 3rd ed. New York: Springer Science and Business Media, 2006.

5. Cavalli, A.; Salvatella, X.; Dobson, C. M.; Vendruscolo, M. Protein structure determination from NMR chemical shifts. *Proc. Natl. Acad. Sci. USA*, **2007**, 104, 9615-9620.

6. Hanash, S. M.; Pitteri, S. J.; Faca, V. M. Mining the plasma proteome for cancer biomarkers. *Nature*, **2008**, 452, 571-579.

7. Stern, E.; et al. Label-free biomarker detection from whole blood. *Nature Nanotech.*, **2010**, 5, 138-142.

8. Tibes, R.; et al. Reverse phase protein array: validation of a novel proteomic technology and utility for analysis of primary leukemia specimens and hematopoietic stem cells. *Mol. Cancer Ther.*, **2006**, 5, 2512-2521.

9. Cox, J.; Mann, M. Is proteomics the new genomics? *Cell*, **2007**, 130, 395-398.

10. Rosengren, S.; Firestein, G. S.; Boyle, D. L. Measurement of inflammatory biomarkers in synovial tissue extracts by enzyme-linked immunosorbent assay. *Clin. Diagn. Lab. Immunol.*, **2003**, 10, 1002-1010.

11. Gygi, S. P.; Corthals, G. L.; Zhang, Y.; Rochon, Y.; Aebersold, R. Evaluation of two-dimensional gel electrophoresis-based proteome analysis technology. *Proc. Natl. Acad. Sci. USA*, **2000**, 97, 9390-9395.

12. Ferrari, M., ed. *Micro/Nano Technology for Genomics and Proteomics*. New York: Springer Science and Business Media, 2006.

13. Harris, C. Protein-protein interactions for cancer therapy. *Proc. Natl. Acad. Sci. USA*, **2006**, 103, 1659-1660.

14. Wu, G.; Fang, X.; Stein, L. A human functional protein interaction network and its application to cancer data analysis. *Genome Biol.*, **2010**, 11:R53.

15. Clarke, J.; et al. Continuous base identification for single-molecule nanopore DNA sequencing. *Nature Nanotech.*, **2009**, 4, 265-270.

16. Dekker, C. Solid-state nanopores. *Nature Nanotech.*, **2007**, 2, 209-215.

17. Branton, D.; et al. The potential and challenges of nanopore sequencing. *Nat. Biotechnol.*, **2008**, 26, 1146-1153.

18. Huh, D.; et al. Tuneable elastomeric nanochannels for nanofluidic manipulation. *Nature Mater.*, **2007**, 6, 424-428.

19. Fan, R.; et al. DNA translocation in inorganic nanotubes. *Nano Lett.*, **2005**, 5, 1633-1637.

20. Mannion, J. T.; Reccius, C. H.; Cross, J. D.; Craighead, H. G. Conformational analysis of single DNA molecules undergoing entropically induced motion in nanochannels. *Biophys J.*, **2006**, 90, 4538-4545.

21. Merchant, C. A.; DNA translocation through graphene nanopores. *Nano Lett.*, **2010**, 10, 2915-2921.

22. D'Souza, A. L.; et al. A strategy for blood biomarker amplification and localization using ultrasound. *Proc. Natl. Acad. Sci. USA*, **2009**, 106, 17152-17157.

23. Aebersold, R.; et al. Perspective: a program to improve protein biomarker discovery for cancer. *J. Proteome Res.*, **2005**, 4, 1104-1109.

24. Martin, K. J.; Fournier, M. V.; Reddy, G. P. V.; Pardee, A. B. A need for basic research on fluid-based early detection biomarkers. *Cancer Res.*, **2010**, 70, 5203-5206.

25. Johann, D. J.; et al. Combined blood/tissue analysis for cancer biomarker discovery: application to renal cell carcinoma. *Anal. Chem.*, **2010**, 82, 1584-1588.

26. Schroder, C.; Jacob, A.; Ruffer, S.; Fellenberg, K.; Hoheisel, J. D. "Antibody Microarrays for Expression Analysis." *Antibody Engineering, Vol. 2.* 2nd ed. Ed. Kontermann, R.; Dubel, S. New York: Springer Science and Business Media, 2010. pp. 429-445.

27. Zhong, L.; et al. Using protein microarray as a diagnostic assay for non-small cell lung cancer. *Am. J. Respir. Crit. Care Med.*, **2005**, 172, 1308-1314.

28. Miller, J. C.; Butler, E. B.; Teh, B. S.; Haab, B. B. The application of protein microarrays to serum diagnostics: prostate cancer as a test case. *Dis. Markers*, **2001**, 17, 225-234.

29. Vermesh, U.; Choi, J. W.; Vermesh, O.; Fan, R.; Nagarah, J.; Heath, J. R. Fast nonlinear ion transport via field-induced hydrodynamic slip in sub-20-nm hydrophilic nanofluidic transistors. *Nano Lett.*, **2009**, 9, 1315-1319.

Chapter 2

Fast Nonlinear Ion Transport via Field-Induced Hydrodynamic Slip in Sub-20 nm Hydrophilic Nanofluidic Transistors

2.1 Introduction

Recently, novel fluid-mechanical phenomena have been observed as the dimensions of fluidic channels have approached the nanometer scale. Theoretical models[1-4] and experimental demonstrations[5-7] of finite hydrodynamic slip in hydrophobic nanochannels have received considerable attention; however, experimental evidence of slip in hydrophilic nanochannels is nonexistent. Here we report on ion transport through an array of 20 nm-radius, 20 μm-long hydrophilic SiO_2 nanofluidic transistors. Above a threshold source-drain bias, channel conductances are enhanced up to 50-fold over expected values. The improved ion transport is interpreted as arising due to an electric field-induced breakdown of the zero-slip boundary condition. The slip length can be tuned by modulating the surface-charge density of the nanochannels via application of a gate voltage. This phenomenon results in amino acid specific I-V traces when lysine and aspartate monomer solutions are added separately, which demonstrates the potential for

the use of nanofluidic channel devices for high throughput protein sequencing and structure determination. The presence of finite slip results in a ~10^6-fold increase in mechanical power output, and thus also shows promise for efficient energy conversion, filtration, and desalination applications.

The relatively recent emergence of nanochannel fabrication methods[8-10] has allowed electrokinetic phenomena to be investigated in nanofluidic systems, and has created renewed interest in the potential of fluidic devices for energy conversion and other tasks. As the Debye screening length approaches the scale of the channel dimensions, the surface charge dominates the electrokinetic flow behavior within the channel, controlling the concentration of electrolytes[11-16] such that unipolar counterions dominate current flow (**Figure 2.1**). This phenomenon can potentially be harnessed for mechanical-to-electrical energy conversion by using pressure to drive a streaming current through the nanochannel. Alternatively, electrical-to-mechanical energy conversion is possible by applying an electric field across the length of the nanochannel, thereby driving fluid through by electroosmosis[17-19]. However, current flow through nanofluidic channels at a given pressure, or source-drain voltage, is severely limited due to the no-slip boundary condition that characterizes most such systems. This boundary condition represents the fact that there is no fluid or ion flow at the liquid/channel interface. The counterion density is highest at this interface, but because these counterions are immobilized by surface charges, those ions do not contribute to the current, resulting in low energy conversion efficiencies.

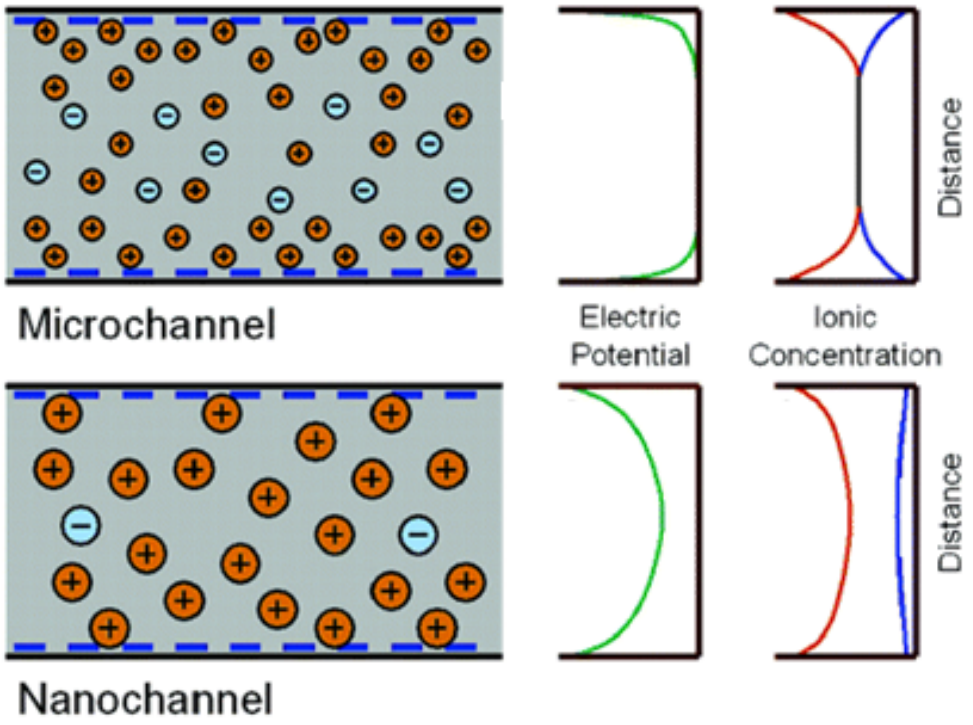

Figure 2.1. Nanochannel electrokinetics. At the nanoscale, channel dimensions become comparable to the Debye screening length, such that unipolar counterions in solution form an electric double layer and dominate current flow when channel surfaces are charged. This phenomenon only occurs below a threshold ion concentration. Adapted from *Nano Lett.* **2005**, 5, 943-948.

The no-slip boundary condition is not a fundamental limitation, however, and systems with finite slip have received recent attention[20,21]. Slip velocity (υ_{slip}) is proportional to the shear rate, according to the following equation:

$$\upsilon_{slip} = \mathbf{b}(d\upsilon/d\mathbf{x})|_{surf}.$$

Here, υ is the fluid velocity, **x** is the coordinate normal to the surface, and **b** is the slip length, or the distance into the surface where υ extrapolates to zero.

A number of theoretical studies[21,22] have revealed that mechanical-to-electrical energy conversion efficiencies can be very high, even approaching 100 %, for nanofluidic

channels exhibiting a large **b**. These studies have focused on streaming currents through smooth, hydrophobic nanofluidic channels, since such systems are thought to exhibit the greatest potential for slip. For example, Ren and Stein[21] have calculated that, for a 10 nm high slit-shaped, hydrophobic nanochannel, 40 % energy conversion efficiencies are realistic for **b** values of 30 nm. Indeed, very large slip lengths have been measured in carbon nanotube-based nanofluidic channels[5,7]. However such devices may not be suitable for energy conversion since the lack of surface charges prevents the creation of an intrachannel unipolar environment essential for mechanical-to-electrical energy conversion. Currently, most nanofluidic channels are fabricated from silica or other materials that yield charged and/or hydrophilic surfaces. Due to the strong attraction of Stern layer counterions to such hydrophilic surfaces, the no-slip condition is difficult to overcome. For example, Dekker's group has measured energy conversion in hydrophilic nanochannels under no-slip conditions, and found a conversion efficiency of only 3 %[23]. They calculated a maximum conversion efficiency of 12 % for similar monovalent ions in water[22]. Much greater conversion efficiencies will be needed for practical technologies to be realized. If the no-slip boundary condition in hydrophilic channels could be surmounted, greatly enhanced streaming currents and energy conversion efficiencies would be possible in such systems, making energy conversion applications far more feasible.

2.2 Experimental Methods

In this chapter, we report on the electrokinetics of potassium chloride (KCl) ion transport through nanofluidic transistors comprised of arrays of oval shaped, hydrophilic, silica nanochannels. Although ion transport has been investigated previously in a single SiO_2 nanofluidic channel[10] with similarly small dimensions, our fabrication method[24] produces sufficiently large numbers of closely spaced SiO_2 nanochannels such that currents can be measured even at very low KCl molarities ([KCl] = 10^{-7} M).

The experimental setup is shown in **Figure 2.2**. The nanofluidic device consisted of a 20 micrometer-long array of 80 parallel, 20 nm × 30 nm cross section silica channels built from a template of silicon nanowires fabricated using the SNAP method[24] (**Figure 2.2b,c**). An indium tin oxide (ITO) gate electrode is deposited on top of the array, with a silica gate oxide layer sandwiched in between. As shown in **Figure 2.2c**, extremely narrow (~3 nm) channels between the primary channels were observed. These likely arise from a SiO_2 deposition process that is not 100 % conformal. However, the voids are far smaller than the primary nanochannels and their contribution to the ionic current should be negligible. The nanochannels interface with two sets of microfluidic channels that act as reservoirs for electrolyte solutions. The device is sealed with a slab of plasma-bonded PDMS to isolate the microfluidic channels and prevent leakage current. Finally, holes are punched into the PDMS to allow the insertion of Ag/AgCl electrodes into the microfluidic channels for current measurements. The detailed fabrication processes are described in the Appendix. The SNAP-based nanochannel fabrication method is robust, allowing devices to be consistently generated with nearly 100 % yield.

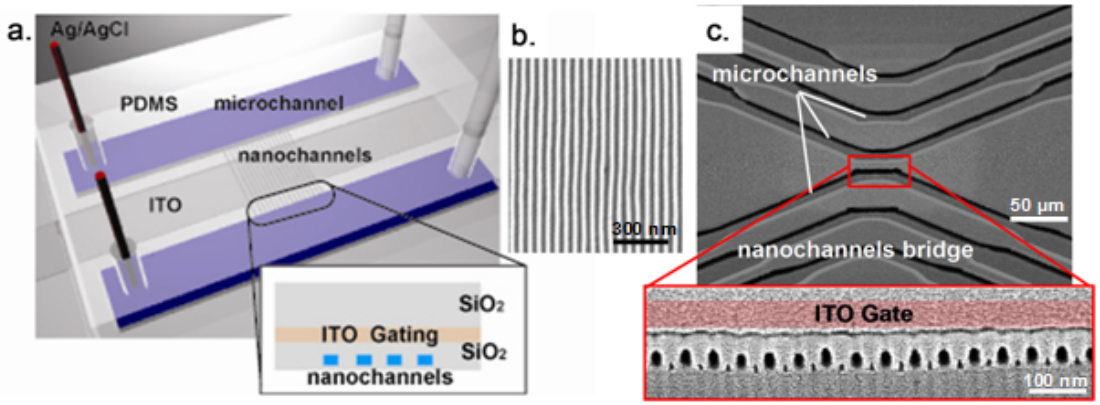

Figure 2.2. Overview of nanofluidic device. a. Experimental setup of essential components of the nanofluidic transistor array. The blue microchannels are electrically contacted with Ag/AgCl source and drain electrodes. These microchannels are connected via a bridge of 80 nanofluidic channels in SiO_2. As shown in the inset, the nanochannels are topped with an indium tin oxide (ITO) gate electrode. **b.** Scanning electron micrograph (SEM) of the silicon nanowire array (top view) from which the SiO_2 nanochannels were templated. **c.** SEM of the nanofluidic device. The 6 V-shaped structures are microfluidic channels; only the two opposing microchannels in the central region of the image are utilized for these experiments. These two channels are bridged by the 20 μm long nanofluidic channel array. Below, an end-on SEM view of a few of the (20 nm wide × 30 nm high) nanofluidic channels is shown, with the position of the ITO gate electrode indicated.

2.3 Results and Discussion

2.3.1 Slip-enhanced ion transport through nanofluidic channels

Upon completion of device fabrication, we introduced aqueous solutions of KCl into the device at concentrations ranging from 10^{-7} M to 10^{-1} M, optically observed nanochannel filling over the entire array, and measured the source-drain current-voltage (I_{SD}-V_{SD}) characteristics over a 30 – 50 volt range (conductance plots (dI_{SD}/dV_{SD}) at the abovementioned KCl concentrations are presented in the Appendix). Similar to previous studies[12,13], which were limited to conductance measurements at low bias (< 5 V),

conductance saturation is present below a threshold concentration of 10^{-3} M. This saturation occurs because the negatively charged silanol groups at the SiO_2 nanochannel surface attract K^+ counterions and repel Cl^- anions over the characteristic Debye length (κ^{-1}), which is given by[25]:

$$\kappa^{-1} = [\varepsilon k_B T/(e^2 N_A \Sigma_i c_i Z_i^2)]^{1/2}.$$

Here, c_i is the molar concentration and Z_i is the valence of ion species *i*. Standard constants include ε (the permittivity), k_B (Boltzmann constant), e (electron charge), and N_A (Avogadro's number). For [KCl] = 10^{-3} M, this gives a Debye length of 9.7 nm, which is comparable to the 10 nm radius of our nanochannels. As a result, the K^+ concentration within our nanochannels is determined by the surface charge on the walls for bulk [KCl] $\leq 10^{-3}$ M. On the other hand, for [KCl] > 10^{-3} M, the Debye length becomes smaller than the nanochannel radius, leading to shielding of surface charges and more ohmic ion transport behavior (**Figure 2.3b**).

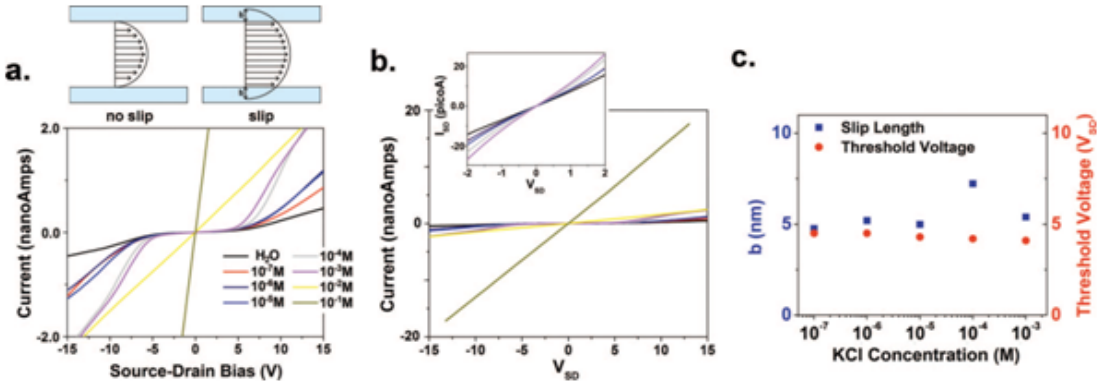

Figure 2.3. Source-drain current-voltage (I-V) data of the nanofluidic devices at various values of [KCl]. a. I-V curves for [KCl] from 10^{-7} to 10^{-1} M. The sharp increase in conductance at V_{SD} ~5 V for all curves for which [KCl] $\leq 10^{-3}$ M is interpreted as the onset of nonzero slip. Schematic diagrams show ion velocity profiles in both the low bias no-slip region and the high bias slip region. **b.** Source-drain I-V data plotted with an expanded current axis, illustrating conductance saturation for [KCl] $\leq 10^{-3}$ M. The saturation implies that, for those concentrations, the Debye screening length in the channel is larger than the channel width. Inset: Expanded I-V curves for [KCl] $\leq 10^{-3}$ M. Note the y-axis scale is picoamperes. The color coding of the traces is the same as in part a. **c.** Slip length (**b**) vs KCl concentration for [KCl] $\leq 10^{-3}$ M along with a display of the threshold voltage (V_T) above which slip occurs with respect to these same KCl concentrations.

In the surface charge-governed ion transport regime, [KCl]$\leq 10^{-3}$ M, and for V_{SD} values above a threshold voltage (V_T) of about 5 V, the current exhibits a sharp and nonlinear increase with increasing bias (**Figure 2.3a**) and conductance enhancement of 20-50 fold, depending upon [KCl]. We propose that this nonlinear behavior arises from an electric field-induced breakdown of the zero-slip condition. The transition into the finite-slip regime can be attributed to the changing behavior of the K^+ ion double layer in the nanochannel solution. The layer closest to the surface, called the Stern layer, is about 0.3 nm thick[26] and consists of K^+ ions immobilized to the nanochannel surface. The second layer, which can move under no-slip conditions, is a diffuse layer of K^+ ions that comprises the rest of the solution within the nanochannels[27] (**Figure 2.4a**).

However, it has been theorized that the Stern layer can be moved tangential to the surface under the influence of an external electric field[2,26] (**Figure 2.4b**). In our device, this may be happening above the threshold V_{SD}, in which case the electric field parallel to the nanochannel surface is overcoming the attraction of the Stern layer K^+ ions to the silica surface. As a result, these ions move along the surface, electroosmotically pulling water with them, and the zero-slip condition no longer holds. Due to viscous forces, hydrodynamic slip at the nanochannel surface increases the velocity of all species within the nanochannel, resulting in greatly enhanced conductance as illustrated in **Figure 2.4b** as well as in the schematic diagrams in **Figure 2.3a**.

Nonlinear I-V characteristics in somewhat larger (40 nm deep) nanofluidic channels for sodium phosphate concentrations in the range 10^{-4} – 10^{-2} M have been observed by Kim, et al[9]. However, their results reflect very different physics. They observed a broad, current-saturated, intermediate bias region separating their low- and high-bias regions. They interpret their data within the framework of concentration polarization, in which an ion depletion region develops at the microchannel/nanochannel interface, which leads to the current saturation regime in their I_{SD}-V_{SD} plots. At sufficiently high bias, instabilities (imaged as vortices) appear at the microchannel/nanochannel interface, collapsing the depletion regions, and resulting in a second phase of steep current increase (the overlimiting region). At even higher bias, conductance values return to their original (low-bias) levels. The lack of a current-saturated region in our data, the fact that conductances remain high and stable as V_{SD} increases, the absence of nonlinear ion transport above 10^{-3} M, and the below-described

voltage-gating experiments all distinguish our system and support the interpretation of non-zero slip in our channels.

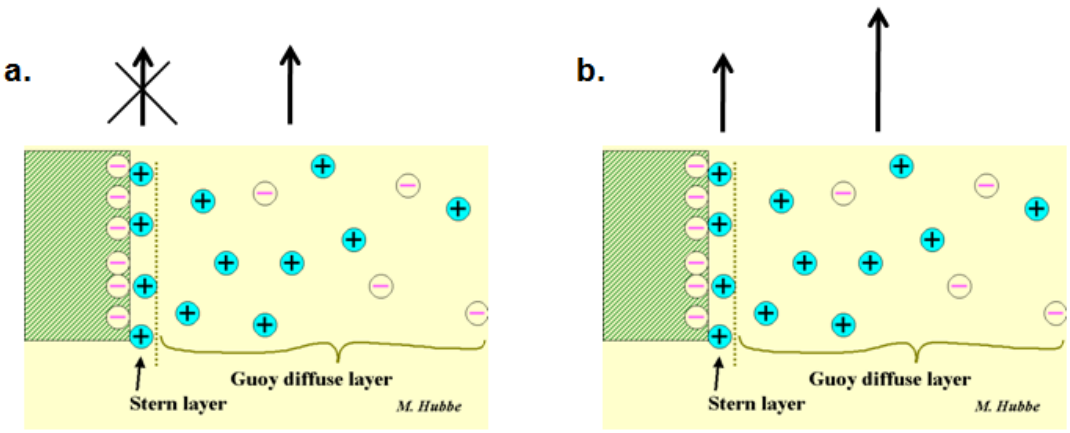

Figure 2.4. The effect of a high electric field on Stern layer ions. a. Stern layer counterions at the channel surface are normally immobolized by surface charges and do not contribute to the current. **b.** If Stern layer counterions can travel in the presence of a high electric field, the resulting finite slip at the channel surface allows enhanced velocity of diffuse layer ions via electro-osmosis and viscous forces. *Adapted from M. Hubbe, Dept. of Forest Biomaterials, NCSU.*

2.3.2 Nanochannel ion transport model

The contribution of slip to conductance enhancement within a nanochannel of radius comparable to the Debye screening length can be modeled as follows (see Appendix for detailed description). To maintain electroneutrality, the nanochannel surface charge must equal the counterion charge in the solution ($\mathbf{Q}_{surface} = \mathbf{Q}_{solution}$). This is expressed as:

$$\mathbf{A} \times \boldsymbol{\sigma} = \mathbf{V} \times \mathbf{e} \times \mathbf{n}_{cr} \qquad (1),$$

where **A** is the nanochannel surface area, $\boldsymbol{\sigma}$ is the surface charge density, **V** is the nanochannel volume, and $\mathbf{n}_{cr}$ is the critical ion density at which nanochannel ion transport transitions from bulk-like to a surface-charge governed regime (herein, $\mathbf{n}_{cr}$ is

equivalent to a K^+ concentration of ~10^{-3} M). The value of $\boldsymbol{\sigma}$ obtained is 0.0006 C/m^2. Using this value, the slip length **b** can be calculated using the conductance equation:

$$\mathbf{G = N \times 4\,\mu\,\sigma\ (d/L)\,(1 + b}/l_{stern}) \qquad (2),$$

where $\boldsymbol{\mu}$ is the K^+ mobility (= 7.6×10^{-8} $m^2/(V\cdot s)$), **d** is the nanochannel hydraulic diameter (= 24 nm), **L** is the nanochannel length (=20 micrometers), **N** is the number of nanochannels (80) in the array, and l_{stern} is the thickness of the Stern layer (~0.3 nm), which is also the distance over which the shear plane moves when shifting from no-slip to slip conditions. The first part of equation (2), $\mathbf{N \times 4\,\mu\,\sigma}$ (**d/L**), represents electrokinetic conductance through the nanochannels in the absence of slip, and the (1 + **b**/ l_{stern}) factor represents the conductance enhancement due to slip[1,2]. For conductance in the low bias ($V_{SD} < V_T$) regime, where there is no slip (**b** = 0), the measured conductance (~14.4 pS) is almost identical to the value calculated (~16.8 pS) using equations (1) and (2).

2.3.3 Tuning the nanochannel surface charge density by application of gate voltages

If the emergence of hydrodynamic slip is indeed a consequence of a field-induced breakdown in electrostatic attractions between the Stern layer and the channel wall, reducing the surface charge density should lower this electrostatic barrier and enhance slip. This reasoning is supported by two observations. First, there is no significant difference either in slip length or in the threshold voltage at which slip occurs for all values of [KCl]≤ 10^{-3} M (**Figure 2.3c**). This is attributable to the fact that the surface charge density remains fairly stable throughout these concentrations. Additional support stems from experiments that exploit a gate electrode to tune the nanochannel surface

charge density and measure the corresponding change in slip length. The gating experiments on a 10^{-4} M KCl solution are presented in **Figure 2.5**.

Another noteworthy observation is the reversal in the effect of V_g on conductance between the low bias and high bias regimes. As V_g becomes more positive, the bare surface charge density (σ) extracted from equation (1) becomes less negative (**Figure 2.5b**), which has two potentially competing effects. The first is a decrease in the intrachannel counterion concentration, which tends to *decrease* the conductance. The second is a decrease in the attraction of the Stern layer to the channel surface, which tends to *increase* the conductance (due to slip). At low source-drain bias ($V_{SD} < V_T$), the electric field is not strong enough to overcome the attraction of the Stern layer to the surface, so the decrease in ion concentration with increased V_g (**Figure 2.5a inset**) translates directly to a decreased conductance, as shown in previous studies[11,12]. By contrast, in the high source-drain bias ($V_{SD} > V_T$) regime, the electric field is strong enough to move the Stern layer. Therefore, as V_g becomes more positive, the Stern layer moves faster (larger slip length, **b**) (**Figure 2.5c**), resulting in a net increase in conductance. Alternatively, less force is required to begin moving the Stern layer (lower V_T) as its attraction to the channel surface decreases with more positive V_g.

Over the entire range of V_{SD}, the nonlinear nature of the I-V curves is evident for all values of V_g (**Figure 2.5a**). In the low bias regime ($V_{SD} < V_T$), where there is no slip, the ohmic response is well-described by the conductance equation without the enhancement factor (notice that the enhancement factor reduces to unity for **b** = 0) as shown in the Appendix. In the high V_{SD} regime ($V_{SD} > V_T$), these curves were fitted with the full conductance equation including the slip enhancement term illustrated in equation

(2). Such linear fits permitted us to extract the slip length, **b**, for each value of V_g (**Figure 2.5c**). Our obtained slip lengths in the range of ~2 – 10 nm are comparable to those proposed in studies of SiO_2 surfaces[28] and represent on average 8 – 35-fold increases in conductance.

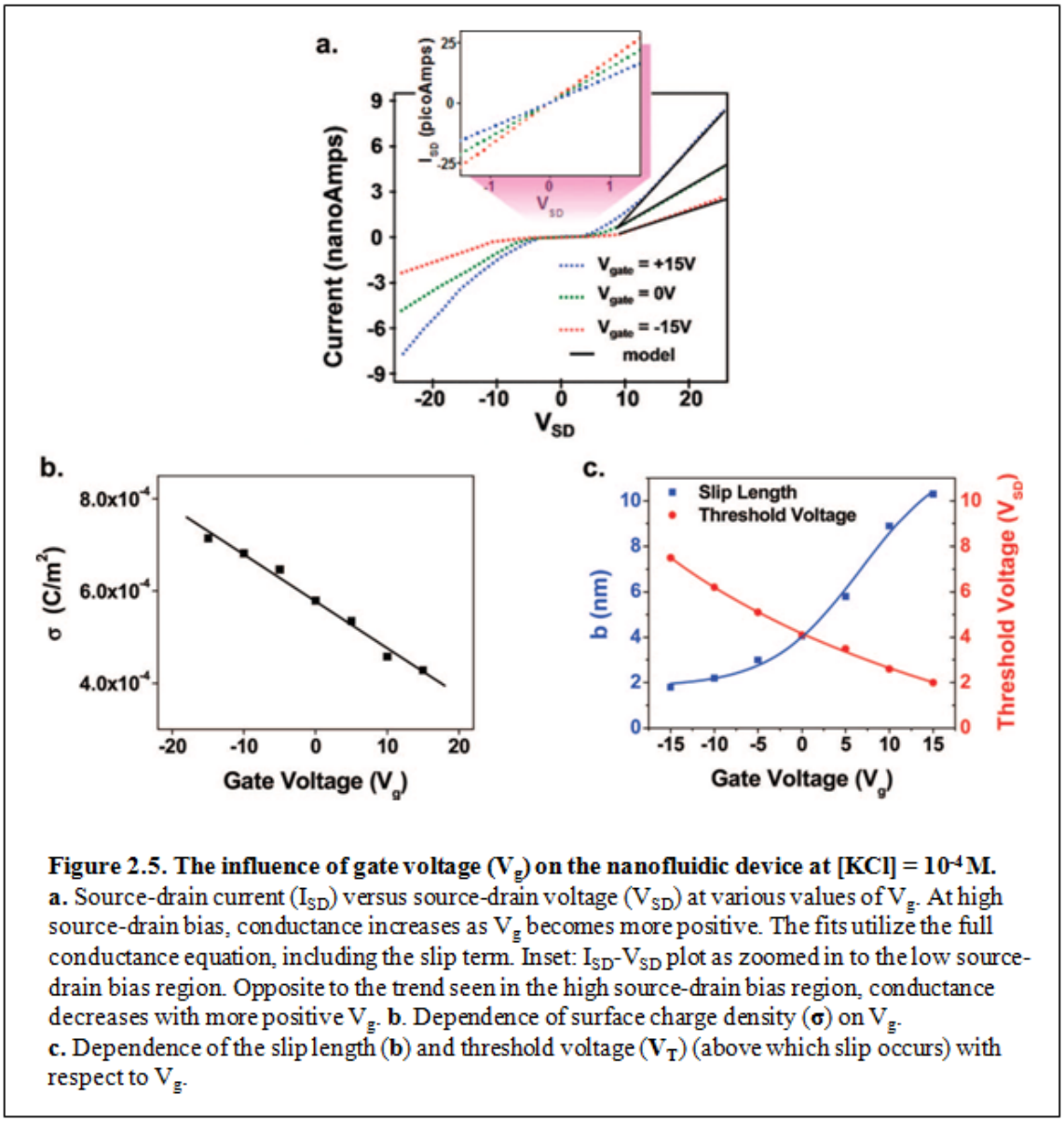

Figure 2.5. The influence of gate voltage (V_g) on the nanofluidic device at [KCl] = 10^{-4} M. **a.** Source-drain current (I_{SD}) versus source-drain voltage (V_{SD}) at various values of V_g. At high source-drain bias, conductance increases as V_g becomes more positive. The fits utilize the full conductance equation, including the slip term. Inset: I_{SD}-V_{SD} plot as zoomed in to the low source-drain bias region. Opposite to the trend seen in the high source-drain bias region, conductance decreases with more positive V_g. **b.** Dependence of surface charge density (**σ**) on V_g. **c.** Dependence of the slip length (**b**) and threshold voltage ($\mathbf{V_T}$) (above which slip occurs) with respect to V_g.

2.3.4 Peptide sequencing

A 10^{-4} M solution of aspartic acid monomers at a pH of 5.5 was inserted into the nanochannel array, and I-V curves were obtained. The device fabrication and measurement setup were identical to those used in I-V measurements with KCl. The data for the amino acid species under varying gate voltages (**Figure 2.6a**) is similar to that seen with 10^{-4} M KCl, with enhanced ion transport occurring above a threshold voltage, but, for aspartic acid, this increase is only observed under the influence of a positive gate voltage. For $V_g = 0$, the conductance is just starting to increase at V_{SD} above $|\pm 20$ V$|$, and for $V_g < 0$, this phenomenon is completely suppressed at all values of V_{SD}. At low source-drain bias, decreasing conductance with increasing V_g parallels the behavior of KCl **(Figure. 2.6a inset**) and emphasizes the opposite trend in conductance vs. gate voltage at low and high source-drain bias. The slip lengths range from 0 – 8 nm (**Figure 2.6b**), values that are comparable to those seen with KCl, although the suppression of the slip length at negative gate voltages is not seen with KCl under the V_{SD} range measured.

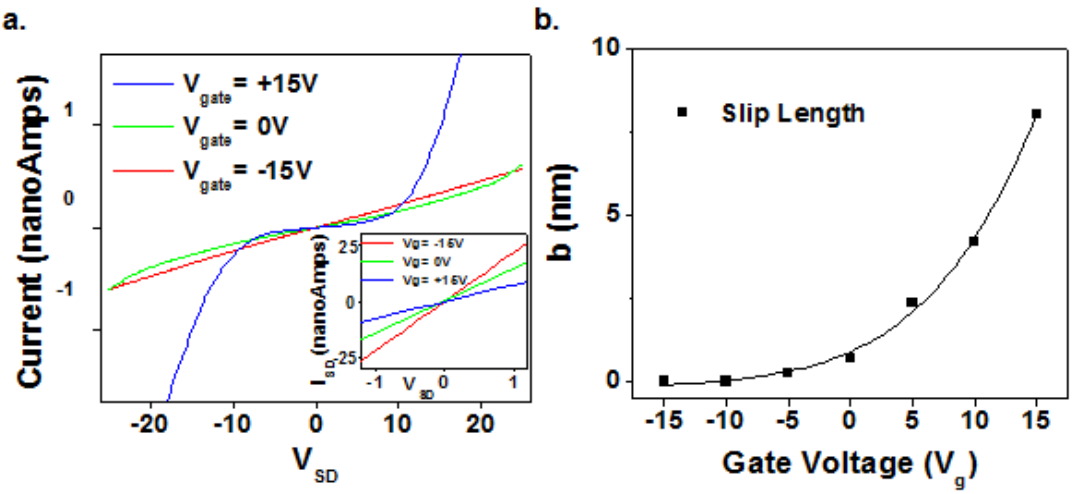

Figure 2.6. The influence of gate voltage (V_g) on the nanofluidic device at [Aspartic Acid] = 10^{-4} M. a. Source-drain current (I_{SD}) versus source-drain voltage (V_{SD}) at V_g = -15 V, 0 V, +15 V, with a V_{SD} sweep from -25 V to +25 V. Inset: Expanded I_{SD}-V_{SD} curves illustrating the dependence of conductance on V_g at low source-drain bias. **b.** Dependence of the slip length (**b**) on V_g. The slip length (**b**) increases as V_g is varied from -15 V to +15 V in 5 V increments.

However, the similarities between the measurements of the aspartic acid and KCl solutions indicate that positive ions are the dominant charge carriers in the aspartic acid solution. Above a pH of ~3.9, the majority of aspartic acid monomers are deprotonated, giving negatively charged aspartate ions and positive hydronium ions. The negative surface charge of the nanochannels with the ensuing Debye length on the order of the nanochannel radius prevents the entry of aspartate ions, in which case conductance is dominated by hydronium ions.

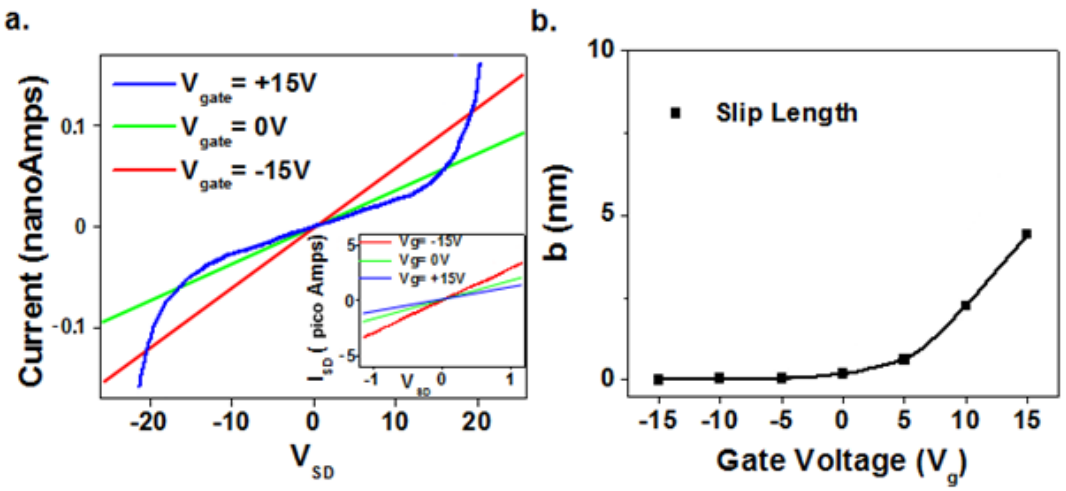

Figure 2.7. The influence of gate voltage (V_g) on the nanofluidic device at [Lysine] = 10^{-4} M. **a.** Source-drain current (I_{SD}) versus source-drain voltage (V_{SD}) at V_g = -15 V, 0 V, +15 V, with a V_{SD} sweep from -25 V to +25 V. Inset: Expanded I_{SD}-V_{SD} curves illustrating the dependence of conductance on V_g at low source-drain bias. **b.** Dependence of the slip length (**b**) on V_g. The slip length (**b**) increases as V_g is varied from -15 V to +15 V in 5 V increments.

A similar experiment was also conducted on a 10^{-4} M solution of lysine monomers at a pH of 9.0 (**Figure 2.7)**. Here, enhanced ion transport above a threshold voltage was observed as well, however the threshold voltage was considerably higher than for aspartate and was only significantly observed for $V_g > +5$ V (**Figure 2.7a**). Even at these positive gate voltages, the conductance just starts to increase at V_{SD} above |±30 V|, resulting in slip lengths that range from 0 – 5 nm (**Figure 2.7b**). Also, the values of the current are about an order of magnitude smaller than those seen for aspartate, signifying that the conducting species must be considerably larger in this case. Given these observations and the fact that below a pH of ~ 10.5, the majority of lysine monomers are protonated, positively charged lysine monomers are most likely the major conducting species. With the differences in I-V characteristics and slip lengths seen for aspartate and lysine, nanofluidic channels have great potential for identifying all the other amino acids

based on mass and pKa value. Once this is achieved, the obvious next step would be to sequence peptides.

2.3.5 Mechanical power enhancement

The ability to access finite-slip conditions in these nanochannels is encouraging from the point-of-view of energy conversion. We consider the mechanical power output of our device. This is the kinetic energy per unit time that is associated with the electroosmotic movement of fluid through the nanochannel array:

$$\textbf{Mechanical Power} = (\mathbf{1/2})(\rho \upsilon_{eof} A)\, \upsilon_{eof}^{\,2} \qquad (3),$$

where υ_{eof} is the electroosmotic fluid velocity of water through the nanochannels, and $\rho \upsilon_{eof} A$ is the mass flow rate. According to equation (3), the mechanical power increases as the cube of the electroosmotic fluid velocity. Therefore, an 80 – 200-fold increase in fluid velocity, as calculated in our device due to slip, translates to a ~10^6 enhancement in mechanical power. Detailed calculations on electroosmotic fluid velocity enhancements extracted from current measured in the nanochannel array device and their correlation to mechanical power are described in the Appendix. Such a large improvement in mechanical power through these silica channels suggests that they may also be useful for certain applications outside of peptide sequencing for which nanofluidic devices have been targeted, such as filtration and water desalination.

Based on our results showing enhanced ion transport, silica-based nanofluidic devices would likely exhibit a higher mechanical-to-electrical energy conversion efficiency than the current measured limit of 3 %[23]. In a recent work by Ren and Stein[21], theoretical characterization of electrokinetic transport through nanochannels showed that

streaming current increases dramatically with increases in slip length, predicting > 70 % energy conversion efficiencies. The ability to tune slip lengths with gate voltages should permit the testing of this theory in future experiments. Measurements of streaming currents through nanochannels will require a slight modification of our device design, since the PDMS/silica interface cannot tolerate high pressures.

2.4 Conclusion

In summary, we have investigated ion and amino acid transport through an array of 80 closely-spaced sub-20 nm hydrophilic SiO_2 nanochannels over a 30 – 50 V range of source-drain biases. We have observed that for ion concentrations at which the Debye length exceeds the nanochannel radius, ion transport becomes greatly magnified at a threshold source-drain bias. This behavior can be described by a theoretical model that attributes the enhancement to a breakdown of the no-slip boundary condition at the liquid/nanochannel surface interface at high source-drain bias. By varying the surface charge density of the nanochannels using a gate electrode, we were able to tune the slip length to obtain further enhancements in ion transport through the hydrophilic nanochannel array. Using this technique, we were also able to obtain specific I-V characteristics for two different amino acids, aspartate and lysine. These results imply that such devices have the potential to be utilized for protein sequencing and structure determination and can be harnessed for efficient energy conversion applications.

2.5 References

1. Bocquet, L.; Barrat, J. L. Flow boundary conditions from nano- to micro-scales. *Soft Matter*, **2007**, 3, 685-693.

2. Joly, L.; Ybert, C.; Trizac, E.; Bocquet, L. Liquid friction on charged surfaces: from hydrodynamic slippage to electrokinetics. *J. Chem. Phys.*, **2006**, 125, 204716.

3. Joseph, S.; Aluru, N. R. Why are carbon nanotubes fast transporters of water? *Nano Lett.*, **2008**, 8, 452-458.

4. Netz, R. R. Electrofriction and dynamic Stern layers at planar charged surfaces. *Phys. Rev. Lett.*, **2003**, 91, 138101.

5. Holt, J. K.; et al. Fast mass transport through sub-2-nanometer carbon nanotubes. *Science*, **2006**, 312, 1034-1037.

6. Lee, C.; Choi, C.; Kim, C. Structured surfaces for a giant liquid slip. *Phys. Rev. Lett.*, **2008**, 101, 064501.

7. Majumder, M.; Chopra, N.; Andrews, R.; Hinds, B. J. Nanoscale hydrodynamics: enhanced flow in carbon nanotubes. *Nature*, **2005**, 438, 44.

8. Cao, H.; et al. Fabrication of 10 nm enclosed nanofluidic channels. *Appl. Phys. Lett.*, **2002**, 81, 174-176.

9. Kim, S. J.; Wang, Y. C.; Lee, J. H.; Jang, H.; Han, J. Concentration polarization and nonlinear electrokinetic flow near a nanofluidic channel. *Phys. Rev. Lett.*, **2007**, 99, 044501.

10. Liang, X. G.; Morton, K. J.; Austin, R. H.; Chou, S. Y. Single sub-20 nm wide, centimeter-long nanofluidic channel fabricated by novel nanoimprint mold fabrication and direct imprinting. *Nano Lett.*, **2007**, 7, 3774-3780.

11. Fan, R.; Yue, M.; Karnik, R.; Majumdar, A.; Yang, P. D. Polarity switching and transient responses in single nanotube nanofluidic transistors. *Phys. Rev. Lett.*, **2005**, 95, 086607.

12. Karnik, R.; et al. Electrostatic control of ions and molecules in nanofluidic transistors. *Nano Lett.*, **2005**, 5, 943-948.

13. Stein, D.; Kruithof, M.; Dekker, C. Surface-charge-governed ion transport in nanofluidic channels. *Phys. Rev. Lett.*, **2004**, 93, 035901.

14. Powell, M. R.; et al. Nanoprecipitation-assisted ion current oscillations. *Nature Nanotech.*, **2008**, 3, 51-57.

15. Vlassiouk, I.; Siwy, Z. Nanofluidic diode. *Nano Lett.*, **2007**, 7, 552-556.

16. Kalman, E.; Vlassiouk, I.; Siwy, Z. Nanofluidic bipolar transistor. *Adv. Mater.*, **2008**, 20, 293-297.

17. Pennathur, S.; Santiago, J.G. Electrokinetic transport in nanochannels. 1. Theory. *Anal. Chem.*, **2005**, 77, 6772-6781.

18. Pennathur, S.; Santiago, J.G. Electrokinetic transport in nanochannels. 2. Experiments. *Anal. Chem.*, **2005**, 77, 6782-6789.

19. Baldessari, F.; Santiago, J.G. Electrophoresis in nanochannels: brief review and speculation. *J. Nanobiotechnology*, **2006**, 4, 12.

20. Pennathur, S.; Eijkel, J. C.; van den Berg, A. Energy conversion in microsystems: is there a role for micro/nanofluidics? *Lab Chip*, **2007**, 7, 1234-1237.

21. Ren, Y. Q.; Stein, D. Slip-enhanced electrokinetic energy conversion in nanofluidic channels. *Nanotechnology*, **2008**, 19, 195707.

22. Van der Heyden, F. H. J.; Bonthuis, D. J.; Stein, D.; Meyer, C.; Dekker, C. Electrokinetic energy conversion efficiency in nanofluidic channels. *Nano Lett.*, **2006**, 6, 2232-2237.

23. Van der Heyden, F. H. J.; Bonthuis, D. J.; Stein, D.; Meyer, C.; Dekker, C. Power generation by pressure-driven transport of ions in nanofluidic channels. *Nano Lett.*, **2007**, 7, 1022-1025.

24. Melosh, N. A.; et al. Ultrahigh-density nanowire lattices and circuits. *Science*, **2003**, 300, 112-115.

25. Chun, M. S.; Park, W. C. Time evolution of electrokinetic flow-induced streaming potential and flux in dead-end and cross-flow filtration of colloids through nanopores. *J. Membr. Sci.*, **2004**, 243, 417-424.

26. Gupta, A. K.; Coelho, D.; Adler, P. M. Influence of the Stern layer on electrokinetic phenomena in porous media. *J. Colloid Interface Sci.*, **2007**, 316, 140-159.

27. Fawcett, W. R. *Liquids, Solutions, and Interfaces: From Classical Macroscopic Descriptions to Modern Microscopic Details (Topics in Analytical Chemistry)* Oxford: Oxford Univ. Press, 2004.

28. Bonaccurso, E.; Kappl, M.; & Butt, H. J. Hydrodynamic force measurements: boundary slip of water on hydrophilic surfaces and electrokinetic effects. *Phys. Rev. Lett.*, **2002**, 88, 076103.

29. Delgado, A.V. *Interfacial Electrokinetics and Electrophoresis*. New York: Marcel Dekker, 2002.

30. Lyklema, J. *Fundamentals of Interface and Colloid Science, Vol. II*. London: Academic Press, 1995.

31. Israelachvili, J. N. *Intermolecular and Surface Forces*. London: Academic Press, 1992.

32. Vlassiouk, I.; Smirnov, S.; Siwy, Z. Ionic selectivity of single nanochannels. *Nano Lett.*, **2008**, 8, 1978-1985.

2.6 Appendix A: Nanochannel Fabrication and Measurement

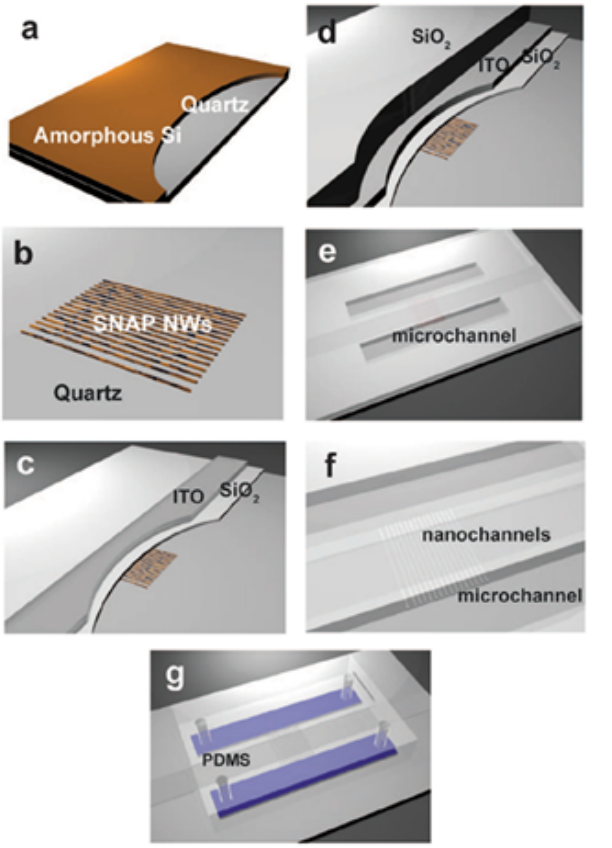

Figure 2.8
Nanochannel device fabrication. **a.** 1 x 1 inch quartz wafer with a 30 nm thick amorphous silicon layer. **b.** A 5 μm wide array of 80 SNAP nanowires patterned from the amorphous silicon layer. **c.** A 40 nm thick low temperature oxide gate oxide layer is deposited onto the nanowire array followed by deposition and patterning of an indium tin oxide gate electrode. **d.** A 5.5 μm thick low temperature oxide layer is deposited next. **e.** Microchannels are etched through the low temperature oxide all the way down to the level of the nanowires. **f.** Nanochannels are created by XeF_2 etching of the silicon nanowires. **g.** A PDMS slab with input and output holes is aligned over the microchannels and plasma bonded to the wafer. Ionic solutions and Ag/AgCl electrodes are inserted into microchannel inputs on both sides of the nanochannels.

The first step in building nanochannels (**Figure 2.8**) was to generate a nanowire template. The SNAP method[24] and standard electron beam lithography (EBL) were used to make an array of silicon nanowires on a transparent quartz substrate with a 30 nm-thick amorphous silicon layer deposited using an e-beam evaporator. In the silicon nanowire array generated by the SNAP method, each wire was about 15 – 20 nm-wide with a pitch of 50 nm. The wires were sectioned into regions 20 μm in length and 5 μm in

width by standard electron beam lithography (EBL). Low Pressure Chemical Vapor Deposition (LPCVD) was then used to deposit a 40 nm-thick silicon dioxide gate oxide layer on top of and between the wires according to the reaction: $SiH_4 + O_2 \rightarrow SiO_2 + 2H_2$. A 50 nm-thick layer of indium tin oxide (ITO) was sputtered on top of the low temperature oxide (LTO), patterned with photoresist, and etched with a 0.5 M HCl solution to create the gate electrode. A 5 μm-thick layer of LTO was deposited on top of the device. Photoresist was spun onto the LTO layer and a microchannel pattern was made by photolithography. The pattern was etched down via an Active Oxide Etching (AOE) process (CHF_3:C_4F_8:Ar = 33 sccm:7 sccm:10 sccm, 200 W, 10 mTorr, 15 minutes) to expose the ends of the SNAP wires. This gave a set of microchannels connecting either end of the SNAP wires. The microchannel depth was about 5.5 μm as confirmed by a surface profiler (Dektak 150). The photoresist was stripped by acetone, and the substrate was further cleaned by a piranha solution (H_2SO_4: H_2O_2 = 5:1 by volume). At this point, XeF_2 was used to selectively and isotropically etch the silicon wires to form hollow channels within the glass according to the reaction: $2XeF_2 + Si \rightarrow SiF_4(g) + 2Xe(g)$. Before loading substrates into the XeF_2 etching chamber, the substrates were dipped into a buffered oxide etching solution (BOE: NH_4F/HF= 6:1 by volume) for 1 second to remove native oxide layers on the exposed tips of the silicon wires. The pressure of XeF_2 gas was maintained at about 2800 mTorr during the etching procedures. The etching progress was monitored by a color change in the array as viewed by optical microscopy. Finally, PDMS with drilled input/output holes was bonded to the device by using an oxygen plasma technique to create a watertight seal between the microchannels. This seal ensures that the only connection between the microchannels is via the

nanochannels. Ionic solutions were inserted through the input holes in the PDMS, and the ionic current measurements were carried out with the use of a source/preamplifier unit (Keithley 2400). Commercially available Ag/AgCl electrode assemblies (E. W. Wright) were used. The ensuing electrokinetic current could be read, thereby allowing the characterization of ionic transport through the nanochannels.

2.7 Appendix B: Conductance Equation Derivation

The contribution of slip to conductance enhancement within a nanochannel of radius comparable to the Debye screening length can be modeled as follows. To maintain electroneutrality, the nanochannel surface charge must equal the counterion charge in the solution. This is expressed as:

$$\mathbf{Q}_{surface} = \mathbf{Q}_{solution} \qquad \text{(eq. A1).}$$

This fundamental equation can be expanded to show its components, which gives:

$$\mathbf{A} \times \sigma = \mathbf{V} \times \mathbf{e} \times (\mathbf{n_K} + \mathbf{n_{Cl}}) \qquad \text{(eq. A2),}$$

where **A** is the nanochannel surface area, σ is the surface charge density, **V** is the nanochannel volume, **e** is the electron charge, and $\mathbf{n_K}$ and $\mathbf{n_{Cl}}$ are the K^+ and Cl^- ion densities, respectively. For [KCl] ≤ 10^{-3} M, the interior of the nanochannel is virtually unipolar, made up almost entirely of K^+ ions, so that the term $\mathbf{n_{Cl}}$ becomes negligible. The factor $\mathbf{n_K} + \mathbf{n_{Cl}}$ can then be approximated as the parameter $\mathbf{n_{cr}}$, which is defined as the critical ion density within the nanochannel at which ion transport transitions from bulk-like to a surface charge-governed regime (herein, $\mathbf{n_{cr}}$ is equivalent to a K^+ concentration of ~10^{-3} M). Using these conditions along with eq. A2, the surface charge density (σ) of a single nanochannel for $[KCl]_{bulk} \leq 10^{-3}$ M is estimated as a function of $\mathbf{n_{cr}}$ by

$$\sigma = \frac{\mathbf{V} \times \mathbf{e} \times \mathbf{n_{cr}}}{\mathbf{A}} \qquad \text{(eq. A3),}$$

which gives a value of 0.0006 C/m^2. From the ion density, it is possible to find the current (**I**) associated with ion transport through a nanochannel, which is approximated as[29]

$$\mathbf{I} = \mathbf{e} \times \mathbf{n} \times \mu \times \mathbf{E} \times \mathbf{S} \qquad \text{(eq. A4)},$$

where **n** is the ion density, **μ** is the K^+ mobility (= 7.6×10^{-8} m^2/(V·s)), **E** is the electric field defined by source-drain voltage/nanochannel length ($\mathbf{V_{SD}/L}$), and **S** is the cross-sectional area of the nanochannel. The conductance (**G**) of the nanochannel array in the surface charge-governed regime at low source-drain bias is obtained by taking the derivative of the current with respect to source-drain voltage ($\mathbf{V_{SD}}$), treating the ion density (**n**) as $\mathbf{n_{cr}}$, and using eq. A3 to make the conductance a function of the surface charge density, which gives

$$\mathbf{G} = \mathbf{N} \times 4\,\mu\,\sigma\,(\mathbf{d/L}) \qquad \text{(eq. A5)},$$

where **d** is the nanochannel hydraulic diameter (= 24 nm), **L** is the nanochannel length (= 20 micrometers), and **N** is the number of nanochannels (80) in the array. To account for enhanced ion transport at high source-drain bias, eq. A5 is modified to

$$\mathbf{G} = \mathbf{N} \times 4\,\mu\,\sigma\,(\mathbf{d/L})\,(\mathbf{1} + \mathbf{b}/l_{stern}) \qquad \text{(eq. A6)},$$

where **b** is the extrapolated slip length, and l_{stern} is the thickness of the Stern layer (~0.3 nm), which is also the distance over which the shear plane moves when shifting from no-slip to slip conditions. The relation shown in eq. A5, $\mathbf{G = N \times 4\mu\sigma(d/L)}$, represents electrokinetic conductance through the nanochannels without considering slip (**b** = 0), as shown in **Figure 2.9**. The extra term, $1 + \mathbf{b}/l_{stern}$, presented in eq. A6, represents the

conductance enhancement due to slip[1,2]. For conductance in the zero-slip regime, the measured conductance (~14.4 pS) was almost identical to the value (~16.8 pS) obtained using eqs. A3 and A5.

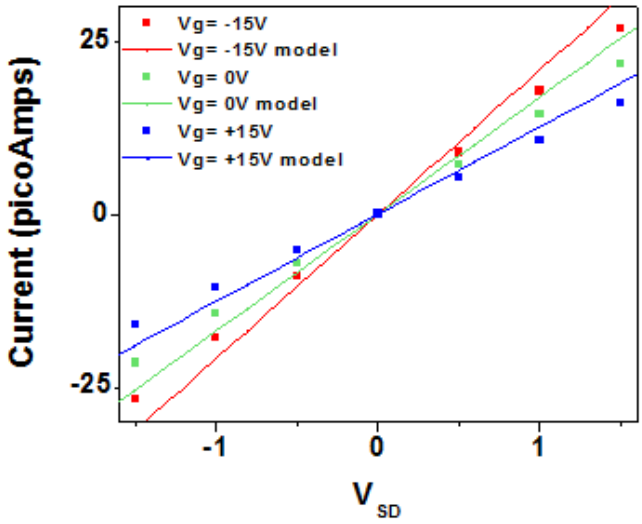

Figure 2.9. Model of gated KCl I_{SD}-V_{SD} curves. I-V curves were obtained for the nanochannel array at low source-drain bias for V_g = -15 V, 0 V, and +15 V. Squares represent experimental data points, and solid lines are based on a calculation of the conductance equation (eq. A5) without the slip-enhancement term so that **b** = 0.

2.8 Appendix C: Mechanical Power Calculations

The mechanical power output of the device – the kinetic energy per unit time associated with electroosmotic movement of fluid through the nanochannel – is defined by

$$\textbf{Mechanical Power} = \frac{1}{2}(\rho \upsilon_{eof} A)\upsilon_{eof}^2 \qquad \text{(eq. A7)},$$

where υ_{eof} is the electroosmotic flow velocity, ρ is the fluid density, A is the cross-sectional area, and $\rho\upsilon_{eof}A$ is the mass flow rate. To obtain the mechanical power output enhancement from the nanochannel device at high electric fields, we first calculate the electroosmotic flow velocity (υ_{eof}) of a KCl solution with a saturated nanochannel concentration of 10^{-3} M in the low voltage no-slip region and in the absence of a gate voltage by applying the Helmholtz-Smoluchowski equation[30]:

$$\upsilon_{eof} = \frac{\zeta \varepsilon E}{\eta} \qquad \text{(eq. A8)},$$

with η the viscosity of water, ε the permittivity, and E the electric field. ζ is the zeta potential at the shear plane, which can be derived from our previously calculated surface charge density (σ) via the Grahame equation[31]:

$$\sigma^2 = \frac{\varepsilon k_B T}{\pi} n_0 \left[\cosh \frac{e \zeta}{k_B T} - 1\right] \qquad \text{(eq. A9)},$$

where $k_B T$ is the thermal energy, and n_0 is the ion charge density within the nanochannels. This gives an electroosmotic velocity of 3.25×10^{-4} m/s at a source-drain bias of 1 volt.

The electroosmotic current (I_{eof}) can be determined from the electroosmotic velocity value by

$$I_{eof} = n_0 \upsilon_{eof} S \qquad \text{(eq. A10)},$$

where S is the cross-sectional area of all 80 nanochannels, resulting in a value of 1.5 picoAmps. This makes up roughly 10 % of the total experimentally measured current of 14.4 picoAmps at 1 volt, although electroosmotic flow has been theoretically shown to contribute up to 25 % of ion current in nanochannels[32].

Thus, assuming that electroosmotic flow accounts for between 10 % and 25 % of the total current, a linear extrapolation of the current from the no-slip, low bias region to higher voltage values results in an electroosmotic velocity of approximately 0.008 – 0.02 m/s at 25 volts. Extracting out the slip-enhanced velocity from the current in the experimental KCl I-V curve with V_g = +15 V shown in **Figure 2.5** using eq. A10 gives a value of ~1.7 m/s at 25 volts. We assume that electroosmotic flow dominates the current above the slip threshold voltage, so that the velocity value of 1.7 m/s is the electroosmotic velocity. Therefore, fluid velocity is enhanced about 80 – 200 times.

We can convert the velocity increases into mechanical power enhancement using eq. A7 above, which shows that mechanical power increases as the cube of the electroosmotic fluid velocity. Comparing slip-enhanced fluid flow to fluid transport confined by the no-slip boundary condition results in a calculated mechanical power output enhancement factor of approximately $5 - 6$ orders of magnitude at 25 volts.

2.9 Appendix D: Differential Conductance of Potassium Chloride

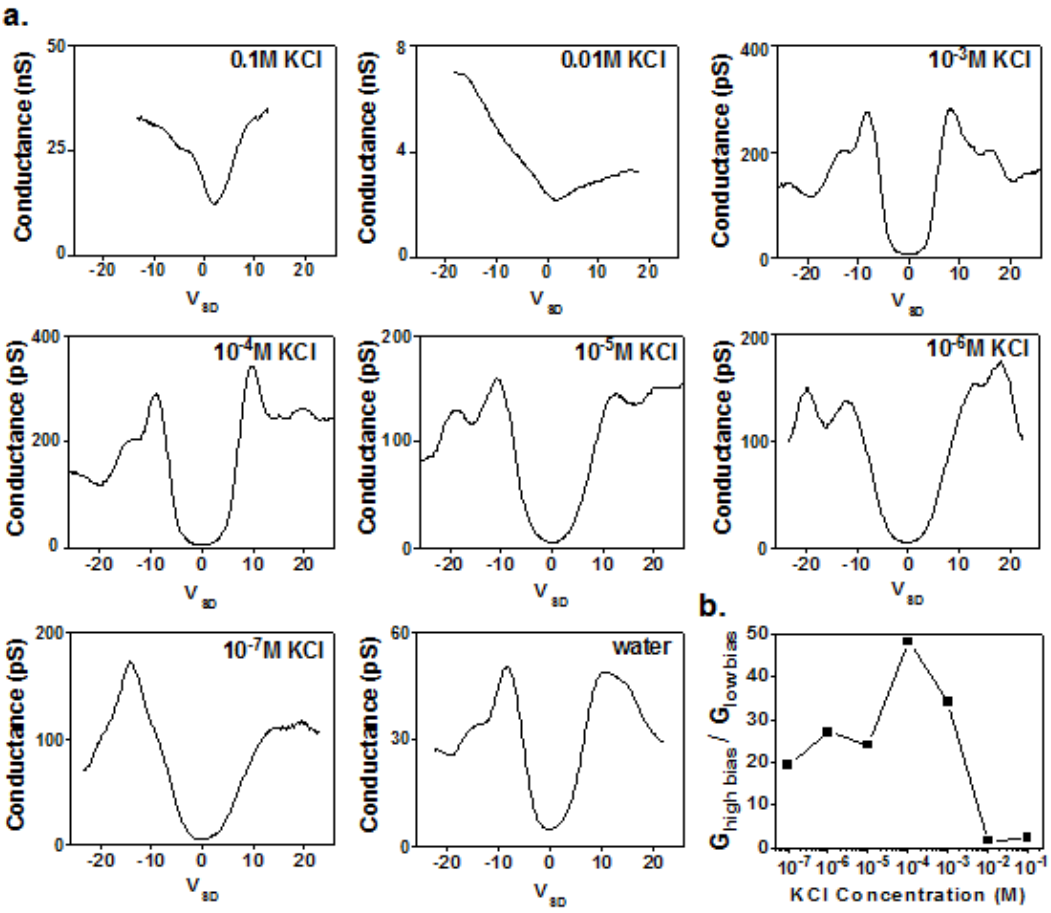

Figure 2.10. KCl differential conductance plots. **a.** Differential conductance curves for [KCl] from 10^{-1} M to 10^{-7}M and for water with a V_{SD} sweep from -25 V to +25 V. For [KCl] ≤ 10^{-3}M, the conductance plots exhibit a distinctive well shape, reflecting the nonlinear nature of the KCl I-V curves. A first (positive bias) conductance maximum occurs at V_{SD} ~ 8.5 V for [KCl] = 10^{-3}M. As [KCl] is reduced to 10^{-7}M, the well shape broadens, and that conductance maximum shifts gradually to higher voltage. **b.** A plot of the conductance increase versus [KCl]. For this plot, the value of the conductance, averaged over a 1 V range centered at the first conductance maximum, is divided by the conductance at low bias, averaged between -1 V and +1 V. The conductance increases between 20-fold and 50-fold, depending upon [KCl].

Chapter 3

Plasma Proteome Profiling of Glioblastoma Multiforme using DNA-Encoded Antibody Microarrays: Characterizing Biomarker Signatures of Disease and Treatment Response

3.1 Introduction

Glioblastoma multiforme (GBM) [WHO grade IV astrocytoma] is the most common primary brain tumor in adults and the most aggressive form of glioma[1]. Due to its highly proliferative and infiltrative nature, GBM carries the poorest prognosis of any cancer, with a median patient survival of ~12 months, despite major advances in chemotherapy, radiation therapy, and surgery over the last few decades[2]. Although glioblastoma patients share many disease features in common, the fact that patients can differ tremendously in their response to therapy suggests that the cancer is molecularly heterogeneous. Indeed, it is known that genetically, there are two routes of glioblastoma development. Primary or de novo GBM, which is typically characterized by sudden onset

of high grade malignancy and an older age of onset, involves EGFR amplification and inactivation of the PTEN gene due to loss of heterogeneity at chromosome 10[3,4]. Secondary GBM, which is defined by progression from a lower-grade astrocytoma, and often presents at a younger age, initially involves chromosome 17 deletions and inactivation of the p53 gene, followed by a series of other mutations as the tumor undergoes malignant transformation[2-4]. However, even within these two broad categories, patients differ in the types of subsequent chromosomal alterations and mutations their tumors exhibit, as well as in rates of tumor growth and progression, overall survival, and types of treatments to which they respond.

Gene expression profiling has been instrumental in further elucidating key molecular players involved in GBM growth and progression, as well as the supporting cast of molecules that exhibit less pronounced changes[5,6], greatly facilitating the search for candidate GBM biomarkers. However, gene expression profiling provides a window only to RNA expression levels, whereas much of the information processing within the cell occurs at the level of protein network interactions. Often the relationship between RNA and protein expression level is nonlinear[7] due to additional transcriptional and post-transcriptional controls[8,9]. Therefore, key drug targets could be differentially expressed at the protein level but not the RNA level[10]. In addition, post-translational processing and modifications can alter the activities of proteins and their locations within the cell[8]. This information cannot be obtained solely by profiling gene expression.

Proteomic approaches pick up where genomic approaches leave off by allowing one to survey disease-related changes in global protein expression, find correlations between proteins that are similarly differentially expressed, and analyze those changes in

the context of known or prospective protein signaling pathways and networks. In particular, antibody-based microarray technology has facilitated the simultaneous high-affinity profiling of numerous proteins from relatively small samples of cell and tissue lysates, culture media[7], and bodily fluids, such as blood[11], urine[12], saliva, tears[13,14], and cerebrospinal fluid[15]. The advantages of this form of multiplexed protein detection over other approaches, such as 2D-PAGE and mass spectrometry, are its higher throughput and sensitivity, scalability, ease of use, cost-effectiveness, smaller sample requirements (< 50 µL), straightforward protein quantitation, and its ability to detect low abundance plasma proteins without the need for tedious protein fractionation steps[7,11,16]. As such, this technology represents a promising platform for novel disease-biomarker discovery. In addition, because small quantities of sample are sufficient to obtain enormous amounts of information, new opportunities are afforded for minimally-invasive diagnosis, stratification, and monitoring of cancer patients[16].

Blood is an ideal fluid for minimally-invasive detection of cancer-associated markers[17]. Cancer cells, like any other cell, secrete proteins into the bloodstream that can provide important information about their physiological and pathological state[17]. As well, intracellular proteins and cell-surface receptors are released into the circulation when cancer cells die. Antibody-based microarrays can permit the simultaneous, sensitive detection of many of these circulating factors from very small sample volumes – as little as a fingerprick's volume worth of blood (10 – 50 µL)[16]. It might nevertheless be expected that plasma detection of brain tumor markers would be challenging because the blood-brain barrier (BBB) greatly limits the free passage of proteins and other molecules between the two compartments[18]. However, the integrity of this barrier becomes greatly

compromised at sites of inflammation[19] or neovascularization[20-22], which both typically accompany glioblastoma tumors. In addition, glioblastoma tumors secrete soluble factors that disrupt the blood-brain barrier[23].

Unfortunately, for the vast majority of cancers and other diseases, no biomarkers have thus far been discovered with adequate specificity and sensitivity for whole-population screening or disease monitoring. Relatively few serum biomarkers have been FDA-approved for cancer monitoring, and just one – prostate specific antigen (PSA) – is approved for disease screening[24]. Likewise for glioblastoma, although gene expression profiling has allowed for the discovery of numerous protein biomarker candidates, none of these proteins on its own has achieved broad application for routine clinical diagnosis, prognosis, or monitoring of GBM, or for evaluating or predicting therapeutic response[25].

However, it has become increasingly recognized that large panels of proteins, in which each component protein has relatively poor disease specificity on its own, can, as a group, provide a highly sensitive and specific molecular signature of disease[26,27]. A number of studies have demonstrated the ability of antibody-based microarrays to identify protein expression patterns that can discriminate between patients with cancer (of the bladder[28], pancreas[29], prostate[30], or stomach[31]) and normal controls. In theory, a sufficiently informative protein biomarker panel could stratify a given disease into subgroups based on unique molecular phenotypes, much as has been shown in gene expression profile studies[5,10]. Treatments could then be customized to the tumor's specific set of molecular alterations. This would greatly contrast with the current expensive and time-consuming trial-and-error, watch-and-wait approach of administering a chemotherapeutic, awaiting a response, and then changing the medication if no

response is achieved. All the while, the patient's tumor continues to advance in grade and stage.

The routine use of antibody-based microarrays for multiplexed, high-throughput plasma biomarker detection and patient classification requires that these platforms be created using standardized methods that optimize sensitivity, reproducibility, cost, and compatibility with microfluidic chip based environments. While many approaches for arraying antibodies on slide surfaces have been investigated, DNA-directed antibody immobilization provides a number of unique advantages in this regard. For one thing, as compared to directly spotted antibodies, DNA-tethered antibodies exhibit less denaturation and possess greater orientational freedom, allowing a larger proportion of antibodies to be oriented such that their binding sites are accessible to cognate antigens[32,33]. Studies have also shown that this approach offers improved spot homogeneity and reproducibility, and far more economical use of antibody materials[32]. Importantly, for multiplexed point-of-care diagnostics, DNA-directed immobilization is amenable to microfluidic chip assembly because the antibodies can be arrayed subsequent to bonding of the PDMS stamp with the DNA-spotted slide – a thermal process that would otherwise destroy the antibodies[16,33].

The goal of the present study was to determine whether a plasma protein signature could be elucidated that would be able to differentiate patients with glioblastoma (n = 46) from healthy controls (n = 47) via a simple blood test that uses close to fingerprick volumes ($\leq$ 50 µL) of blood. We also sought to elucidate a plasma biomarker signature indicative of tumor growth – and, conversely, treatment response – in Avastin-treated GBM patients. Our platform consisted of capture-antibody arrays created by DNA-

directed assembly within ELISA-like wells. These antibodies were targeted against 35 distinct proteins known to be generally associated with tumor growth, survival, migration, invasion, angiogenesis, and immune-regulation. The platform allowed us to profile even low-abundance analytes (such as cytokines and growth factors) in plasma using microliter-scale sample volumes. We detected a number of proteins that were differentially expressed with high statistical significance ($p < 0.05$), allowing us to use these plasma biomarker signatures to classify patients into the aforementioned experimental and control groups with high sensitivity and specificity.

3.2 Materials and Methods

3.2.1 DNA-encoded antibody libraries (DEAL) technique

The antibody assembly platform used here is based on the DNA-encoded antibody library (DEAL) method, which has been reported elsewhere by our group[33]. When DEAL is utilized to measure proteins, it is used as follows (**Figure 3.5** in Appendix). Capture antibodies (CAs) against the protein of interest are chemically labeled with single-stranded DNA (ssDNA) oligomers, yielding ssDNA-CA conjugates. The coupling reaction is accomplished using succinimidyl 4-formylbenzoate (SFB, Solutink) and Succinimidyl 4-hydrazinonicotinate acetone hydrazone in *N*,*N*-dimethylformamide (DMF) (SANH, Solulink) as conjugation agents to link amine termini on DNA oligomers to the amine side-groups of proteins. A size-exclusion column is used to purify the product by removing excess unreacted DNA molecules. Separately, the complementary ssDNA oligomers (100 μM in a 50 % DMSO/water mixture) are

spotted onto a poly-L-lysine coated glass slide (150 μm spots spaced 300 μm center-to-center) using an array spotter (VersArray Chip Writer Pro, BioRad). Each spot also contains 10 μM of oligo **M** as a spot loading control. At the beginning of a DEAL protein assay, incubation of ssDNA-CA conjugates with the complementary spatially-patterned ssDNA array assembles the CAs onto those specific sites through DNA hybridization. This step transforms the DNA microarray into an antibody microarray that is ready for a protein sandwich assay. Biological samples (i.e. plasma isolated from human whole blood) can be applied onto the CA microarray and antigens can be captured. Finally, detection antibodies and/or fluorescent read-out probes are introduced sequentially to complete the immuno-sandwich assay. DNA oligomer sequences are chosen with appropriate melting temperatures to optimize 37 ^{o}C hybridization to complementary strands while minimizing cross-hybridization (< 5 % in fluorescence signal).

3.2.2 Antibody array platform

Our platform consists of ELISA-like wells assembled by bonding a PDMS slab with square holes to a poly-lysine coated glass substrate onto which 6 x 6 oligonucleotide arrays have been pre-spotted. Thirty-five distinct DNA-addressed antibodies are directed to their complementary spots during the assay. The assay wells accommodate up to 200 μL of sample, but in fact, only about 20 – 50 μL are needed to obtain a reasonable signal-to-noise. We used 50 μL of plasma for all of our assays.

3.2.3 Multiplexed assays on patient plasma

Each microarray well (12 wells/slide) was first blocked with 200 μL of blocking buffer – 3 % wt/vol bovine serum albumin fraction V (Sigma) in 150 mM 1x PBS

without calcium/magnesium salts (Irvine Scientific) – for 1 hour in a 37 ^{o}C incubator. The wells were then aspirated, and 50 µL of a cocktail containing 35 different DNA-antibody conjugates (50 nM each) in blocking buffer were pipetted into the wells to transform the DNA arrays into capture-antibody arrays. After incubation at 37 ^{o}C for 1 hour, the wells were aspirated, and then rinsed with blocking buffer 4 – 5 times to remove excess unbound conjugate. At this step, the wells were ready for the blood test. Fifty-microliter undiluted plasma samples were added to each well and allowed to incubate for 1 hour at 37 ^{o}C. The samples were then aspirated and each well was again rinsed 4 – 5 times with blocking buffer. Next, a cocktail containing the 35 biotinylated detection antibodies (50 nM each) in blocking buffer was added to each well (50 µL) and was allowed to incubate for 1 hour at 37 ^{o}C. The wells were aspirated and rinsed 4 – 5 times with blocking buffer, followed by incubation of a solution containing 50 nM Streptavidin-Cy5 (eBioscience) and 50 nM **M'**-Cy3 for 1 hour at 37 ^{o}C. The wells were aspirated, and rinsed 4 – 5 times with blocking buffer. The PDMS well template was then peeled off the slide within a blocking buffer bath, and the slide was allowed to incubate in the bath for 1 minute at room temperature. The slide was then immersed in 150 mM 1x PBS, 1/2x PBS, and twice in deionized water in separate 50 mL falcon tubes for 1 minute, 10 seconds, and 2 seconds, respectively. The slide was then spun dry and scanned by a fluorescence microarray scanner.

3.2.4 Plasma collection and processing

Blood samples were collected by standard phlebotomy techniques in 10 mL blood collection tubes containing ACD-A anticoagulant (BD Vacutainer yellow-top glass tubes). The samples were centrifuged at *1500 x g* for 15 minutes, and the plasma was

collected and subdivided into 200 µL aliquots. Care was taken to ensure that plasma samples were frozen at -80 ^{o}C within 2 hours of collection to minimize degradation of plasma proteins by proteases. Each aliquot was thawed just once as needed.

3.2.5 Data processing and statistics

Post-assay, all array slides were scanned using a two-color laser fluorescence microarray scanner (GenePix 4200A Professional, Axon Instruments) at the same instrument settings – 70 % and 50 % for the laser power of the 635 nm and 532 nm channels, respectively. Optical gains were 550 and 500 for the 645 nm and 532 nm channels, respectively. Spot intensities were quantified with the software program GenePix Pro 6.0 using the fixed circle method. For each sample, the local background was subtracted from each spot, and the average and standard deviation were taken for each of the 35 sets of six repeated spots. A semi-global normalization method was used for chip-to-chip normalization. Briefly, the coefficient of variation (CV) was calculated for each analyte over all samples and ranked. The 15 % of analytes (5 analytes) with the lowest CV-values were used to calculate the normalization factor $N_i = S_i/\mu$, where S_i is the sum of the signal intensities of the 5 analytes for each sample, and μ is the average of S_i from all samples. The dataset generated from each sample was then divided by the normalization factor N_i. Universally, all datasets contained at least 4 analytes that had comparable intensities to negative controls run in separate experiments. Therefore, the net intra-assay intensities were calculated by subtracting each background-corrected analyte intensity by the mean intensity of the 4 lowest-intensity analytes. Unsupervised two-way average linkage hierarchical clustering (Cluster 3.0) was then performed on an entire patient cohort data set, and the resulting heatmap and dendrogram were viewed

using Java TreeView. The statistical significance (both Mann-Whitney and t-test *p*-values) of differential protein expression between experimental and control groups was analyzed using the *AnalyseIt* add-in for Microsoft Excel. This add-in was also used to generate box plots for each measured analyte across each study group.

3.2.6 Classification of patients

Two-by-two contingency tables and diagnostic parameters – sensitivity, specificity, negative predictive value (NPV), and positive predictive value (PPV) – were calculated by repeated random sub-sampling cross-validation. An Excel macro developed in-house was used to randomly assign 10 patients to a test set, leaving the remainder of patients as the training set. Unsupervised two-way average linkage hierarchical clustering (Cluster 3.0) was then performed on the entire patient cohort dataset (now containing 10 unknowns) and the resulting heatmap and dendrogram were viewed using Java TreeView. The ten unknown patients were then manually classified as belonging to the experimental (Group A) or control group (Group B) based on the following decision rules (x = fraction of members within the unknown's cluster that belong to same group):

1. The minimum number of clusters incorporating the unknown and at least 5 other members is analyzed. If all members of this cluster fall into the same group (x = 1), the unknown is classified as a member of that group with high confidence (this is considered a homogeneous zone). If $x > 0.75$, the unknown is still considered to be part of the majority group (with average confidence) but the cluster is no longer considered a homogeneous zone. If $x < 0.75$, then…

2. The minimum number of clusters incorporating the unknown and at least 8 other members is analyzed. If now $x > 0.75$, the unknown is considered to be part of the majority group. If $0.5 < x < 0.75$, the unknown is still considered to be part of the majority group, but with low confidence. In this case…

3. The minimum number of clusters incorporating the unknown and at least 14 other members is analyzed using the same decision rules as in 2.

4. If $x \sim 0.5$ after step 3, then the unknown remains unclassified and is removed from the analysis. Alternatively, an $x \sim 0.5$ is sufficient to remove the unknown sample from the analysis even if the unknown is grouped within a smaller cluster if the members of that cluster are closely correlated, yet far less correlated with the nearest neighboring cluster.

5. If in step 1, the unknown is part of a cluster containing 4 or fewer members that are all highly correlated with each other relative to the nearest neighboring cluster, the unknown is assigned to the majority group with low confidence if $0.5 < x < 0.66$, average confidence if $0.66 < x < 0.75$ and high confidence if $x = 1$.

6. If two or more unknowns are nearest neighbors, these unknowns remain unclassified and are removed from the analysis.

This random sub-sampling was then repeated 10 times with replacement (100 unknown events), such that some patients may have been randomly assigned to a test sample more than once, while others not at all. An Excel macro developed in-house then compared the predicted and actual classifications, and output the total number of true-positives, false-positives, true-negatives, and false-negatives in a 2 x 2 contingency table, as well as the sensitivity, specificity, NPV, and PPV of the diagnostic evaluation. This constituted the full diagnostic evaluation for a dataset. For the two patient cohorts examined in this study, diagnostic evaluation was also performed on trimmed datasets consisting of subsets of *n* proteins (from the initial 35-protein panel) that exhibited the most statistically significant differential expression between experimental and control groups (where n = 3, 6, 9, 12, 16, 20, 25). For each dataset, points were plotted in ROC space (sensitivity vs. 1 – specificity) to assess the predictive power of the test.

3.3 Results

3.3.1 Evaluation of DNA directed antibody microarrays

Preliminary experiments were run in advance to validate a set of 35 orthogonal oligos that exhibited minimal cross-hybridization (< 5%). In addition, the full panel of DNA-conjugated antibodies was validated with a set of cognate recombinants to ensure that there was minimal cross-talk between each recombinant and non-cognate spots. Each DNA spot was loaded with reference DNA (10 %), which, once hybridized with a dye-conjugated complement, served as a DNA-loading control. For each oligo, the spot loading was highly consistent both across an entire slide as well as between slides.

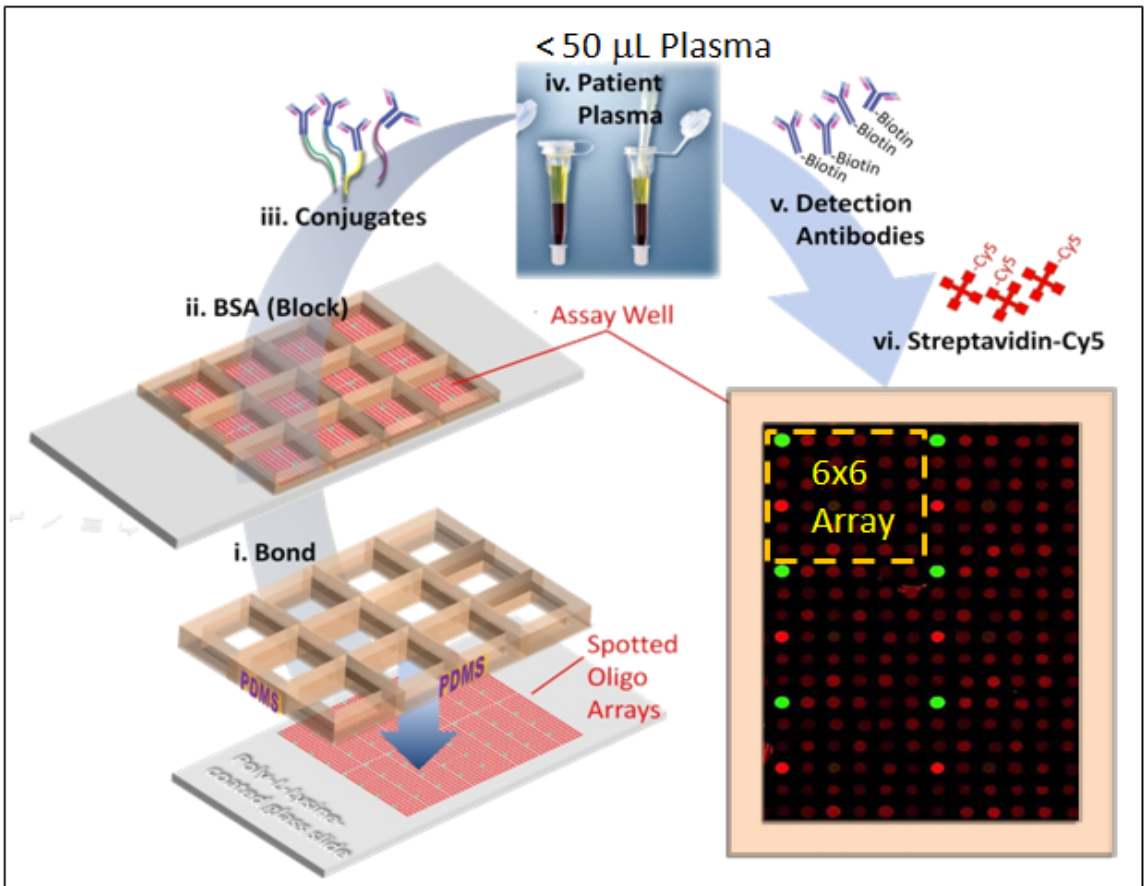

Figure 3.1. Assay platform and methodology. Polylysine-coated slides were spotted with 36 distinct oligos in 6 x 6 array repeats. **i**. A PDMS slab containing square holes was set on top of the spotted substrates, forming ELISA-like assay wells. Assays were performed by **ii**. blocking the wells with BSA, **iii**. incubating with conjugates to transform the DNA microarray into an antibody microarray, **iv**. adding a different patient plasma sample to each well, **v**. incubating with biotinylated detection antibodies, **vi**. adding Streptavidin-Cy5 (Red Spots) and **M′**-Cy3 (Green Reference Spot), with rinses between steps. Each well contained six full repeats of the 6 x 6 antibody arrays. The platform was used to detect 35 distinct proteins from 40 – 50 µL of plasma. Readout was performed with a flourescence scanner.

The fluorescent readouts from all plasma samples assayed on the 35-plex antibody array platform were analyzed for spot homogeneity, reproducibility, and signal-to-noise. A representative image of the fluorescent readout from a single assay well is shown in **Figure 3.1**. Each well contained a total of six repeats of 6 x 6 spot arrays (35 antibodies + 1 green Cy3-conjugated reference oligonucleotide). The spots are circular, well-defined, and radially homogeneous. There was very little intra-assay variation in the

intensities of each set of 6 spot repeats. In addition, spot intensities tended to be highly consistent even between duplicate assays run on separate slides.

3.3.2 Classification of GBM patients versus healthy controls

We compared plasma samples from 46 GBM patients (72 samples: for some patients, plasma samples from multiple collection dates were available) with those of 47 healthy controls with respect to the plasma levels of 35 different proteins known to be generally associated with tumor growth, survival, invasion, migration, and immunoregulation. Two-way average-linkage hierarchical clustering allowed these two groups to be discriminated with a sensitivity and specificity of 84 ± 15 % and 89 ± 31 %, respectively (**Figure 3.2a**). The heat map is divided into numerous islands of GBM patient, healthy control, and mixed population clusters without a clean separation between the two groups. We then sought to determine whether the diagnostic accuracy could be improved by removing those test samples from diagnostic evaluation that did not fall into highly homogeneous clusters (i.e. > 70% of the cluster members belong to the same group). Within the subpopulation of test samples that fell into highly discriminatory clusters, the sensitivity and specificity improved to 90 ± 14 % and 94 ± 8 %, respectively, albeit with a diagnosable population size that was 70 % of the original. Among test samples that clustered entirely with members of a single group ("homogeneous zones"), the sensitivity and specificity both approached 100 %. Thirty percent of samples fell into one of these homogeneous zones, allowing that subpopulation to be diagnosed with near-perfect accuracy.

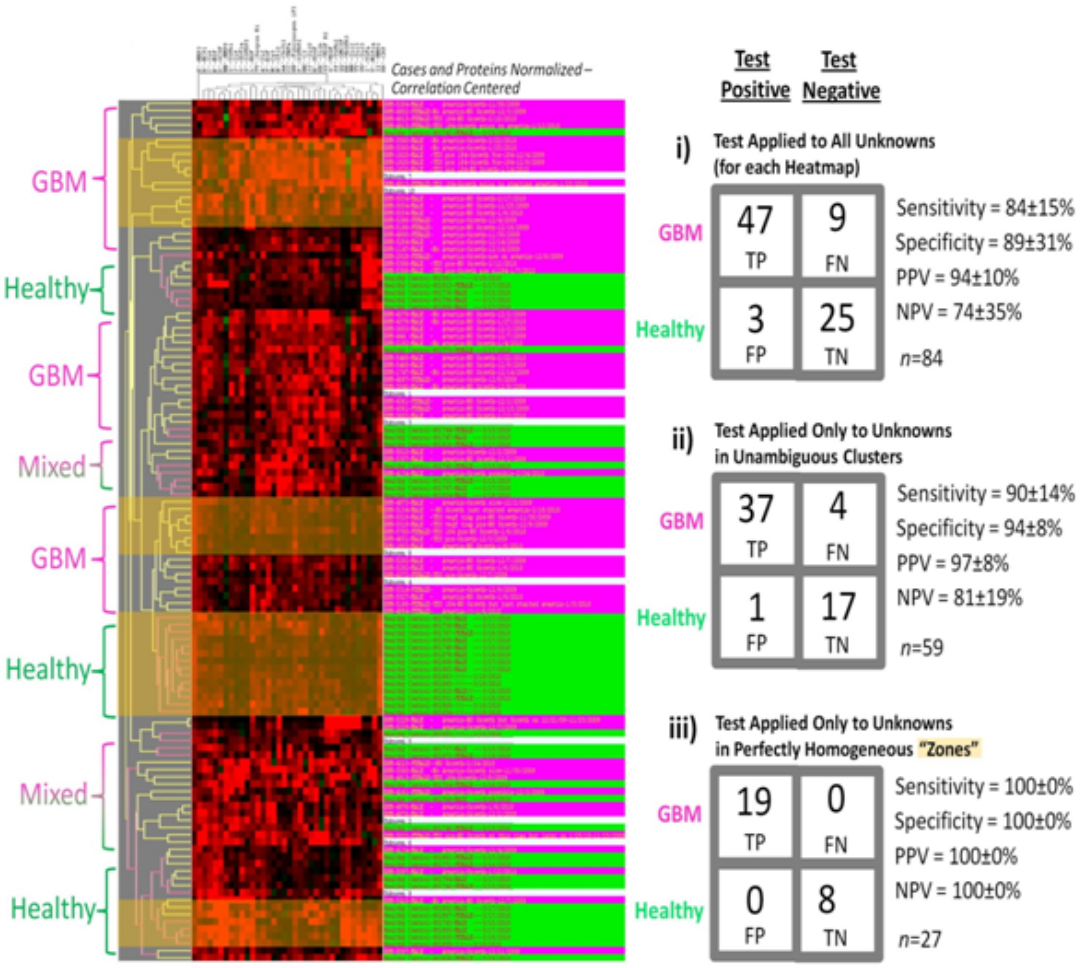

Figure 3.2a. GBM patients vs. healthy controls
Average linkage hierarchical clustering (unsupervised) was performed on 35-protein datasets from each of 72 GBM patient plasma samples and 47 Healthy Control samples. A computer program was used to randomly assign patients to trial and test sets (multiple times), and the tumor growth status of each test set member (unknown) was predicted based on the status of nearest neighbors in its cluster. 2x2 tables were generated and relevant statistical parameters calculated for diagnostic tests that evaluated: **i)** all unknowns on the heatmap; **ii)** unknowns in clusters where a sizeable majority of members -including the nearest neighbor - shared the same status; **iii)** unknowns in completely homogeneous clusters where *all* members shared the same status - so-called "homogeneous zones" (highlighted).

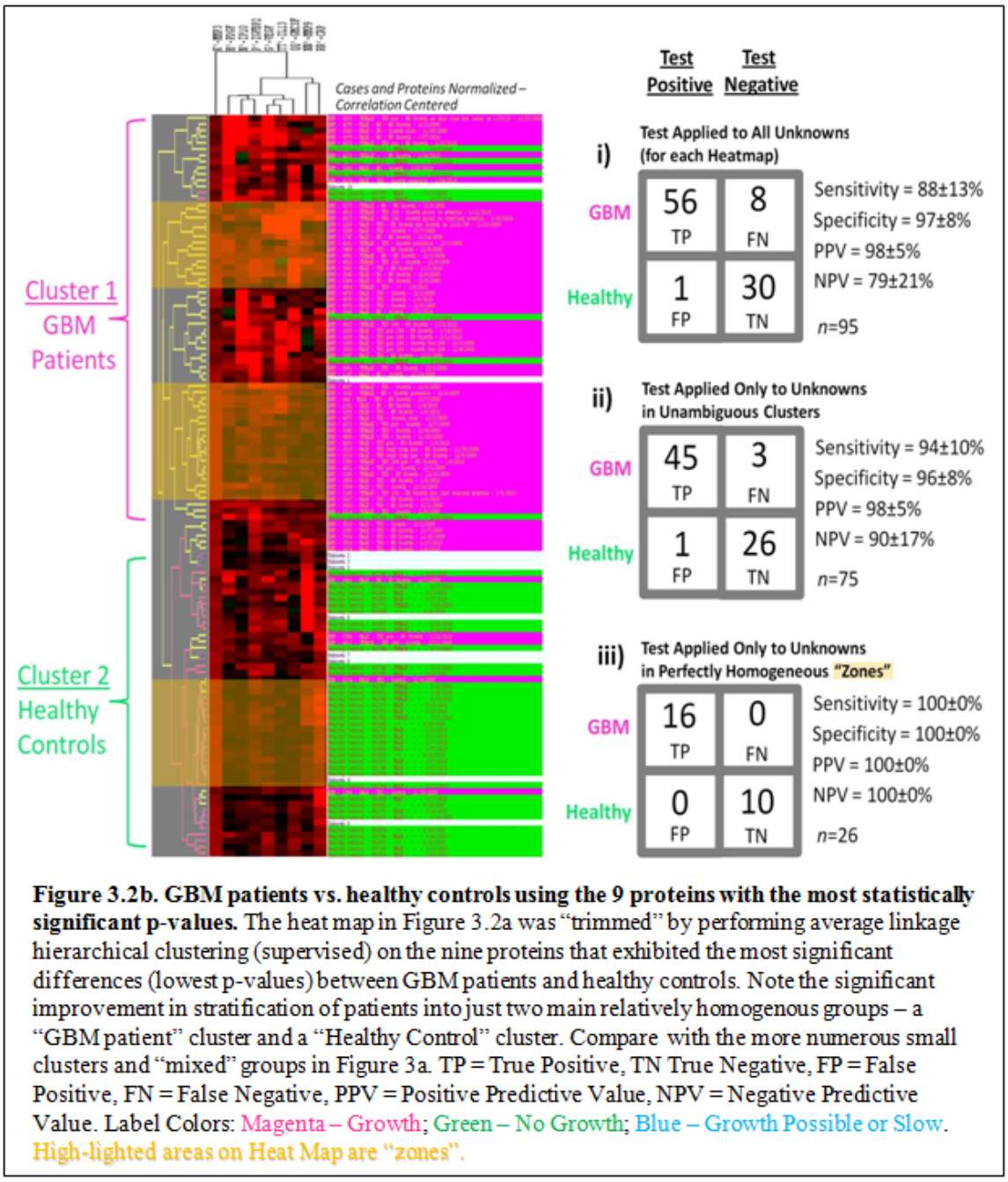

Figure 3.2b. GBM patients vs. healthy controls using the 9 proteins with the most statistically significant p-values. The heat map in Figure 3.2a was "trimmed" by performing average linkage hierarchical clustering (supervised) on the nine proteins that exhibited the most significant differences (lowest p-values) between GBM patients and healthy controls. Note the significant improvement in stratification of patients into just two main relatively homogenous groups – a "GBM patient" cluster and a "Healthy Control" cluster. Compare with the more numerous small clusters and "mixed" groups in Figure 3a. TP = True Positive, TN True Negative, FP = False Positive, FN = False Negative, PPV = Positive Predictive Value, NPV = Negative Predictive Value. Label Colors: Magenta – Growth; Green – No Growth; Blue – Growth Possible or Slow. High-lighted areas on Heat Map are "zones".

We then repeated the cluster analysis with a trimmed panel that included only the nine proteins with the most statistically significant (Mann-Whitney and t-test p-values < 0.05) differential expression (**Figure 3.2b**). These included: MMP3, PDGF, IP10, IGFBP2, VEGF, IL13, GM-CSF, MMP9, and CRP. The resultant heat map shows far improved classification of GBM patients and healthy controls into two separate clusters,

with few misclassifications in each cluster. By using this trimmed protein panel, the sensitivity and specificity achieved were 88 ± 13 % and 97 ± 8 %, respectively. As before, those samples (20 % of the sample population) that did not decisively cluster with a particular group were removed from diagnostic evaluation, and the sensitivity and specificity among the resulting diagnosable population improved to 94 ± 10 % and 96 ± 8 %, respectively. Again, both sensitivity and specificity approached 100 % among test samples that clustered within perfectly homogeneous zones.

3.3.3 Diagnostic strength as a function of protein panel size

The cluster analysis was repeated for *n*-protein subsets of the original 35 protein panel, where n = 3, 6, 9, 12, 16, 20, 25, & 35 of the most statistically significant discriminators of GBM and health status. Diagnostic test sensitivity, specificity, and positive and negative predictive values were calculated for each of these subsets. Those test samples that did not decisively cluster with a particular group were removed from the evaluation. As can be seen in **Figure 3.3a**, the sensitivity and specificity remain about level as one trims the panel from 35 to 20 proteins. Both parameters increase as the panel is trimmed from 16 proteins onwards, with a peak at 6 proteins, followed by a sharp drop as the panel size is reduced further. On the other hand, the percentage of samples evaluable increases steadily as one trims the panel from 35 proteins down to 9 proteins and then tapers off. Since the strength of a diagnostic test lies not only in its diagnostic accuracy but also in the percentage of the population it can evaluate, we designated an artificial parameter *S* to represent the product of a diagnostic value and the percentage of patients diagnosable for each n-protein subset. As can be seen in **Figure 3.3a**, this parameter increases steadily as the protein panel size is reduced, peaking at 9 proteins

and then falling off sharply. Therefore, the 9-protein subset appears to optimize test performance by achieving a high diagnostic accuracy while still maintaining the ability to diagnose a large fraction of the sample population.

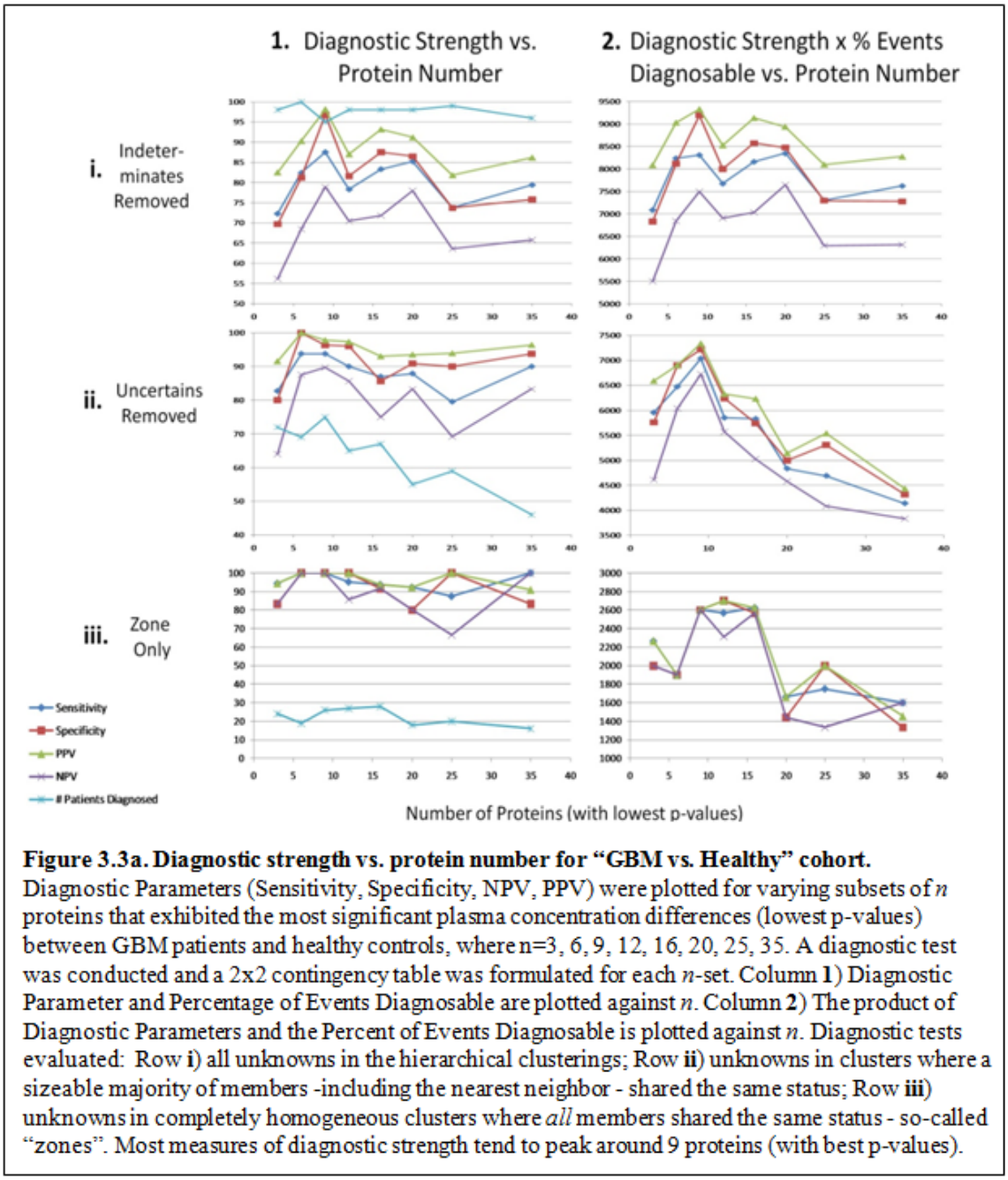

Figure 3.3a. Diagnostic strength vs. protein number for "GBM vs. Healthy" cohort. Diagnostic Parameters (Sensitivity, Specificity, NPV, PPV) were plotted for varying subsets of *n* proteins that exhibited the most significant plasma concentration differences (lowest p-values) between GBM patients and healthy controls, where n=3, 6, 9, 12, 16, 20, 25, 35. A diagnostic test was conducted and a 2x2 contingency table was formulated for each *n*-set. Column **1**) Diagnostic Parameter and Percentage of Events Diagnosable are plotted against *n*. Column **2**) The product of Diagnostic Parameters and the Percent of Events Diagnosable is plotted against *n*. Diagnostic tests evaluated: Row **i**) all unknowns in the hierarchical clusterings; Row **ii**) unknowns in clusters where a sizeable majority of members -including the nearest neighbor - shared the same status; Row **iii**) unknowns in completely homogeneous clusters where *all* members shared the same status - so-called "zones". Most measures of diagnostic strength tend to peak around 9 proteins (with best p-values).

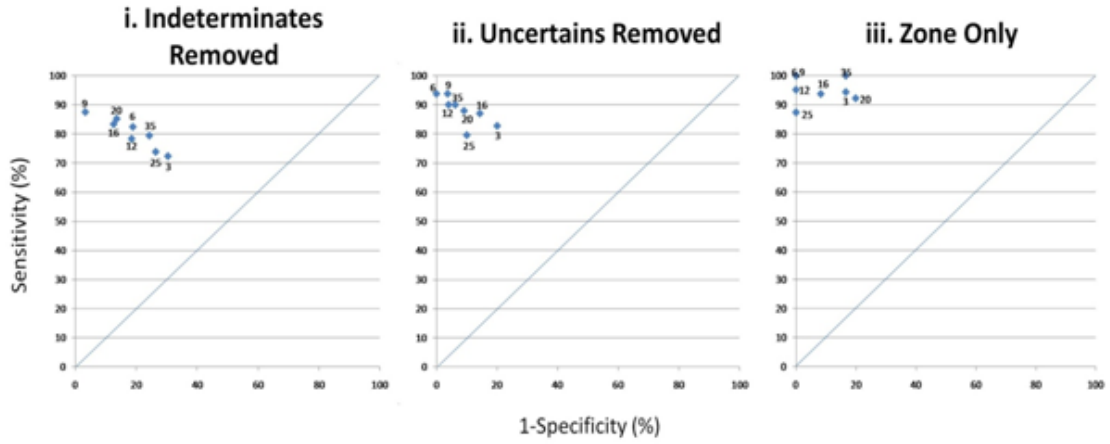

Figure 3.3b. ROC plots for "GBM vs. Healthy" cohort. Relevant diagnostic parameters for each *n*-set were plotted in ROC space. Cases **i**, **ii**, & **iii** are the same as before. Note the improvement in predictive power (distance of points from 45° line) from case **i** → **ii** → **iii**. Also note the high predictive power of the 9-set in **i.** and both the 6- & 9- sets in **ii.** and **iii.** The coordinate (0,100) represents perfect classification.

The predictive power of each *n*-protein subset for classifying GBM patients and healthy controls can also be evaluated by plotting the true positive rate (sensitivity) vs. the false positive rate (1 – specificity) for each subset. As observed in **Figure 3.3b**, the 6- and 9-protein subsets yield points in ROC (Receiver-Operating Characteristic) space that are farthest in perpendicular distance from the 45° line, suggesting that this number of differentially expressed proteins maximizes the predictive power. Points for all protein-panel subsets move farther from the diagonal line as the sample population is trimmed to include: only those samples in clusters that are highly biased – the great majority (> 70 %) of members belong to either the GBM patient or healthy control groups (as in **Figure 3.3b ii**); or, only those samples in clusters that are completely biased – all members belong to one of the two groups (as in **Figure 3.3b iii**). Perfect classification was achievable in both 6- and 9-protein subsets when analyzing only the subset of test samples that were located within perfectly homogeneous clusters. As a whole, the data in

Figure 3.3 shows that by performing cluster analysis on patient plasma samples assayed for the 6 or 9 proteins most significantly differentially expressed, a very high degree of predictive power could be achieved among samples in highly biased clusters. In addition, the 9-protein set optimized the predictive power and the number of patients diagnosable. Furthermore, a subgroup of these patients who fell into perfectly homogeneous clusters could be diagnosed with near certainty.

3.3.4 GBM patients on Avastin – classification of tumor growth vs. no growth

We then assayed plasma samples from GBM patients treated with the chemotherapeutic drug Avastin (Bevacizumab) with respect to the same 35-protein panel as before. Specifically, we compared 52 samples from 25 patients who exhibited tumor growth (according to MRI imaging) with 51 samples from 21 patients who exhibited no tumor growth since their last evaluation. Two-way average linkage hierarchical clustering allowed these two groups to be discriminated with a sensitivity and specificity of 74 ± 10 % and 78 ± 19 %, respectively (**Figure 3.4a**). When only patient samples within highly biased clusters were analyzed (45 % of the total sample population), the sensitivity and specificity improved to 90 ± 11 % and 96 ± 8 %, respectively. The sensitivity remained the same but the specificity increased to 100 % when test samples only in perfectly homogeneous clusters were analyzed (20 % of sample population).

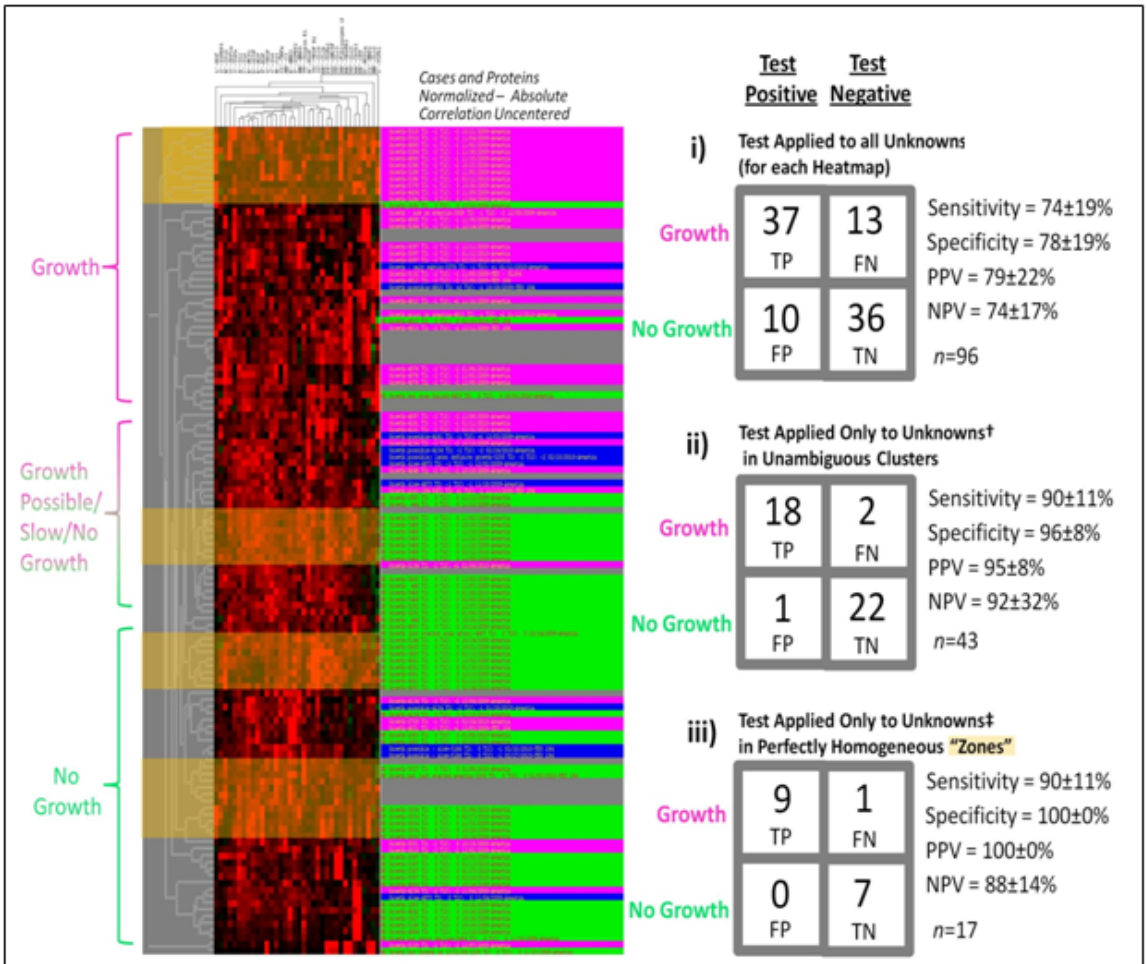

Figure 3.4a. GBM patients on Avastin – tumor growth vs. no growth. Average linkage hierarchical clustering (unsupervised) was performed on 35-protein datasets from each of 122 plasma samples derived from GBM patients treated with Avastin. A computer program was used to randomly assign patients to trial and test sets (multiple times), and the tumor growth status of each test set member (unknown) was predicted based on the status of nearest neighbors in its cluster . 2x2 tables were generated and relevant statistical parameters calculated for **i)** all unknowns in the heatmap; **ii)** only unknowns in clusters where a sizeable majority of members -including the nearest neighbor - shared the same status; **iii)** only unknowns in completely homogeneous clusters where *all* members shared the same status - so-called "zones" (highlighted). TP = True Positive, TN True Negative, FP = False Positive, FN = False Negative, PPV = Positive Predictive Value, NPV = Negative Predictive Value. High-lighted areas on Heat Map are "zones".

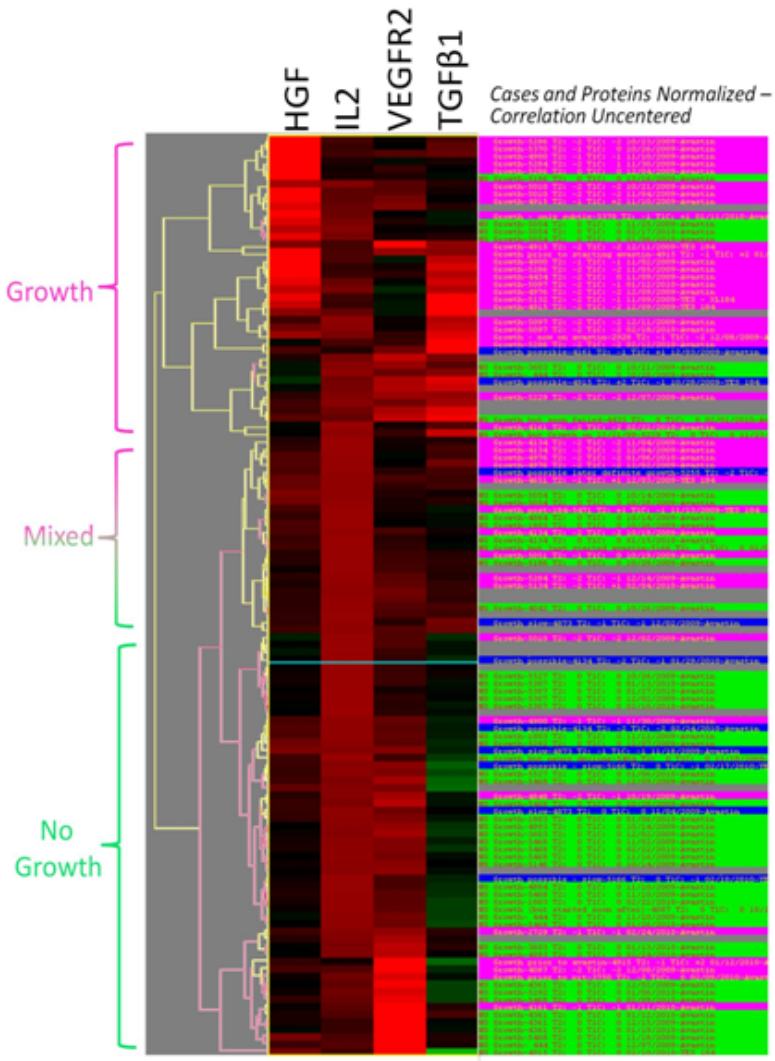

Figure 3.4b. GBM patients on Avastin – tumor growth vs. no growth – using the 4 proteins with the most statistically significant p-values. The heat map in Figure 3.4a was "trimmed" by performing average linkage hierarchical clustering (supervised) on the four proteins that exhibited the most significant differences (lowest p-values) when comparing patients with tumor growth to those with no growth. Patients with high HGF and/or high TGFβ1 levels tended to exhibit tumor growth, while patients with high VEGFR2 levels and/or low TGFβ1 tended to exhibit no tumor growth.

The heat map is divided into 3 main sections consisting of samples from: 1. patients whose tumors have grown since their last evaluation (recurrence); 2. patients whose tumors have remained stable since their last evaluation (no recurrence); and 3. a mixed population of patients exhibiting either possible, slow growth or no growth. The

patient samples were then clustered with respect to the 4 proteins that were differentially expressed with the highest statistical significance (Mann-Whitney/t-test $p < 0.05$). **Figure 3.4b** shows clustering of patient samples into 3 main groups: 1. tumor growth; 2. no tumor growth; and 3. mixed population: consisting of both patients with and without tumor growth. Particularly notable is that serum levels of HGF and TGFβ1 appear to be highly upregulated in the tumor growth group as compared with the no growth group. The cytokines MIP1α and IL12 (not shown in the heatmap) are also highly upregulated in the growth group. In addition, VEGFR2 appears to be highly down-regulated, while IL2 is only somewhat downregulated, in the growth group compared with the no growth group. The alterations in cytokine levels observed in the sera of patients with growing tumors with respect to non-growing tumors may not necessarily be attributable to changes in tumor production and secretion of these cytokines. Rather, they may actually reflect changes in systemic responses to the growing tumor, such as inflammatory-associated or other immune-mediated responses.

3.4 Discussion

While antibody microarrays have been used in the past to profile cancers of the lung, liver, ovary, prostate, pancreas, colon, and bladder, this is the first study demonstrating their use for plasma profiling of glioblastoma. In this study, we have shown that by interrogating a relatively large panel of 35 plasma proteins, biomarker signatures could be straightforwardly elucidated that could differentiate GBM patients from healthy controls, and that could classify GBM patients treated with Avastin based on whether they were responsive to therapy. Furthermore, none of these proteins on its

own has been shown to be an effective biomarker for cancer diagnosis or for treatment response. Therefore, this study also reaffirmed past observations that large panels of proteins can serve as highly sensitive and specific biomarker signatures of disease, even when each component protein is a poor disease-marker on its own.

The study also showed that the predictive power of patient classification by hierarchical clustering depended on the number of differentially expressed proteins analyzed. Tests that included those proteins that were statistically significantly differentially expressed ($p < 0.05$) had greater predictive power compared with tests that additionally contained large numbers of non-discriminatory proteins or compared with tests that contained too few discriminatory proteins. The implication for future biomarker signature discovery from large numbers of proteins is that variously sized subsets of differentially expressed proteins should be evaluated to find the optimally-sized set for maximal predictive power.

In this study, the accuracy of test sample classification was also dependent on the fraction of members within the test sample's cluster that belonged to the same group (experimental vs. control). Therefore, prediction accuracy improved when evaluating only those test samples in highly biased clusters, and approached 100 % within completely homogeneous clusters. Of course, the fraction of diagnosable patients decreased as the tolerance for cluster heterogeneity was reduced. In light of this, an optimal tolerance was chosen that maximized diagnostic accuracy while minimizing the fraction of patients left out of the diagnostic evaluation. In this study, we evaluated only three tolerance settings, corresponding to exclusion of test samples in clusters that were: i. perfectly heterogeneous, ii. < 70 % homogeneous, and iii. < 100 % heterogeneous.

However, the study could potentially be reanalyzed with a larger set of tolerances to find an even better optimum. Alternatively, all patients could have been included in the diagnostic evaluation, but with the appreciation that the diagnosis of patients in certain clusters would be more accurate than in others. In theory, an accuracy score or confidence level could be calculated for grouping within any cluster. Subsequently, only those patients whose diagnoses have a predicted accuracy greater than, say, 90 % would be triaged for therapy, whereas all others would have to undergo further tests to ascertain their diagnosis. Based on our results, the diagnostic accuracy would be expected to increase with the homogeneity of a test sample's cluster, with even higher accuracies likely attainable in homogeneous clusters of larger size.

Though it might have been anticipated that plasma protein detection of brain tumors would be difficult due to the blood-brain barrier, in fact, we were able to detect differential expression of a number of factors. Many of these have been associated with systemic cancers or have been previously shown to be differentially expressed in culture media from GBM cell lines and primary cells, in the CSF fluid of GBM patients, or even in patient sera. For example, VEGF, a powerful mediator of endothelial cell proliferation and angiogenesis generally, which was found to be upregulated in GBM patients in this study, has also been shown previously to be highly secreted from GBM cell lines and primary tumors and to be expressed in the CSF fluid of glioblastoma patients[34]. VEGF is typically associated with advanced tumor stage and poor prognosis in a variety of cancers[34]. While no difference in serum expression of VEGF in the context of GBM was found by some[35], our results corroborate reports that have shown upregulated serum expression of VEGF[36]. VEGF is known to promote microvascular permeability[34], which

likely plays a role in the enhanced BBB leakiness at sites of characteristically highly neovascularized GBM tumors, thereby permitting its detection (as well as detection of a whole host of other tumor-associated proteins) in the plasma.

PDGF, which also has an important role in glioblastoma angiogenesis – particularly, in peri-endothelial cell recruitment[37] – was found to be upregulated in Avastin-treated GBM patients with growing tumors in this study. This finding is supported by past studies that have demonstrated that PDGF and its receptor are co-overexpressed in glioblastoma-derived cell lines as well as in primary GBM tumors, promoting neovascularization and tumor progression by an autocrine mechanism[38,39].

The fact that HGF levels were highly overexpressed in the sera of Avastin-treated GBM patients exhibiting tumor growth as compared to those with stable tumors confirms previous reports demonstrating that higher tumor content and CSF levels of HGF are correlated with increased tumor malignancy and poorer prognosis[40]. HGF has also been implicated in synergizing with VEGF to promote glioma angiogenesis and increased microvessel density, particularly by inducing endothelial cell proliferation[41,42]. It is also known that c-Met receptor activation by HGF enhances several oncogenic mechanisms, including cell cycle progression, proliferation, survival, migration, and invasion, and that GBM progression can be mediated by an HGF/c-Met autocrine loop[41]. Since tumors require extensive neovascularization for sustained growth, and considering the instrumental role HGF plays in GBM progression, its heightened presence in the plasma of patients with tumor growth seems sensible.

Serum IGFBP2, a binding protein that regulates the bioavailability and bioactivity of IGFs, was also found to be upregulated in this study, corroborating past reports of

elevated serum and CSF levels of IGFBP2 in patients with GBM and higher grade gliomas generally[43,44]. IGFBP2 has previously been shown to be involved in tumor growth regulation both in vitro and in vivo, and to promote glioma cell migration and invasion[45,46]. Its increased expression has therefore also been associated with increased glioma malignancy and poorer patient prognosis[43].

The ability to detect these proteins in the blood is perhaps less surprising when considering the leaky nature of newly-forming blood vessels in and around a glioblastoma tumor[20], as well as the inflammation-associated[47,48] increase in BBB permeability in the tumor's vicinity. Furthermore, not all the differentially expressed proteins detected are products of tumor cells. Many of these proteins, and particularly the cytokines, are likely secreted from inflammatory and immune cells located either in proximity to the tumor or much farther away, representing a systemic immune or inflammatory anti-tumor response. For example, GM-CSF, IP-10/CXCL-10, and IL13 were all found to be highly expressed in GBM patient plasma as compared to healthy controls. In addition, IL12, MIP1α, and TGFβ1 were all found to be highly differentially expressed in Avastin-treated GBM patients with growing tumors as compared to those with stable tumors.

Serum GM-CSF expression has previously been shown to be increased in GBM patients[36]. This is not surprising considering its important, yet conflicting, roles in promoting tumor proliferation, migration, and angiogenesis on the one hand[36,49], while on the other hand stimulating myeloproliferation in order to mount an immune/ inflammatory attack against growing tumors[48,49]. Likewise, MIP1α and its receptors have been shown to be overexpressed in GBM cells *in vitro*, and likely serve to attract

appropriate subsets of inflammatory and immune effector cells – including lymphocytes and macrophages – to the sites of tissue damage for repair[50]. However, this antitumor activity may be outweighed by an autocrine loop that promotes proliferation of the tumor cells[50]. Differential upregulation of TGFβ1 in patients with growing tumors is consistent with studies showing that tumors, such as glioblastoma, can lose their cytostatic responsiveness to this cytokine, and can instead respond to it by producing PDGF, the tumor growth promoter mentioned previously. Alternatively, tumors can overproduce and utilize TGFβ1 to suppress an antitumor host immune response and evade immune surveillance[51].

The high expression of IP-10/CXCL-10 seen in GBM patients in this study could also reflect the immune system's attempt to inhibit further tumor growth. This cytokine is secreted by monocytes, endothelial cells, and fibroblasts as a chemoattractant for recruitment of monocyte-lineage cells, T cells, and NK cells that can participate in an anti-tumor response[52]. In addition, it has previously been implicated in inhibition of angiogenesis[52], which is vital for tumor growth. Because its upregulation is induced by IFNγ, it is believed to contribute to the IFNγ-dependent anti-tumor effects of IL12[53]. This is also consistent with the upregulation of IL12 observed in this study in Avastin-treated GBM patients with tumor growth as compared to those with stable tumors. Interestingly, it also has conflicting tumor-promoting and proliferative effects on non-transformed astrocytes and cultured glioma cells, and its presence has been correlated with increased malignancy grade[54]. However, its role as a discriminatory marker in this study may be confounded by the fact that our experimental population was older than the control population, and IP-10 levels naturally increase with age, doubling between ages 40 and

70 – 80[55]. Of all the analytes studied, IL13, a cytokine known to have both pro- and anti-tumor effects, showed the highest GBM patient plasma overexpression. This may be attributable to IL13 insensitivity in GBM patients as a result of GBM tumor overexpression of the "decoy" inhibitory receptor IL13Rα2[56], which may be leading to a compensatory increase in IL13 production.

Surprisingly, the levels of both CRP and MMP9 were actually decreased in GBM patient plasma as compared with healthy controls, and VEGFR2 levels were downregulated in Avastin-treated GBM patients with growing tumors as compared to those with stable tumors. Because of MMP9's documented involvement in promoting tumor invasion, as well as its anti-apoptotic and pro-angiogenic effects[57,58], its decreased plasma level in GBM patients in this study was unanticipated. Furthermore, the decrease in VEGFR2, a VEGF receptor, is unexpected since one-third of primary glioblastomas harbor amplifications in 3 receptor tyrosine kinase genes that are juxtaposed on chromosome 4: KIT, PDGFRA, and VEGFR2[59]. Furthermore, past studies have shown that VEGFR2 (and VEGFR1) is highly expressed in primary GBM tumors[60]. However, VEGFR2 downregulation could be explained by the fact that these receptors are internalized by the cell when bound by ligand. Since VEGF levels are high, a significant amount of receptor internalization could be taking place.

3.5 Future Outlook

The fact that the plasma samples used in this study could be interrogated by multiplexed antibody arrays within ELISA-like wells allowed relatively small sample volumes (< 50 μL) to be used. This suggests that these assays can in the future be

performed using blood from a fingerprick rather than the much larger quantities (milliliters) typically harvested by phlebotomy. In addition, the DNA-directed assembly of antibodies makes this platform amenable for use within microfluidics platforms, since DNA arrays can withstand the bonding temperatures required for platform assembly whereas directly-spotted antibody arrays cannot[16,33]. Therefore, a promising next step would be to integrate these arrays and antibody panels within a microfluidics-based blood separation diagnostic device. Because on-chip blood separation obviates the need for centrifugation and other blood processing steps, and due to the faster kinetics of ligand capture under conditions of fluid flow, all the assay steps within the microfluidic environment can be performed in under an hour. Consequently, a point-of-care diagnostic chip that probes for the most highly discriminatory proteins described herein for classifying patients into GBM or healthy subgroups (or for gauging treatment response) would allow patients to be diagnosed or monitored using a simple fingerprick blood test within a short time after walking into a doctor's office.

Future studies could also enlarge the microarray panel to hundreds of plasma proteins and evaluate even larger patient populations with varying grades of glioma. This could allow for higher resolution stratification of patients into diagnostic and treatment groups based on their molecular phenotypes, which could be more informative than histological grading alone. Additional studies could also assess the ability of these types of assays to classify patients as responders or non-responders shortly after initiation of treatment. Currently, using contrast-enhanced MRI imaging, it could take at least a week or more to discern whether a tumor is still growing or stable. However, it is likely that molecular changes within the tumor are occurring long before these changes manifest as

visible tumor growth and progression. Therefore, a blood test that could evaluate treatment response within hours of administration of a chemotherapeutic would allow doctors to arrive at the most effective treatment in the shortest possible time. The resulting benefits to the patient's health as well as the cost-savings could be significant.

3.6 References

1. McLendon, R.; et al. Comprehensive genomic characterization defines human glioblastoma genes and core pathways. *Nature*, **2008**, 455, 1061-1068.

2. Fauci, A. *Harrison's Principles of Internal Medicine*. New York: McGraw-Hill, 2005.

3. Deimling, A.; et al. Subsets of glioblastoma multiforme defined by molecular genetic analysis. *Brain Pathol.*, **1993**, 3, 19-26.

4. Jiang, R.; et al. Pathway alterations during glioma progression revealed by reverse phase protein lysate arrays. *Proteomics*, **2006**, 6, 2964-2971.

5. Freije, W.; et al. Gene expression profiling of gliomas strongly predicts survival. *Cancer Res.*, **2004**, 64, 6503.

6. Sreekanthreddy, P.; et al. Identification of potential serum biomarkers of glioblastoma: serum osteopontin levels correlate with poor prognosis. *Cancer Epidem. Biomar.*, **2010**, 19, 1409.

7. Huang, R. P.; Huang, R.; Fan, Y.; Lin, Y. Simultaneous detection of multiple cytokines from conditioned media and patient's sera by an antibody-based protein array system. *Anal. Biochem.*, **2001**, 294, 55-62.

8. Iwadate, Y.; et al. Molecular classification and survival prediction in human gliomas based on proteome analysis. *Cancer Res.*, **2004**, 64, 2496.

9. Schwartz, S.; Weil, R.; Johnson, M.; Toms, S.; Caprioli, R. Protein profiling in brain tumors using mass spectrometry. *Clin. Cancer Res.*, **2004**, 10, 981.

10. Mischel, P.; Cloughesy, T.; Nelson, S. DNA-microarray analysis of brain cancer: molecular classification for therapy. *Nat. Rev. Neurosci.*, **2004**, 5, 782-792.

11. Kingsmore, S. Multiplexed protein measurement: technologies and applications of protein and antibody arrays. *Nat. Rev. Drug Discovery*, **2006**, 5, 310-321.

12. Lv, L.; Liu, B. High-throughput antibody microarrays for quantitative proteomic analysis. *Expert Rev. Proteomics*, **2007**, 4, 505-513.

13. Varnum, S.; Woodbury, R.; Zangar, R. A protein microarray ELISA for screening biological fluids. *Methods in Molecular Biology -Clifton then Totowa*, **2004**, 264, 161-172.

14. Sack, R.; et al. Membrane array characterization of 80 chemokines, cytokines, and growth factors in open-and closed-eye tears: angiogenin and other defense system constituents. *Invest. Ophthalmol. Vis. Sci.*, **2005**, 46, 1228.

15. Kastenbauer, S.; Angele, B.; Sporer, B.; Pfister, H.; Koedel, U. Patterns of protein expression in infectious meningitis: a cerebrospinal fluid protein array analysis. *J. Neuroimmunol.*, **2005**, 164, 134-139.

16. Fan, R.; et al. Integrated barcode chips for rapid, multiplexed analysis of proteins in microliter quantities of blood. *Nat. Biotechnol.*, **2008**, 26, 1373-1378.

17. Hanash, S.; Pitteri, S.; Faca, V. Mining the plasma proteome for cancer biomarkers. *Nature*, **2008**, 452, 571-579.

18. Rubin, L.; Staddon, J. The cell biology of the blood-brain barrier. *Annu. Rev. Neurosci.*, **1999**, 22, 11-28.

19. Abbott, N. Inflammatory mediators and modulation of blood–brain barrier permeability. *Cell. Mol. Neurobiol.*, **2000**, 20, 131-147.

20. Kumar, V.; Abbas, A.; Fausto, N. *Robbins and Cotran Pathologic Basis of Disease*. 7th ed. Philadelphia: Saunders, 2005.

21. Leon, S.; Folkerth, R; Black, P. Microvessel density is a prognostic indicator for patients with astroglial brain tumors. *Cancer*, **1996**, 77, 362-372.

22. Kargiotis, O.; Rao, J.; Kyritsis, A. Mechanisms of angiogenesis in gliomas. *J. Neuro-Oncol.*, **2006**, 78, 281-293.

23. Schneider, S.; et al. Glioblastoma cells release factors that disrupt blood-brain barrier features. *Acta Neuropathol.*, **2004**, 107, 272-276.

24. Ludwig, J.; Weinstein, J. Biomarkers in cancer staging, prognosis and treatment selection. *Nat. Rev. Cancer*, **2005**, 5, 845-856.

25. Jiang, R.; Li, J.; Fuller, G.; Zhang, W. "Proteomic Profiling of Human Brain Tumors." *CNS Cancer*. Ed. van Meir, E. G. London: Harwood Academic Publishers, 2009. pp. 553-575.

26. Ray, S.; et al. Classification and prediction of clinical Alzheimer's diagnosis based on plasma signaling proteins. *Nat. Med.*, **2007**, 13, 1359-1362.

27. Wulfkuhle, J.; Liotta, L; Petricoin, E. Proteomic applications for the early detection of cancer. *Nat. Rev. Cancer*, **2003**, 3, 267-275.

28. Sanchez-Carbayo, M.; Socci, N.; Lozano, J.; Haab, B.; Cordon-Cardo, C. Profiling bladder cancer using targeted antibody arrays. *Am. J. Pathol.*, **2006**, 168, 93.

29. Orchekowski, R.; et al. Antibody microarray profiling reveals individual and combined serum proteins associated with pancreatic cancer. *Cancer Res.*, **2005**, 65, 11193.

30. Miller, J.; et al. Antibody microarray profiling of human prostate cancer sera: antibody screening and identification of potential biomarkers. *Proteomics*, **2003**, 3, 56-63.

31. Ellmark, P.; et al. Identification of protein expression signatures associated with Helicobacter pylori infection and gastric adenocarcinoma using recombinant antibody microarrays. *Mol. Cell. Proteomics*, **2006**, 5, 1638.

32. Wacker, R.; Schröder, H.; Niemeyer, C. Performance of antibody microarrays fabricated by either DNA-directed immobilization, direct spotting, or streptavidin-biotin attachment: a comparative study. *Anal. Biochem.*, **2004**, 330, 281-287.

33. Bailey, R. C.; Kwong, G. A.; Radu, C. G.; Witte, O. N.; Heath, J. R. DNA-encoded antibody libraries: A unified platform for multiplexed cell sorting and detection of genes and proteins. *J. Am. Chem. Soc.*, **2007**, 129, 1959-1967.

34. Hicklin, D.; Ellis, L. Role of the vascular endothelial growth factor pathway in tumor growth and angiogenesis. *J. Clin. Oncol.*, **2005**, 23, 1011.

35. Takano, S.; et al. Concentration of vascular endothelial growth factor in the serum and tumor tissue of brain tumor patients. *Cancer Res.*, **1996**, 56, 2185.

36. Rafat, N.; Beck, G.; Schulte, J.; Tuettenberg, J.; Vajkoczy, P. Circulating endothelial progenitor cells in malignant gliomas. *J. Neurosurg. Pediatrics*, **2010**, 112.

37. Guo, P.; et al. Platelet-derived growth factor-B enhances glioma angiogenesis by stimulating vascular endothelial growth factor expression in tumor endothelia and by promoting pericyte recruitment. *Am. J. Pathol.*, **2003**, 162, 1083.

38. Hermansson, M.; et al. Endothelial cell hyperplasia in human glioblastoma: coexpression of mRNA for platelet-derived growth factor (PDGF) B chain and PDGF receptor suggests autocrine growth stimulation. *P. Natl. Acad. Sci. USA*, **1988**, 85, 7748.

39. Guha, A.; Dashner, K.; McBlack, P.; Wagner, J.; Stiles, C. Expression of PDGF and PDGF receptors in human astrocytoma operation specimens supports the existence of an autocrine loop. *Int. J. Cancer*, **1995**, 60, 168-173.

40. Garcia-Navarrete, R.; Garcia, E.; Arrieta, O.; Sotelo, J. Hepatocyte growth factor in cerebrospinal fluid is associated with mortality and recurrence of glioblastoma, and could be of prognostic value. *J. Neuro-Oncol.*, **2010**, 97, 347-351.

41. Abounader, R.; Laterra, J. “HGF/c-Met Signaling and Targeted Therapeutics in Brain Tumors.” *CNS Cancer*. Ed. van Meir, E. G. London: Harwood Academic Publishers, 2009. pp. 933-952.

42. Schmidt, N.; et al. Levels of vascular endothelial growth factor, hepatocyte growth factor/scatter factor and basic fibroblast growth factor in human gliomas and their relation to angiogenesis. *Int. J. Cancer*, **1999**, 84, 10-18.

43. Lin, Y.; et al. Plasma IGFBP-2 levels predict clinical outcomes of patients with high-grade gliomas. *Neuro Oncol.*, **2009**, 11, 468.

44. Hoeflich, A.; et al. Insulin-like growth factor-binding protein 2 in tumorigenesis: protector or promoter? *Cancer Res.*, **2001**, 61, 8601.

45. Dunlap, S.; et al. Insulin-like growth factor binding protein 2 promotes glioma development and progression. *P. Natl. Acad. Sci. USA*, **2007**, 104, 11736.

46. Wang, H.; et al. Insulin-like growth factor binding protein 2 enhances glioblastoma invasion by activating invasion-enhancing genes. *Cancer Res.*, **2003**, 63, 4315.

47. Fossati, G.; et al. Neutrophil infiltration into human gliomas. *Acta Neuropathol.*, **1999**, 98, 349-354.

48. Frei, K.; et al. Granulocyte-macrophage colony-stimulating factor (GM-CSF) production by glioblastoma cells. Despite the presence of inducing signals GM-CSF is not expressed in vivo. *J. Immunol.*, **1992**, 148, 3140.

49. Mueller, M.; et al. Autocrine growth regulation by granulocyte colony-stimulating factor and granulocyte macrophage colony-stimulating factor in human gliomas with tumor progression. *Am. J. Pathol.*, **1999**, 155, 1557.

50. Kouno, J.; et al. Up-regulation of CC chemokine, CCL3L1, and receptors, CCR3, CCR5 in human glioblastoma that promotes cell growth. *J. Neuro-Oncol.*, **2004**, 70, 301-307.

51. Massagué, J.; Gomis, R. The logic of TGF [beta] signaling. *FEBS Lett.*, **2006**, 580, 2811-2820.

52. Enderlin, M.; et al. TNF- and the IFN- -inducible protein 10 (IP-10/CXCL-10) delivered by parvoviral vectors act in synergy to induce antitumor effects in mouse glioblastoma. *Cancer Gene Ther.*, **2008**, 16, 149-160.

53. Phelps, C.; Korneva, E. *Cytokines and the Brain*. Amsterdam: Elsevier Science Ltd, 2008.

54. Maru, S.; et al. Chemokine production and chemokine receptor expression by human glioma cells: role of CXCL10 in tumour cell proliferation. *J. Neuroimmunol.*, **2008**, 199, 35-45.

55. Shurin, G.; et al. Dynamic alteration of soluble serum biomarkers in healthy aging. *Cytokine*, **2007**, 39, 123-129.

56. Liu, H.; et al. Interleukin-13 sensitivity and receptor phenotypes of human glial cell lines: non-neoplastic glia and low-grade astrocytoma differ from malignant glioma. *Cancer Immunol. Immun.*, **2000**, 49, 319-324.

57. Yong, V.; Power, C.; Forsyth, P.; Edwards, D. Metalloproteinases in biology and pathology of the nervous system. *Nat. Rev. Neurosci.*, **2001**, 2, 502-511.

58. Egeblad, M.; Werb, Z. New functions for the matrix metalloproteinases in cancer progression. *Nat. Rev. Cancer*, **2002**, 2, 163-176.

59. Puputti, M.; et al. Amplification of KIT, PDGFRA, VEGFR2, and EGFR in gliomas. *Mol. Cancer Res.*, **2006**, 4, 927.

60. Huang, H.; Held-Feindt, J.; Buhl, R.; Mehdorn, H.; Mentlein, R. Expression of VEGF and its receptors in different brain tumors. *Neurol. Res.*, **2005**, 27, 371-377.

3.7 Appendix A: DNA-Encoded Antibody Libraries (DEAL) Technique

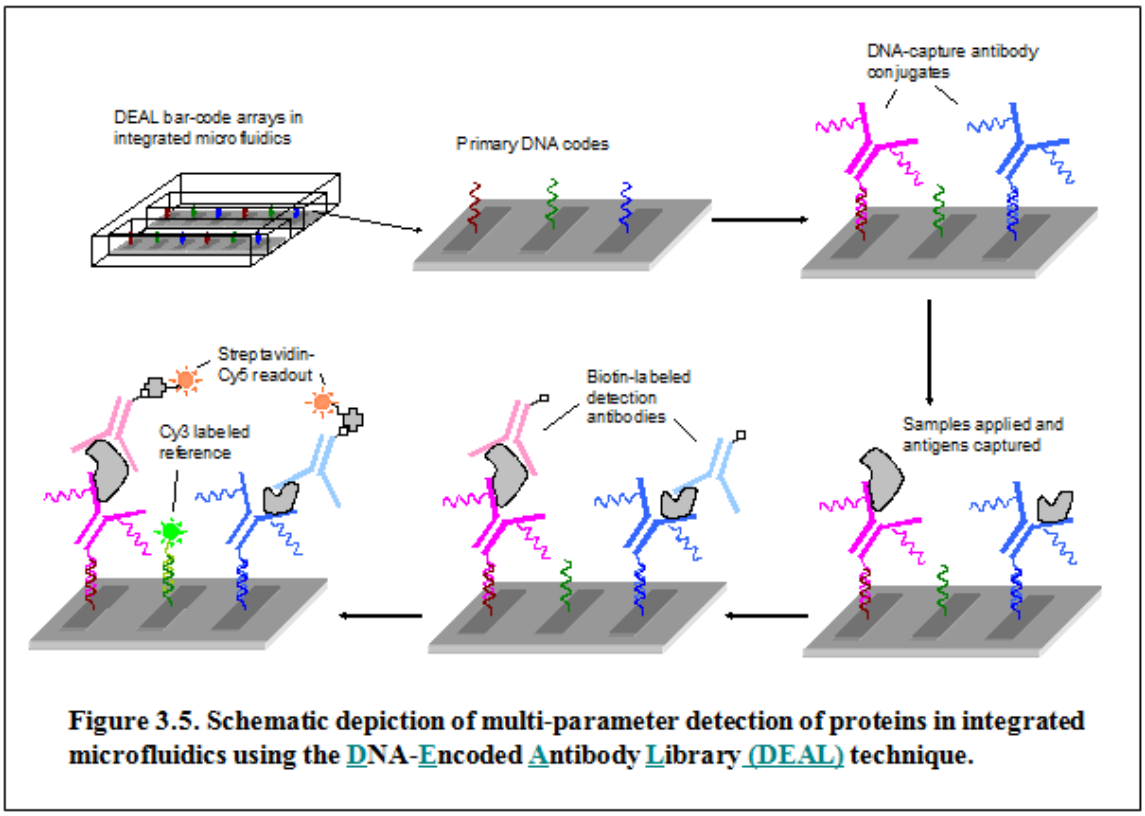

Figure 3.5. Schematic depiction of multi-parameter detection of proteins in integrated microfluidics using the DNA-Encoded Antibody Library (DEAL) technique.

The advantages of DEAL are multifold. First, the fact that DNA hybridization is utilized as an assembly strategy allows for multiple proteins to be detected within the same microenvironment, since the various 1^{o} CA antibodies for the various proteins to be detected can be each labeled with a different ssDNA oligomer (**Figure 3.5**). Second, antibodies are not particularly stable, and this makes surfaces onto which antibodies are attached unstable towards drying out, heating, etc. This means that the antibody must be attached to the surface immediately prior to use. Using DNA hybridization as an assembly strategy means that the surface can be prepared ahead of time, dried out,

heated, shipped around, etc. The instability of antibodies also makes protein assays difficult to execute within microfluidics environments, since the antibodies don't survive the microfluidics fabrication. This is, again, circumvented with the DEAL approach.

3.8 Appendix B: Patient Characteristic Tables

Table 3.1. GBM patient vs. healthy control population characteristics.

		GBM		Healthy	
		Patients	Samples	Patients	Samples
Total		46	72	47	47
Age	Median	56	56	39	39
	Mean	56	56	41	41
	Range	30-82	30-82	18-72	18-72
Gender	Male	28	48	22	22
	Female	18	24	18	18
	N/A			7	7
Treatment	No Avastin	11	14	47	47
	Avastin	24	36	0	0
	Avastin 184	2	6	0	0
	Pre-Avastin	7	14	0	0
	N/A	2	2	0	0
Recurrence	New	5	9	N/A	N/A
	1st	14	24	N/A	N/A
	2nd	5	6	N/A	N/A
	3rd	2	7	N/A	N/A
	4th	2	2	N/A	N/A
Blood Draws	1	27		47	
	2	12		0	
	3	4		0	
	4	1		0	
	5	1		0	

Table 3.2. Avastin-treated GBM patients: characteristics of patient population with and without tumor recurrence.

		Tumor Growth		No Tumor Growth	
		Patients	Samples	Patients	Samples
Total		25	52	21	51
Age	Median	56		57	
	Mean	55		54	
	Range	30-82		30-71	
Gender	Male	16	30	10	33
	Female	9	22	11	17
Treatment	Avastin	20	44	19	49
	Avastin 184	5	8	2	2
T2 Levin Score	-2	16	30	0	0
	-1	8	16	0	0
	0	3	4	21	51
	1	1	1	0	0
	2	1	1	0	0
T1C Levin Score	-2	11	22	0	0
	-1	12	16	0	0
	0	6	6	21	51
	1	5	5	0	0
	2	1	3	0	0
Recurrence	New	3	5	4	13
	1st	9	15	7	11
	2nd	3	6	2	2
	3rd	3	5	1	1
	4th	1	1	2	3
	6th	1	1	0	0
	N/A	12	18	5	5
Blood Draws	1	13		9	
	2	3		5	
	3	6		2	
	4	1		3	
	5	1		1	
	6	1		0	
	7	0		0	
	8	0		0	
	9	0		1	

3.9 Appendix C: Serum Protein Biomarker Panels and Oligonucleotide Labels

The protein panels used in the cancer-patient serum experiment (panel 1) and finger-prick blood test (panel 2), the corresponding DNA codes, and their sequences are summarized in **Table 3.3** and **Table 3.4**. These DNA oligomers were synthesized by Integrated DNA Technologies (IDT), and purified by high pressure liquid chromatography (HPLC). The quality was confirmed by mass spectrometry. The antibody vendors and catalogue numbers are listed in **Table 3.5**.

Table 3.3. List of proteins and corresponding DNA codes

DNA-code	Human Plasma Protein	Abbreviation
Panel (1)		
A/A'	Interleukin-2	IL-2
B/B'	Monocyte Chemotactic Protein 1	MCP1
C/C'	Interleukin-6	IL-6
D/D'	Granulocyte-Colony Stimulating Factor	G-CSF
E/E'	Macrophage Migration Inhibitory Factor	MIF
F/F'	Epidermal Growth Factor	EGF
G/G'	Vascular Endothelial Growth Factor	VEGF
H/H'	Platelet Derived Growth Factor	PDGF
I/I'	Transcription Growth Factor alpha	TGFα
J/J'	Interleukin-8	IL-8
K/K'	Matrix Metalloproteinase 3	MMP3
L/L'	Hepatocyte Growth Factor	HGF
M/M'	Reference (Cy3)	M'-Cy3
N/N'	Interferon-Inducible Protein 10	IP10/CXCL10
O/O'	Stromal Cell-Derived Factor 1	SDF1
P/P'	Insulin-like Growth Factor Binding Protein 2	IGFBP2
S/S'	Insulin-like Growth Factor Binding Protein 5	IGFBP5
U/U'	Macrophage Inflammatory Protein 1 alpha	MIP1α
Z/Z'	Transcription Growth Factor Beta 1	TGFβ1
AA/AA'	Chitinase 3-like 1	Ch3L1
BB/BB'	Vascular Endothelial Growth Factor Receptor 3	VEGFR3
CC/CC'	Tumor Necrosis Factor alpha	TNFα
HH/HH'	Granulocyte-macrophage colony stimulating factor	C3
II/II'	Matrix Metalloproteinase 2	MMP2
JJ/JJ'	Interleukin-10	IL-10
KK/KK'	Interleukin-1 beta	IL-1β
MM/MM'	Interleukin-12	IL-12
NN/NN'	Matrix Metalloproteinase 9	MMP9
PP/PP'	Transforming Growth Factor Beta 2	TGFβ2
QQ/QQ'	Granulocyte Macrophage Colony-Stimulating Factor	GM-CSF
RR/RR'	C-Reactive Protein	CRP
SS/SS'	Vascular Endothelial Growth Factor Receptor 2	VEGFR2
TT/TT'	Interleukin-13	IL-13
UU/UU'	Interleukin-23	IL-23
VV/VV'	Serpin E1	Serpin E1
WW/WW'	Fibrinogen	Fibrinogen

Table 3.4. List of DNA sequences used for spatial encoding of antibodies

Sequence Name	Sequence	Tm (50mM NaCl) ^{O}C
A	5'- AAA AAA AAA AAA AAT CCT GGA GCT AAG TCC GTA-3'	57.9
A'	5' NH3- AAA AAA AAA ATA CGG ACT TAG CTC CAG GAT-3'	57.2
B	5'-AAA AAA AAA AAA AGC CTC ATT GAA TCA TGC CTA -3'	57.4
B'	5' NH3AAA AAA AAA ATA GGC ATG ATT CAA TGA GGC -3'	55.9
C	5'- AAA AAA AAA AAA AGC ACT CGT CTA CTA TCG CTA -3'	57.6
C'	5' NH3-AAA AAA AAA ATA GCG ATA GTA GAC GAG TGC -3'	56.2
D	5'-AAA AAA AAA AAA AAT GGT CGA GAT GTC AGA GTA -3'	56.5
D'	5' NH3-AAA AAA AAA ATA CTC TGA CAT CTC GAC CAT -3'	55.7
E	5'-AAA AAA AAA AAA AAT GTG AAG TGG CAG TAT CTA -3'	55.7
E'	5' NH3-AAA AAA AAA ATA GAT ACT GCC ACT TCA CAT -3'	54.7
F	5'-AAA AAA AAA AAA AAT CAG GTA AGG TTC ACG GTA -3'	56.9
F'	5' NH3-AAA AAA AAA ATA CCG TGA ACC TTA CCT GAT -3'	56.1
G	5'-AAA AAA AAA AGA GTA GCC TTC CCG AGC ATT-3'	59.3
G'	5' NH3-AAA AAA AAA AAA TGC TCG GGA AGG CTA CTC-3'	58.6
H	5'-AAA AAA AAA AAT TGA CCA AAC TGC GGT GCG-3'	59.9
H'	5' NH3-AAA AAA AAA ACG CAC CGC AGT TTG GTC AAT-3'	60.8
I	5'-AAA AAA AAA ATG CCC TAT TGT TGC GTC GGA-3'	60.1
I'	5' NH3-AAA AAA AAA ATC CGA CGC AAC AAT AGG GCA-3'	60.1
J	5'-AAA AAA AAA ATC TTC TAG TTG TCG AGC AGG-3'	56.5
J'	5' NH3-AAA AAA AAA ACC TGC TCG ACA ACT AGA AGA-3'	57.5
K	5'-AAA AAA AAA ATA ATC TAA TTC TGG TCG CGG-3'	55.4
K'	5' NH3-AAA AAA AAA ACC GCG ACC AGA ATT AGA TTA-3'	56.3
L	5'-AAA AAA AAA AGT GAT TAA GTC TGC TTC GGC-3'	57.2
L'	5' NH3-AAA AAA AAA AGC CGA AGC AGA CTT AAT CAC-3'	57.2
M	5'-Cy3-AAA AAA AAA AGT CGA GGA TTC TGA ACC TGT-3'	57.6
M'	5' NH3-AAA AAA AAA AAC AGG TTC AGA ATC CTC GAC-3'	56.9
AA	5'-AAAAAAAAAATAAGCCAGTGTGTCGTGTCT-3'	58
AA'	5'NH3-AAAAAAAAAAAGACACGACACACTGGCTTA-3'	58.1
BB	5'-AAAAAAAAAAAGTCTGATCCCATCGCGTAT-3'	57.8
BB'	5'NH3-AAAAAAAAAAATACGCGATGGGATCAGACT-3'	57.8

CC	5’-AAAAAAAAAAGAGGTCAGTTCACGAAGCTC-3’	58.2
CC'	5’NH3-AAAAAAAAAAGAGCTTCGTGAACTGACCTC-3’	58.2
HH	5’-AAAAAAAAAAGCACTAACTGGTCTGGGTCA-3’	59.2
HH'	5’NH3-AAAAAAAAAATGACCCAGACCAGTTAGTGC-3’	58.4
II	5'-AAA AAA AAA AGT CAG GTG TTC GCG CTC ATT -3'	60.1
II'	5'NH3-AAA AAA AAA AAA TGA GCG CGA ACA CCT GAC -3'	59.4
JJ	5'-AAA AAA AAA AGA TCG TAT GGT CCG CTC TCA -3'	58.8
JJ'	5'NH3-AAA AAA AAA ATG AGA GCG GAC CAT ACG ATC -3'	58
KK	5'-AAA AAA AAA AAC AGG TCA TCG AAC TCT CAG -3'	56.7
KK'	5'NH3-AAA AAA AAA ACT GAG AGT TCG ATG ACC TGT -3'	57.5
MM	5'-AAA AAA AAA AGG CGG CTA TTG ACG AAC TCT -3'	59.5
MM'	5'NH3-AAA AAA AAA AAG AGT TCG TCA ATA GCC GCC -3'	58.8
NN	5'-AAA AAA AAA AGC AGG GAA TTG CCG ACC ATA -3'	59.9
NN'	5'NH3-AAA AAA AAA ATA TGG TCG GCA ATT CCC TGC -3'	59.1
PP	5'-AAA AAA AAA ACG CGG CGT GTC TCA GAA TAT -3'	59.8
PP'	5'NH3-AAA AAA AAA AAT ATT CTG AGA CAC GCC GCG -3'	58.9
QQ	5'-AAA AAA AAA AAT CCG GTC TCA TCG CTG AAT -3'	58.2
QQ'	5'NH3-AAA AAA AAA AAT TCA GCG ATG AGA CCG GAT -3'	58.2
RR	5'-AAA AAA AAA AAA TGC TCA CAT CGC AGG TAC -3'	57.6
RR'	5'NH3-AAA AAA AAA AGT ACC TGC GAT GTG AGC ATT -3'	58.3
SS	5'-AAA AAA AAA AAC GCT AAT GAC GGC AGT GCA -3'	60.4
SS'	5'NH3-AAA AAA AAA ATG CAC TGC CGT CAT TAG CGT -3'	60.3
TT	5'-AAA AAA AAA AAT GTG TCC GAA CGT CGA GCT -3'	59.8
TT'	5'NH3-AAA AAA AAA AAG CTC GAC GTT CGG ACA CAT -3'	59.8
UU	5'-AAA AAA AAA AGC CGT CGG TTC AGG TCA TAT -3'	59.4
UU'	5'NH3-AAA AAA AAA AAT ATG ACC TGA ACC GAC GGC -3'	58.7
VV	5'-AAA AAA AAA AGT CGC GGG TTC TGC ACA TAT -3'	59.9
VV'	5' NH3-AAA AAA AAA AAT ATG TGC AGA ACC CGC GAC -3'	59.2

* All amine-terminated strands were linked to antibodies to form DNA-antibody conjugates using SFB/SANH coupling chemistry described by R. Bailey et al.[33] Codes AA-HH were used in the experiment examining fresh whole blood from a healthy volunteer. Codes A-M were used for the molecular analyses of cancer patient serum samples.

Table 3.5. Antibody vendors and catalogue numbers

	Company	Capture Antibody (Catalogue #)	Detection Antibody (Catalogue #)
IL2	BD	555051	555040
MCP1	eBioscience	16-7099-85	13-7096-85
IL6	eBioscience	16-7069-85	13-7068-85
G-CSF	R&D systems	MAB214	BAF214
MIF	R&D systems	MAB289	BAF289
EGF	R&D systems	MAB636	BAF236
VEGF	R&D systems	MAB293	BAF293
PDGF	R&D systems	MAB1739	BAF221
TGFa	R&D systems	AF-239-NA	BAF239
IL8	BD	554718	554716
MMP3	R&D systems	AF513	BAF513
HGF	R&D systems	MAB694	BAF294
IP10	R&D systems	MAB266	BAF266
SDF1	R&D systems	MAB350	BAF310
IGFBP2	R&D systems	MAB6741	BAF674
IGFBP5	R&D systems	MAB8751	BAF875
MIP1a	R&D systems	AF-270-NA	BAF270
TGFb1	BD	559119	559119
Ch3L1	R&D systems	DY2599	DY2599
VEGFR3	R&D systems	MAB349	BAM3492
TNFa	eBioscience	16-7348-85	13-7349-85
C3	abcam	ab17455-100	ab14232-50
MMP2	R&D systems	DY1496	DY1496
IL10	eBioscience	16-7108-85	13-7109-85
IL1b	eBioscience	16-7018-85	13-7016-85
IL12	eBioscience	14-7128-82	13-7129-85
MMP9	R&D systems	MAB9092	BAM909
TGFb2	R&D systems	DY302	DY302
GM-CSF	BD	554502	554505
CRP	R&D systems	MAB17071	BAM17072
VEGF R2	R&D systems	MAB3573	BAF357
IL13	eBioscience	16-7139-81	13-7138-81
IL23	eBioscience	14-7238-85	13-7129-85
Serpin E1	R&D systems	MAB1786	BAF1786
Fibrinogen	abcam	ab10066-250	ab14790-200

3.10 Appendix D: DNA Crosstalk Validation Assay

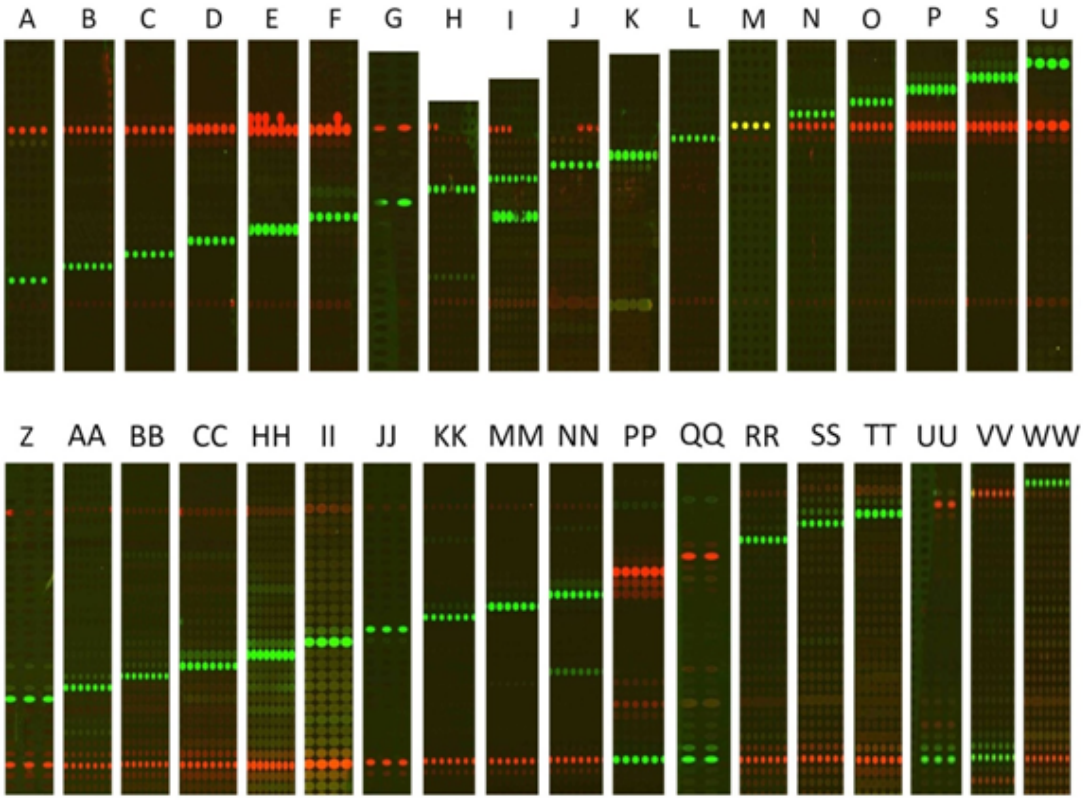

Figure 3.6. Test for DNA cross-hybridization. 36 ssDNA oligonucleotides (dye conjugates) were each tested separately for orthogonality against the full set of 36 surface-bound complementary strands. Red = **M′**-Cy5 reference. Green = Cy3-conjugated oligonucleotide. However, for **PP**, **QQ**, **UU**, and **VV**: Green = **M′**-Cy3 reference, Red = Cy5-conjugated oligonucleotide. Cross-hybridization was far less than the 5% cut-off for all oligonucleotides except for **I**, where the cross-hybridization level with **F** was 8% (and can be distinctly seen in the image).

Chapter 4

High-Density, Multiplexed Patterning of Cells at Single-Cell Resolution for Applications in Tissue Engineering

"To further the construction of complex tissues, or even entire organs, there are still significant technical challenges to overcome. Among them, a very important problem is subtly combining and orchestrating cells, growth factors and scaffolds into an architecture that will allow their unfettered interaction, especially where distinct cell types are required in anatomically exact locations to attain biological function."

-Thomas Boland. Inkjet printing of viable mammalian cells. *Biomaterials,* **2005,** 26, 93-99.

4.1 Introduction

4.1.1 Advances in tissue engineering

Considerable advances in the design of functional replacements for damaged or destroyed tissues and organs over the last decade or so have created an avenue for overcoming both the shortage and immunogenicity of allogeneic transplants. Tissue

engineered substitutes for a number of tissues have already been created, including stomach[1], esophagus[2], spinal cord[3], and several types of commercially available skin. In addition, various types of cartilage, bone, and blood vessel replacements have been successfully implanted into humans[4].

Classical tissue engineering approaches have utilized a top-down approach, in which a solid scaffold mimicking an organ or tissue is first created, followed by seeding of cells on this scaffold[5]. While this method has been useful in a broad range of scenarios, its major limitations are difficulties in mimicking the native microarchitecture (i.e., placing different cell types in precise positions relative to each other) and vascularizing large scaffolds for delivery of oxygen and nutrients to cells[6].

An alternative to this approach, which has been developed in recent years, is a bottom-up approach, in which cells are first patterned in an arrangement that closely emulates the native tissue microarchitecture, and these building blocks are then "stacked" together to create a functional tissue unit[7]. Examples of this include encasing patterned cells in thin layers of thermally- or UV-curable hydrogels, which are sufficiently rigid so as to maintain, intact, the architecture of patterned cells. These cell-laden hydrogels are then stacked on top of each other to create three-dimensional structures[8].

The success of cell culture and growth in these environments lies in the fact that hydrogels can closely mimic the tensile, elastic, and compressive physical forces a cell typically encounters within its native extracellular matrix (ECM) [9]. In addition, hydrogels can be impregnated with ECM proteins that allow cells to attach to the extracellular matrix (be it native or synthetic), and which provide the chemical cues that anchorage-dependent cells require for growth and survival[9-11]. Moreover, soft-lithography

techniques can be used to imprint vascular channels between cell-laden hydrogel layers to provide perfusion at the length-scales of the native microenvironment[12].

An important additional benefit that certain hydrogels can provide is their relative lack of immunogenicity, which could potentially allow allogeneic cells encased within them to be transplanted with minimal risk of detection by the host's immune surveillance[13,14]. Capitalizing on this idea, many groups have sought to minimize or even eliminate the immunogenicity of allogeneic islet transplants by encapsulating donor β cells (insulin-producing islet cells) in hydrogel microcapsules made of non-immunogenic materials, such as alginate or polyethylene glycol (PEG) [15-17]. These hydrogel capsules contain pores that are large enough to allow oxygen and nutrients to be transported freely for metabolic sustenance, but that are too small for entry of antibodies or T cells[14]. In principle, islets from other species (pigs, monkeys) could potentially be encapsulated, without the danger of graft rejection, allowing for an ample supply of islets to be harvested and transplanted[10]. In addition, human and non-human stem- and precursor-cells could be propagated in culture and then encapsulated for transplantation[10,14].

Of course, the potential advantages of encapsulation come with the challenges of ensuring cell survival in microcapsules over extended periods. Many groups have looked at ways of increasing the longevity of cells within these capsules by adding extracellular matrix proteins, tuning their size (smaller capsules have a smaller diffusion barrier) and porosity, and embedding molecules (such as VEGF) that accelerate vascularization of the transplants in rodent models.

However, it is becoming increasingly recognized that these may not be the only factors that are essential to cell survival and function. In most tissues, cells require

chemical cues from particular types of adjacent cells (juxtacrine signaling) and nearby cells (paracrine signaling) in order to survive and properly perform their functional roles. For example, in the central nervous system (CNS), glial cells receive inputs, assimilate information and send instructive chemical signals both to neurons and to other neighboring cells[18,19]. Astrocytes, in particular, have been implicated in dynamic regulation of neuron production, synaptic network formation, and neuron electrical activity[20]. Also, in endocrine glands, proper hormone secretion requires cell-cell communication for regulated and synchronous activity of all cells within the gland[21,22]. The human islet is no exception. Unlike the rodent islet, in which β cells cluster together in the islet center (forming an "insulin core") while glucagon-secreting α cells and the less abundant δ and PP cells are relegated to the periphery, all endocrine cell types in human islets are interspersed together in a manner that is likely nonrandom (Figure 4.1). The multiple islet cell types are free to intermingle in "an arrangement which predisposes human islets for strong paracrine interactions[23]." In order for native microarchitectural arrangements to be reproduced in synthetic constructs created from cultured islet or CNS cells, some method of patterning these various cell types in close proximity to each other, in the correct ratios, and with precise relative positioning is needed.

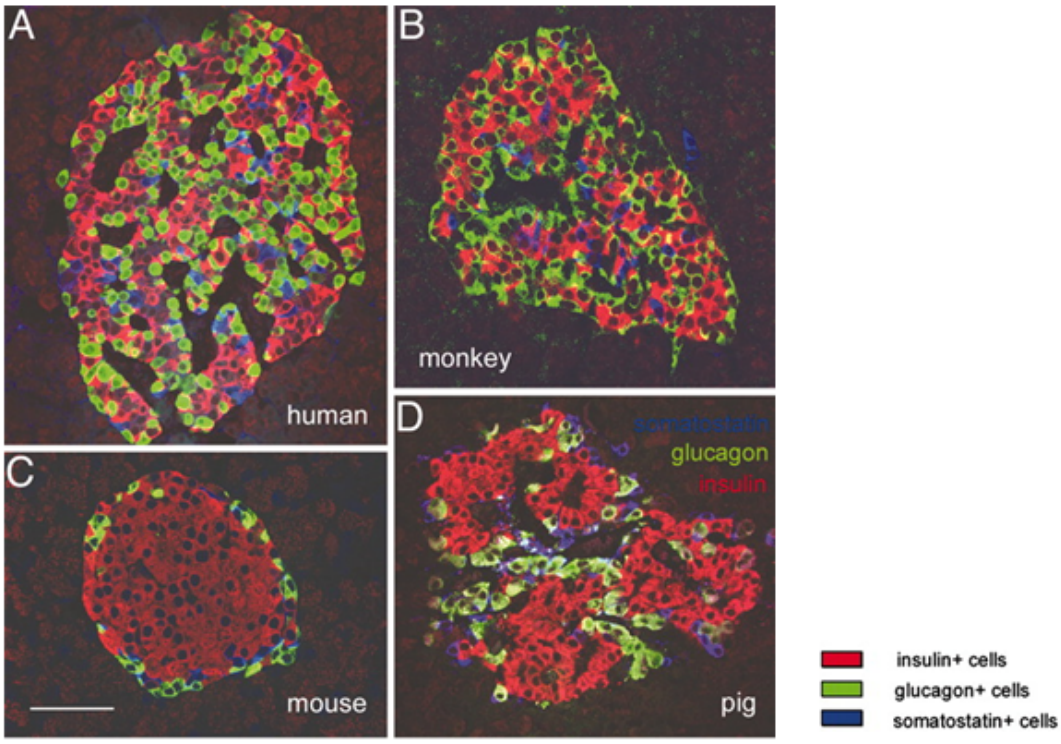

Figure 4.1. Cell arrangements within islets of Langerhans in different species. Note the core-mantle arrangement of α and β cells in mouse and pig islets in contrast to the more dispersed, almost checkerboard-like, clustering of cells in human islets. Red → β cells; Green → α cells; Blue → δ cells.

4.1.2 Challenges and limitations to high-resolution multiplexing

Toward this end, microfabrication techniques borrowed from the semiconductor industry appear to hold the most promise. Microfabrication techniques have paved the way to breakthroughs in our ability to pattern cells at high resolution for applications in biosensing[24,25], drug screening[26,27], neural networks[28], and artificial tissues[29,30]. Existing methods for patterning cells include microcontact printing[31,32], inkjet printing[6,33,34], switchable substrates[35,36], elastomeric stencils[37,38], microwells[29,39], optical tweezers[40,41], electrophoresis[42], and dielectrophoresis[8,43]. A major limitation of most of these platforms,

however, is the multiplexing resolution – the resolution at which different cell types can be patterned. For example, microcontact printing can be used for dense patterning of cell-binding proteins with low-micron to sub-micron feature sizes; however, in order to print distinct features adjacently, multiple inking and alignment steps must be performed. In addition, the loading density of biomolecules patterned by this approach is limited, as the platform is typically suited to printing monolayers. Dielectrophoresis has been successfully used to pattern complex two-dimensional cellular microstructures, including liver lobules[8,43], but this approach does not appear as yet to be amenable to a high degree of multiplexing. Inkjet printing is an exciting approach to high-throughput biomolecule printing, but its application to cell printing is still being tested as there are unanswered questions regarding cell viability in the presence of the thermal and mechanical stresses associated with the printing process. In addition, the feature resolution of biomolecule- and cell-based inkjet printers (~60 – 100 μm) is not yet at the single-cell level[6,33,34].

While microfluidic patterning of substrates for highly multiplexed biological sensing has been demonstrated[44], this technique has not yet been used for high-resolution multiplexing of cells. This is likely due to a number of limitations of current patterning schemes. In the most general case, multiplexed features are created by simply flowing a distinct oligo, protein, antibody, or other biomolecule or chemical into each channel within a microfluidic device. Since microfluidic channels are typically long and thin, they are well-suited to patterning high-aspect ratio features (long, thin lines or rectangles), but not low-aspect ratio features, such as the micron-scale squares or spots that would be needed for high density cell arrays. While it is possible in theory to pattern such features using modifications of the PDMS device architecture, these modifications do not come

without their own set of challenges. For example, one could envisage building a multilayer PDMS structure, such that each layer contains a fluidic network that feeds a unique biomolecule solution to a series of micron-sized spots in the patterning (first) layer[45,46]. However, the task of aligning multiple layers and creating vias connecting the layers reliably is extremely arduous, and therefore impractical for high-density multiplexing of more than 2 – 3 distinct molecules or cells.

4.2 From High Density Microarrays to Single-Cell Resolution Cell Arrays

4.2.1 Creating a dense multiplexed cell microarray

Here we show a relatively straightforward method for circumventing these limitations in microfluidic patterning, thereby facilitating high resolution biomolecule- and cell-multiplexing, while minimizing the complexities of device fabrication and processing time. The approach involves creating a densely-patterned DNA-microarray that is then converted into a dense cell-microarray.

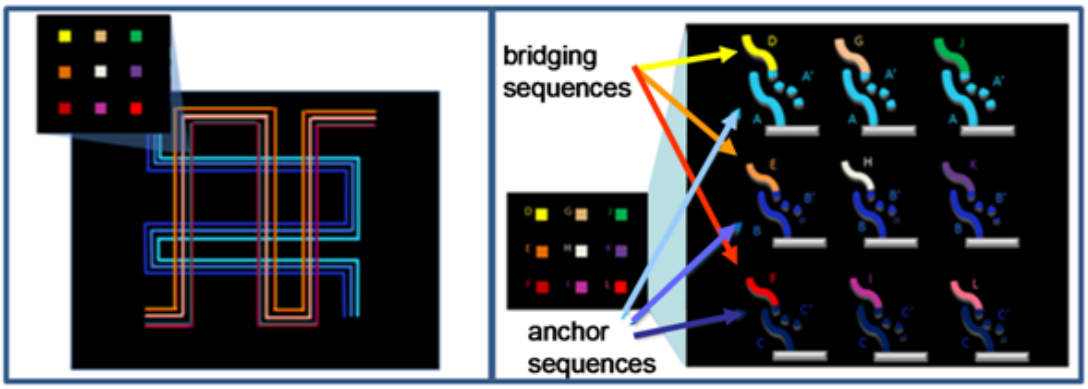

Figure 4.2. The preparation of a high density DNA microarray for tissue assembly. Illustration of the orientation of microfluidic flow patterning molds #1 (blue lines) for deposition of *n* anchor ssDNA sequences, and #2 (red lines) for patterning *m* bridging sequences. The resulting pattern is a series of *n x m* microarrays, with each array spot having its own unique chemical identity.

As shown in **Figure 4.2**, the small DNA microarray features are created in two sequential oligonucleotide flow-patterning steps, as follows: 1. A PDMS device containing a high density of parallel channels is used to flow-pattern distinct oligo strands ("anchor strands") onto a polylysine-coated glass surface. 2. The PDMS stamp is then re-oriented on the substrate 90^{o} clockwise, and a distinct set of oligos are flowed into the PDMS device to create a series of *n x m* microarrays. These oligos are designed to include a 20-base pair "tail" that is complementary to one of the anchor sequences, and a 20-base pair "head" with a unique sequence. As such, after the DNA patterning is complete, these oligos serve as intermediaries that bridge the anchor sequences with unique DNA-conjugated cells. For example, in the first patterning step, we flowed three 80-mer anchor sequences – named **A**, **B**, and **C** – in 3 adjacent channels and simultaneously repeated this flow-patterning arrangement 6 times. In the second patterning step, we flowed three sets of 3 distinct bridging strands, also in 3 adjacent channels (one set per channel): first channel - strand **A'-i** (containing both a 20-mer "tail" sequence that is complementary to anchor strand **A**, and a unique 20-mer "head"

sequence **i**), **B'-ii**, and **C'-iii**; second channel - strands **A'-iv**, **B'-v**, and **C'-vi**; third channel – strands **A'-vii**, **B'-viii**, **C'-ix**. This flow-patterning arrangement was also repeated 6 times simultaneously. The result was a series of thirty-six 3 x 3 arrays, in which each 3 x 3 array contained 9 distinct oligonucleotide "head" sequences (**i, ii, iii, iv, v, vi, vii, viii, ix**) that were available for binding of 9 distinct cell types conjugated to one of 9 complementary strands (**i', ii', iii', iv', v', vi', vii', viii', ix'**). The red squares in **Figure 4.3a** were created by hybridization of **i'**-Cy5 fluorescent DNA to the 3 x 3 array, while green squares were generated by hybridizing (**ii'-ix')**-Cy3 to the array. By adding only **A'-i**, **B'-ii**, and **C'-iii** strands in the second patterning step, creating 3 x 1 arrays was straightforward (**Figure 4.3b**). Red squares, green squares, and yellow squares were created by adding **i'**-Cy5, **iii'**-Cy3, and equal concentrations of **ii'**-Cy5 and **ii'**-Cy3, respectively. The dimensions of the square DNA features comprising the arrays exactly equal the width of the channels used to pattern them. Therefore, since the PDMS flow-patterning channels were 10 μm wide and spaced 30 μm apart, closely-packed 10 μm x 10 μm DNA squares were created that could each accommodate a distinct ~10 μm-diameter single cell.

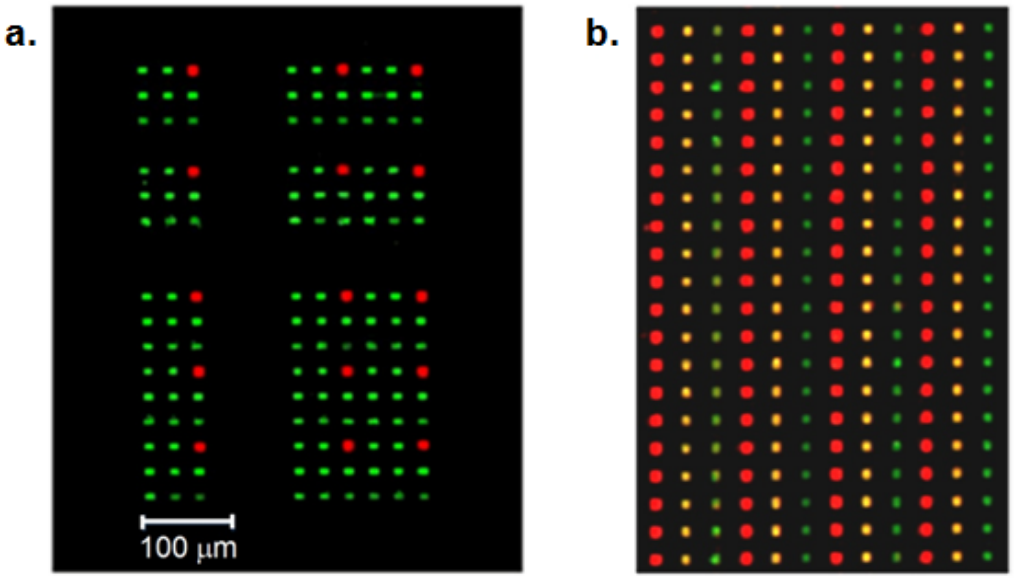

Figure 4.3. Fluorescent scans of high density DNA microarrays. a. Repeating 3 x 3 arrays (red squares = **i** oligomer; green squares = **ii, iii, iv, v, vi, vii, viii,** and **ix** oligomers). **b.** Repeating 3 x 1 arrays (red squares = **i** oligomer; yellow squares = **ii** oligomer; green squares = **iii** oligomer).

To increase the total number of repeats of these 3 x 3 array units, the number of channels in the PDMS flow-patterning device can be increased, or the entire set of channels can be designed to wind up and down in serpentine fashion across the length of the device. For example, by creating serpentine channels with 10 turns, as opposed to straight channels, the number of array repeats can be increased 100-fold (10^2), to thirty-six hundred 3 x 3 arrays.

Once the glass surface was patterned, distinct cell types, each conjugated to one of 9 "head"-complementary oligo sequences, were pipetted onto the surface, where each conjugated cell type bound to its cognate square. Once patterned, the cells were encased in a UV-curable PEG hydrogel so that their positions relative to each other were fixed. The cell-laden hydrogel was then cut into small sections and stacked on top of each other with further curing to create a three-dimensional tissue.

4.2.2 Platform design flexibility and patterning opportunities

In some sense, each DNA square and its cognate cell can be thought of as the biological equivalent of a pixel on a CCD display. The number of possible cell patterns increases exponentially with the number of orthogonal microarray squares in each grid unit - just as the number of patterns that can be displayed on a digital screen scales with the number of pixels. The sizes and spacings of these biological pixels can be tuned by the microfabrication process. More specifically, the feature sizes and spacings can be modified by adjusting the microfluidic channel widths and inter-channel distances, respectively. To allow for physical contact between cells, the feature sizes and inter-feature distances need only be downsized sufficiently. For example, by creating 5 μm-sized square features with 5 μm spacings, a 10 μm-diameter cell attached to its cognate feature will overlap the space between features to a degree, allowing it to come in contact with a neighboring cell whose footprint is also larger than its cognate square. Furthermore, by varying the widths and spacings of channels within a microfluidic device, different-sized features can coexist within the same array, accommodating cells of different sizes. By increasing feature sizes sufficiently, distinct clusters, each containing a few homotypic cells, can be patterned adjacently.

The feature geometries are also tunable to a large extent. For example, one can simply rotate the PDMS device in the second patterning step at an angle between 0^o and 90^o to create parallelograms instead of squares. Rectangles can be created simply by using a microfluidic device in the second patterning step that has different channel widths compared with the device used in the first step. Alternatively, in one of the two patterning steps, a PDMS device can be used in which each channel consists of a series of connected

circles or triangles, allowing a variety of feature shapes to be realized even within the same array unit. Since feature geometry has been shown to influence stem cell fates[32], creating customized feature geometries for each cell type to be arrayed would be very valuable in cases where stem-cells or progenitor-cells are used to pattern tissues. With the flexibility in feature sizes, spacings, and geometries potentially afforded by this platform, dense 2-D microarchitectures can be patterned with feature proximities that permit contact between single cells of varying types, closely mimicking the native tissue environment.

4.2.3 DNA conjugation of cells

In order for a cell type to be addressed to the correct square in a densely-patterned microarray, each cell type had to be labeled with a unique complementary oligonucleotide strand. Previous studies have shown variations of this method. One study showed that oligos could be modified with lipophilic end groups that could anchor the oligos directly into the cell membrane. Bertozzi et al. demonstrated the attachment of ssDNAs to cell-surface glycans by means of Staudinger ligation chemistry, but the initial step required a 3-day cell incubation period with an exogenous modified sugar metabolite to facilitate subsequent chemical steps[47]. More recent work by the same group showed that *N*-hydroxysuccinimidal (NHS) ester-modified DNAs could be reacted directly with amino groups on cell-surface proteins in under an hour[48].

Our approach to conjugating cells with DNA was relatively straightforward (**Figure 4.4**). Cells were biotinylated and then addressed via streptavidin-conjugated oligonucleotides. Our own lab's extensive experience using cysteine-engineered streptavidin (SAC)-conjugated oligos, in conjunction with biotinylated MHC proteins, to

pull down antigen-presenting T cells, inspired this method[49]. Native streptavidin contains a lysine residue in close proximity to the biotin-binding pocket, such that amide coupling strategies for cross-linking DNA would alter the streptavidin-biotin binding capacity. SAC by contrast has been genetically engineered to incorporate a cysteine residue at the carboxy-terminus, away from the biotin-binding pocket, allowing DNA to be conjugated using maleimide chemistry only at this site (since cysteine residues are absent in native streptavidin)[49]. To tailor this strategy for DNA conjugation of cells, cells were first biotinylated (by reacting with NHS-biotin), followed by incubation with their respective SAC-oligos. The advantage of this method is its modularity and ease. The reaction between the SAC-oligos and the biotinylated cells occur immediately upon mixing, so any biotinylated cell can be instantly conjugated with an oligo of one's choosing. For experiments in which cells were patterned on arrays containing different sets of DNAs, biotinylated cells were quickly reacted with the SAC-oligos relevant to each DNA array. In addition, once biotinylated, cells could in theory be passaged a few times and still retain enough surface biotins for sufficient DNA conjugation. This would permit fast DNA-conjugation of cells directly from the culture dish, obviating the need to repeat the biotinylation procedure before every experiment.

Like the conjugation method exemplified by the Bertozzi group[48], our cell conjugation method also constitutes a cell surface marker-free approach. Whereas past cell-patterning approaches utilized antibodies against cell-surface proteins to capture cells (e.g. immunopanning)[50-52], these approaches are only practical if a cell-surface protein exists in sufficient abundance to allow the cell to be held down by surface-bound antibodies[48]. For a marker with less surface density, higher affinity antibodies would be

needed to capture cells. On top of this, producing high-affinity monoclonal antibodies is a time-consuming and expensive process with variable outcomes. By contrast, biotinylation of cells, followed by binding of SAC-oligos, is a simple, generalizable platform that can be used on any cell type, regardless of whether the cell has a targetable surface marker. The cell need only have surface amino groups, which are ubiquitous due to the abundance of membrane proteins.

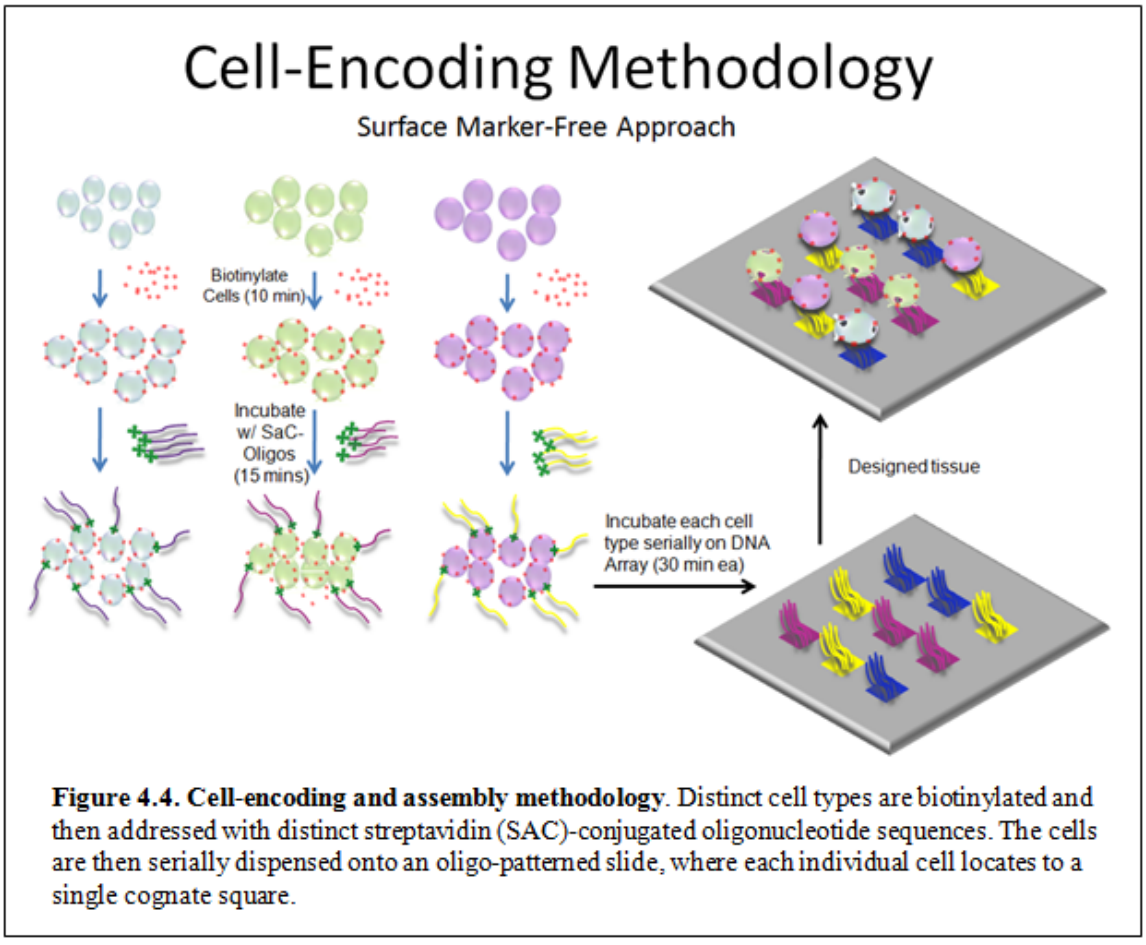

Figure 4.4. Cell-encoding and assembly methodology. Distinct cell types are biotinylated and then addressed with distinct streptavidin (SAC)-conjugated oligonucleotide sequences. The cells are then serially dispensed onto an oligo-patterned slide, where each individual cell locates to a single cognate square.

4.2.4 Patterning human central nervous system and mouse pancreatic islet tissue constructs

We first applied our patterning methodology toward creating a cell model of the human nervous system by co-assembling neurons and astrocytes into designed structures. The human CNS and neuronal systems in general are composed of neurons and glial cells interspersed in specific spatial organizations that are vital for the development of these systems[53]. Prior to integrating both cell types together, we first separately demonstrated the spatially selective capture of single astrocytes and single neurons. Primary human astrocytes were first encoded with **ii'** DNA and then incubated onto a 3 x 3 DNA microarray. The astrocytes localized only to the **ii** DNA squares, with ~27 % of squares covered by one astrocyte each). The fraction of squares covered by two astrocytes was larger (~40 %) because the astrocytes exhibited rapid division in culture, thus astrocytes that were dividing but hadn't completed mitosis could bind to a single spot (**Figure 4.5a**). Nonspecific binding of cells to non-cognate squares or to any other portions of the slide was not observed. In some cases, 3 to 4 astrocytes were found on particular **ii** DNA squares, which could be due to variability in the size of the astrocytes as well as the fact that astrocytes tend to cluster into small groups in culture. Astrocyte division was observed to continue on-chip even after the cells were patterned. In a separate experiment, primary human neurons were patterned onto the **iii** DNA spot of a 3 x 1 microarray (consisting only of oligo sequences **i**, **ii**, and **iii** as the capture sequences) to illustrate the extent of cell density (**Figure 4.5b**). A much higher percentage of the DNA squares (60 %) bound to only one cell relative to the astrocyte experiment since the neurons did not divide in culture. The cell-patterned slide was then incubated in media at 37 ^{o}C. When reassessed after 2 days, the neuronal processes were observed to be actively

growing, demonstrating that the neurons were still viable. Once the neurons were established, primary human astrocytes conjugated to **ii'** DNA were then incubated with the neuron-patterned slide and localized to their cognate squares. The final cell pattern consisted of multiple rows of primary human neurons and astrocytes spaced 30 µm apart, with each cell localized to a 10 µm x 10 µm DNA square (**Fig. 4.5c**). After incubation with astrocytes, it was clear based on cell morphology that the astrocytes were localized to the **ii** DNA squares, while the neurons remained on the **iii** DNA squares and did not move or get washed away from their initial designated locations.

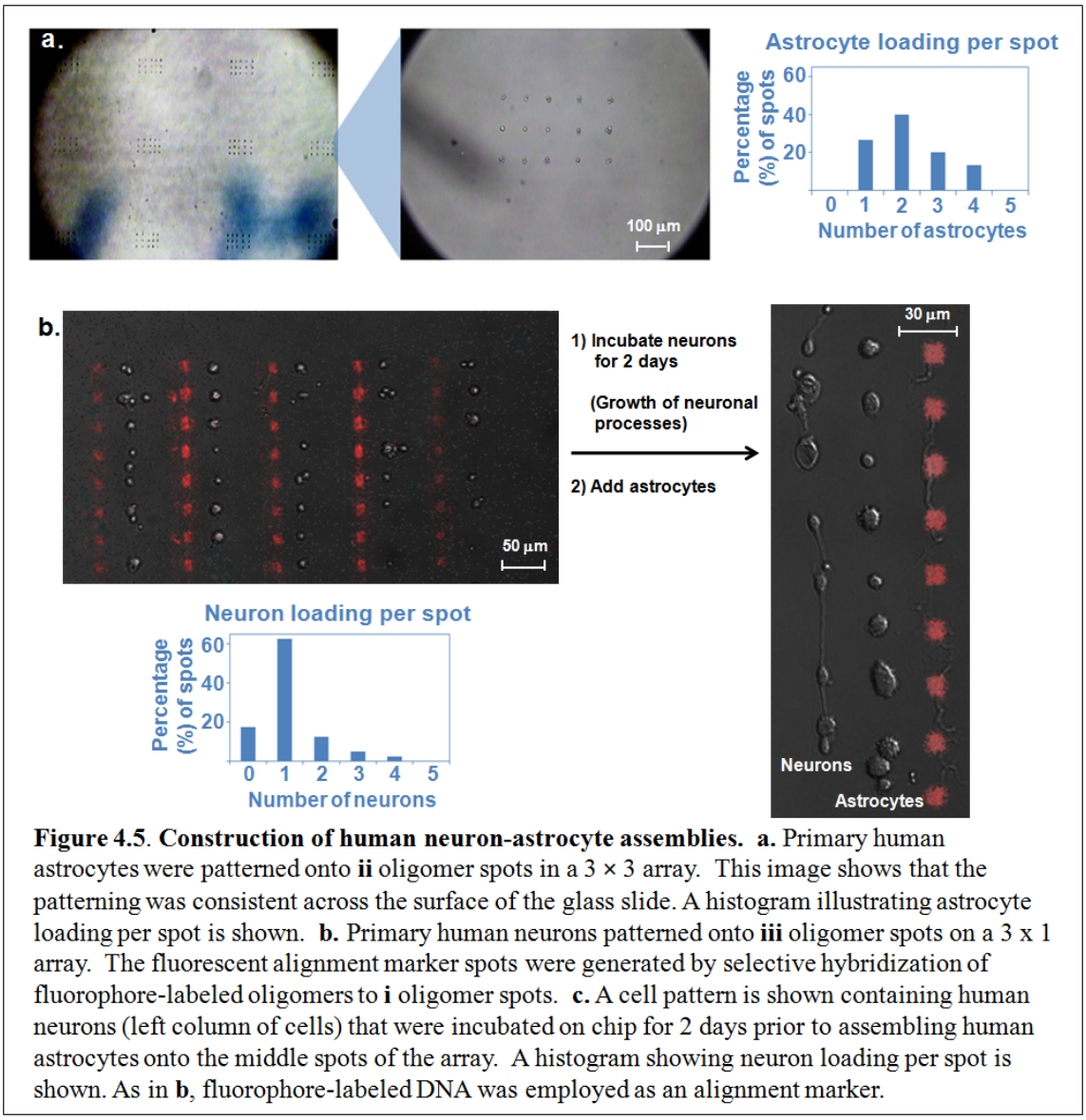

Figure 4.5. Construction of human neuron-astrocyte assemblies. **a.** Primary human astrocytes were patterned onto **ii** oligomer spots in a 3 × 3 array. This image shows that the patterning was consistent across the surface of the glass slide. A histogram illustrating astrocyte loading per spot is shown. **b.** Primary human neurons patterned onto **iii** oligomer spots on a 3 x 1 array. The fluorescent alignment marker spots were generated by selective hybridization of fluorophore-labeled oligomers to **i** oligomer spots. **c.** A cell pattern is shown containing human neurons (left column of cells) that were incubated on chip for 2 days prior to assembling human astrocytes onto the middle spots of the array. A histogram showing neuron loading per spot is shown. As in **b**, fluorophore-labeled DNA was employed as an alignment marker.

We also explored the construction of model pancreatic tissues. Some 340,000 people nationwide have diabetes mellitus type 1, which is characterized by loss of insulin production as a result of an autoimmune destruction of β cells within the pancreatic islets of Langerhans[54]. While pancreas transplants have proven to be effective in restoring normoglycemia in diabetic patients, this approach carries the risks attendant to major surgery and lifelong immunosuppression[55]. Allogeneic islet cell transplantation is a less invasive alternative, but typically is limited to patients with highly specific clinical

indications that are in addition to diabetes[55]. A promising alternative is to propagate and differentiate stem cells in culture into mature islet cells, thus yielding an unlimited number of transplantable cells[56]. However, all endocrine cell types in human islets, including the insulin-secreting β cells, the glucagon-secreting α cells, and the less abundant δ and PP cells, are arranged in apparently nonrandom architectures. We thus chose to explore our high resolution tissue engineering approach for mimicking the native islet microarchitectures.

In an effort to build a tissue that closely emulates the arrangement of cells in the human islets of Langerhans, we created an islet construct that included two mouse islet cell lines (α and β cells) patterned on the **iii** and **ii** DNA squares, respectively, of a 3 x 1 microarray with identical dimensions to that used for the neuron-astrocyte construct (**Figure 4.6**). As in the neuron-astrocyte cell patterning experiment, the α and β cells localized to their cognate DNA squares, typically averaging ~1 cell per square (~67 % of **iii** squares bound to only 1 α cell; ~87 % of **ii** squares bound to only 1 β cell). For every 100 correctly patterned cells, on average, only 1 cell bound nonspecifically, although there were examples of 2 or 3 cells patterning on a given spot (**Figure. 4.6a,b**).

We were able to designate a fraction of our arrays for conducting functional assays on the patterned cells. After the islet cells were patterned, **i'** DNA conjugated anti-insulin antibodies were incubated on the slide and allowed to hybridize to their cognate squares adjacent to the cells. The cells were incubated for 2 days to allow ample time for secreted insulin to bind to the anti-insulin antibody squares. The insulin assays were developed with biotinylated secondary antibodies followed by fluorophore-conjugated

streptavidin. The antibody squares fluoresced under confocal microscopy only when β cells were present (**Figure 4.6a-c**).

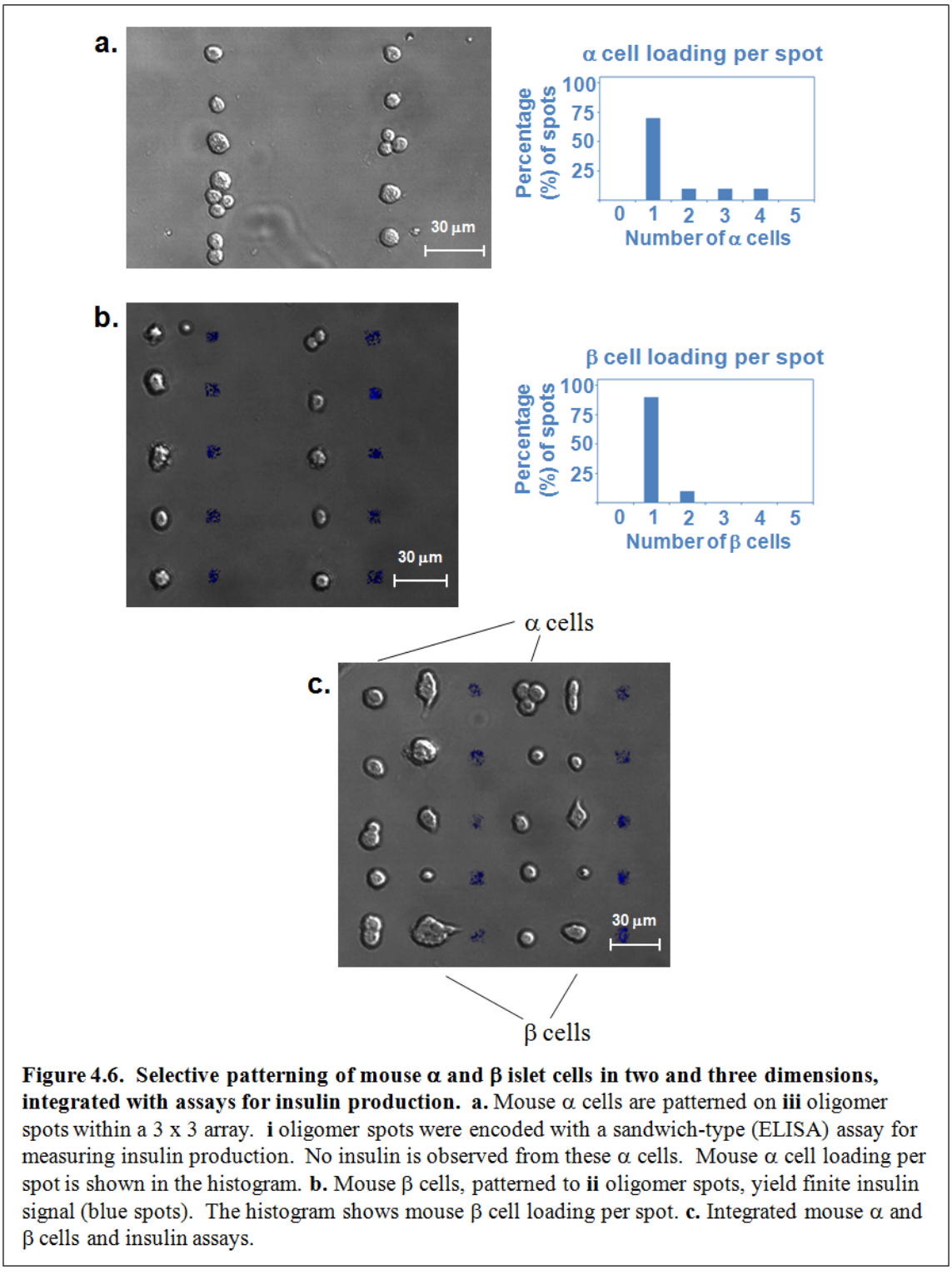

Figure 4.6. Selective patterning of mouse α and β islet cells in two and three dimensions, integrated with assays for insulin production. **a.** Mouse α cells are patterned on **iii** oligomer spots within a 3 x 3 array. **i** oligomer spots were encoded with a sandwich-type (ELISA) assay for measuring insulin production. No insulin is observed from these α cells. Mouse α cell loading per spot is shown in the histogram. **b.** Mouse β cells, patterned to **ii** oligomer spots, yield finite insulin signal (blue spots). The histogram shows mouse β cell loading per spot. **c.** Integrated mouse α and β cells and insulin assays.

Finally, we applied our platform to create islet tissue constructs in a 3-D configuration in order to more closely mimic native islet structures. Prior studies have shown that cell patterns can be encased in thin UV-curable polyethylene glycol (PEG) hydrogels and stacked to form 3-D tissue constructs.[8,57] In those studies, the cells are typically localized to the surface by nonchemical means such that cell-pattern transfer from the slide surface to the hydrogel layer is straightforward. In our case, the cells are chemically attached to the slide surface via DNA hybridization, and so it was not obvious that the cells could be readily transferred. However, we found that once the cell patterns were encased within a UV-cured PEG hydrogel, we were able to remove the cell-laden hydrogel layer from the glass surface without disturbing the cell pattern or damaging the cells. We aligned and stacked two such hydrogel layers to create a 3-D islet tissue construct (**Fig. 4.7**). This procedure could be repeated to build up multiple layers. Viability of the encased cells, as determined by calcein AM/ethidium homodimer (live/dead) staining, was confirmed after incubation in media at 37 ^{o}C for one week (**Fig. 4.7**). However, as in previous studies[8,57], cell division and mobility within the hydrogel matrix was not observed, likely due to the strong mechanical barrier provided by the rigid PEG membrane. The use of lower PEG concentrations or reduced UV light power would likely decrease this mechanical barrier, but at the expense of the rigidity needed to maintain the pattern integrity.

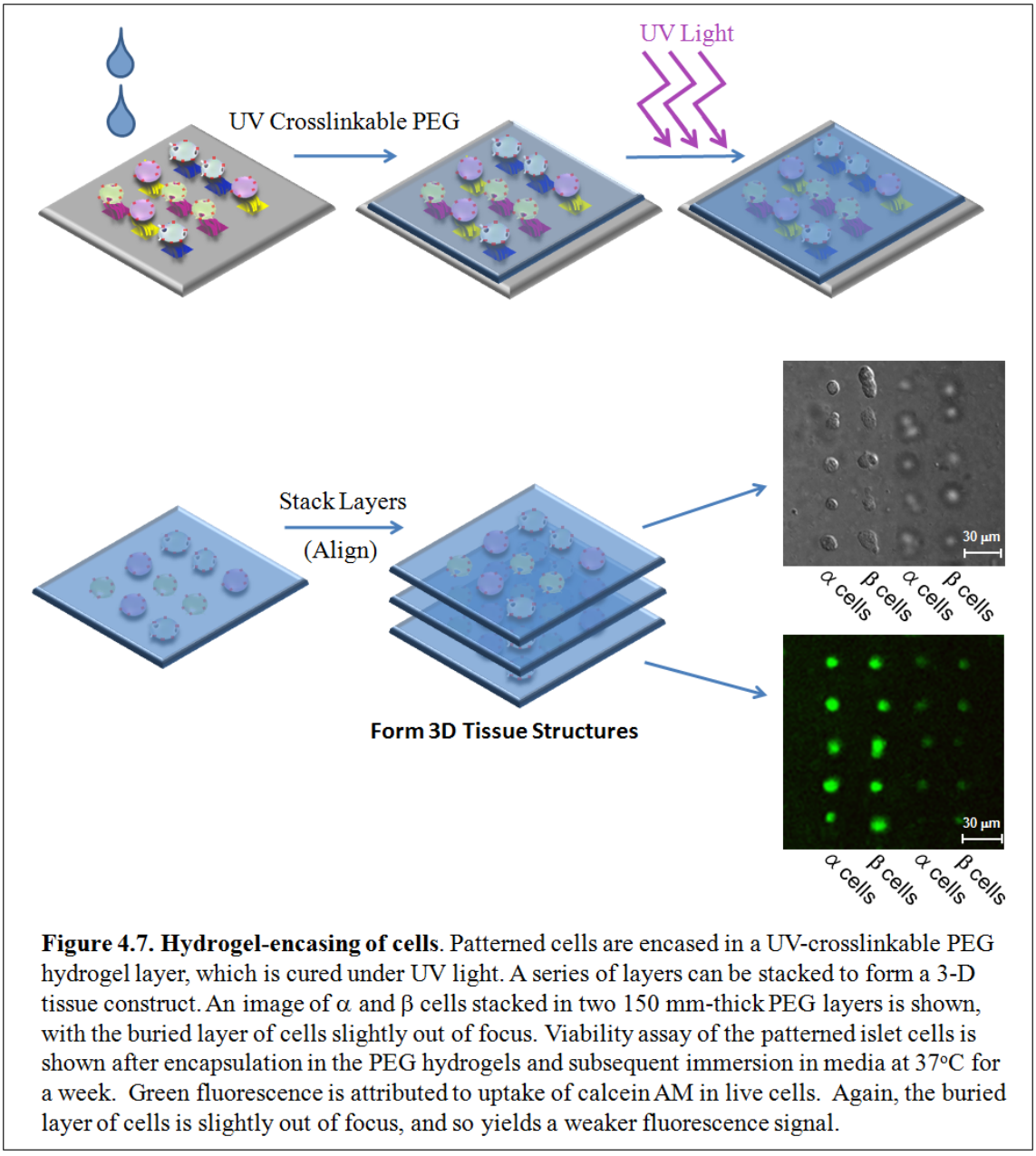

Figure 4.7. Hydrogel-encasing of cells. Patterned cells are encased in a UV-crosslinkable PEG hydrogel layer, which is cured under UV light. A series of layers can be stacked to form a 3-D tissue construct. An image of α and β cells stacked in two 150 mm-thick PEG layers is shown, with the buried layer of cells slightly out of focus. Viability assay of the patterned islet cells is shown after encapsulation in the PEG hydrogels and subsequent immersion in media at 37°C for a week. Green fluorescence is attributed to uptake of calcein AM in live cells. Again, the buried layer of cells is slightly out of focus, and so yields a weaker fluorescence signal.

The ability of our platform to act as an on-chip multiplexed ELISA technology could allow for a multitude of applications on densely patterned islet cells. For example, insulin levels could be compared to those of a series of control cultures containing equal amounts of the same 2 cell types in an unpatterned mixture of similar cell density: 1. in a culture dish (single layer of adherent cells); 2. in a single layer of cells encased in a

hydrogel; and 3. in a stacked 3-D structure. An identical set of control experiments could be carried out on *patterned* cells. Comparing insulin levels between experiments 1 and 2 would allow one to assess the effects on insulin-production of encasing islet cells in a hydrogel layer in both patterned and unpatterned scenarios. Comparing experiments 2 and 3 would allow one to determine the effect on insulin production of stacking multiple 2-D islet layers on top of each other (again in both patterned and unpatterned scenarios). Comparing patterned and unpatterned structures – be they un-encased, encased in a single hydrogel layer, or encased in a 3D hydrogel structure – would reveal whether maintaining the relative positions of the 2-cell types in 2-D and in 3-D has an effect on insulin production that differs from a structure containing a random mixture of the same cells.

A fourth experiment could compare insulin production by patterned 3-D structures comprised of aligned vs. unaligned cell layers. The cell-laden hydrogel layers could be aligned to each other using alignment markers (and a mask aligner), so that a given cell type always encounters the same neighboring cell in the layer above it (for example, a β cell in layer 2 is always above an α cell in layer 1). Such an experiment would show whether maintenance of a set cell configuration in all 3 axes of a 3-D islet tissue construct is functionally important (e.g. has an effect on insulin production) as compared with just 2 of the 3 axes.

A fifth experiment would compare insulin production by 3-D tissue constructs with that of islets isolated from a mouse. The mouse islets would be sectioned such that they contain the same number of cells as the engineered tissues. In all of the experiments just mentioned, glucagon functional assays could be performed for the other cell type (α cell) as well.

Furthermore, two-color fluorescence immunostaining for insulin and glucagon (α and β cells, respectively) could be performed on cut sections of the patterned single-layer and 3-D constructs on a routine basis. The intensity and distribution of immunostaining in these sections could provide additional functional information that ELISA could not. For example, on chip ELISA assays may not be sensitive enough to detect insulin production from a relatively small number of patterned cells. In addition, if insulin levels in the tissue media are low, it would be useful to know whether the problem is that: 1. the β cells are producing little or no insulin, or 2. the β cells are producing insulin but cannot secrete it. Both of these scenarios would be problematic in the context of a transplant, and would require further tinkering with the design parameters. Immunostaining would also show whether cells have migrated or otherwise deviated from their original configuration on the slide or in the hydrogel. These experiments could continue to be repeated for at least a month or for as long as the cells are viable.

4.3 Experimental Methods

4.3.1 Mold and device fabrication

Briefly, a 5-inch chrome mask drafted with the mold design (using AutoCAD software) and 4-inch silicon wafers were sent to a semiconductor processing foundry (Integrated Systems, Inc. ISSYS) for DRIE processing to create a silicon hard mold with 40 μm thick features. The design consisted of a series of twenty 10-μm wide serpentine channels (with 3 turns) spaced 30 μm apart. The hard mold was then placed in a chlorotrimethylsilane (TCMS) vapor chamber for 20 minutes. A PDMS mixture (10 parts

Sylgard 184 A:1 part Sylgard 184 B curing agent) was poured onto the mold in a petri dish, degassed for 1 hour in a vacuum dessicator, and then baked at 80 ^{o}C until the samples were softly cured (~20 min). The PDMS mold replica was then cut out of the bulk PDMS and through-holes were punched at the locations of the channel inlets and outlets. The microfluidic mold replica was then rinsed with IPA and DI water, airgun dried, and dust was removed with scotch tape. The device was then centered on a clean polylysine-coated glass slide and bonded by baking for 4 hours at 80 ^{o}C.

4.3.2 Validation of oligonucleotide set

The oligonucleotide sequences were chosen based on a pre-validated set of 12 orthogonal 40-mer oligos, each containing a unique 20-mer sequence followed by a 20-mer poly-A tail. These oligos had originally been screened for having very low calculated melting temperatures for hair-pin structures, self-hybridization, and cross-hybridization. Three of the sequences served as anchor sequences, with their complements serving as the “tail” portions of the bridging sequences. The other 9 sequences served as the “head” portions of the bridging sequences, with their complements serving as the conjugate strands for the cells. The 20-mer head and tail sequences were appended to each other via a 20-mer polyA sequence, creating a 60-bp bridging sequence. For the anchor oligonucleotides, a length of 80 base pairs (two identical 40-mer sequences (appended end-to-end) was found to be optimal in ensuring sufficient contact area with the polylysine surface to anchor the cells.

4.3.3 First flow-patterning step

1. 100 μM solutions of oligos **A**, **B**, and **C** ("anchor" sequences) were flowed into channels 1, 2, and 3 respectively. This was simultaneously repeated for each additional set of three channels. The solutions were flowed in at around 3 psi via external 23-gauge pin adapters connected to Tygon lines, which were hooked up to an external pressure source and pressure gauge. The solutions were flowed until 1 μL droplets formed at the outlets, indicating the channels were completely filled.
2. The device was then stored in a dessicator at room temperature for 2 days to allow for complete evaporation of water, leaving behind the DNA stripes on the substrate.
3. The PDMS was then peeled away and the patterned glass slide was baked at 80 ^{o}C for 2 – 4 hours to facilitate DNA bonding to the polylysine-coated slide.
4. In the meantime, a second PDMS mold replica was fabricated and rinsed thoroughly with IPA and DI H_2O, then airgun dried, and dust was again removed using scotch tape.
5. Once removed from the oven, the slide was allowed to cool to room temperature and rinsed briefly with DI H_2O to remove excess salts and unbound DNA, then dried with an airgun.
6. The second PDMS mold replica was then placed on the patterned slide oriented 90^{o}-clockwise with respect to the original position of the first PDMS mold replica in the first patterning step.
7. The device was then baked at 80 ^{o}C for 4 hours (for stronger bonding)

4.3.4 Second flow-patterning step

1. 3 % BSA/PBS blocking buffer was then flowed into all device channels for one hour at 3 psi.
2. For 3 x 3 Arrays: Solutions 1, 2, 3 (bridging sequences) were flowed into channels 1, 2, and 3, respectively, for one hour at 3 psi. This was simultaneously repeated for each additional set of three channels in the device. **Solution 1**: 50 µM each of oligo strands **A'-i**, **B'-ii**, **C'-iii**; **solution 2**: 50 µM each of oligo strands **A'-iv**, **B'-v**, and **C'-vi**; **solution 3**: 50 µM each of oligo strands **A'-vii**, **B'-viii**, and **C'-ix**.
3. For 3 x 1 Arrays: Solution 1 was flowed into multiple adjacent channels.
4. 3 % BSA/PBS buffer was then flowed into each channel for 1 hour to remove excess unbound DNA.
5. The PDMS was then peeled off, and the slide was incubated in a 3 % BSA/PBS bath (to block areas previously in contact with the PDMS), followed by rinsing with PBS, and airgun drying. (Rinsing with DI water was avoided at this step because it could dissociate the hybridized anchor and bridging strands).

4.3.5 DNA microarray validation

Once these DNAs were patterned into densely packed 3 x 3 grids or 3 x 1 grids, the patterned slide underwent a second cross-talk validation assay (now using just the 9 dye-conjugated complements **i'** through **ix'**) to ensure that no new crosstalk had been introduced by having two orthogonal sequences tethered into a single bridging sequence. This assay also served to assess whether there was leakage between microfluidic

patterning channels, which would manifest as smearing of the fluorescent signal between oligo squares in the grid.

4.3.6 Conjugating cells with DNA

1. Prior to conjugation, media was decanted from the cell culture dishes and the dishes were rinsed 3 times with 1x PBS.
2. Each dish was then incubated at room temperature for 10 minutes with 3 mL of a 40 μM solution of NHS-biotin in PBS (Solulink protocol).
3. The culture dishes were then rinsed 3 times with media to remove excess unreacted biotin.
4. 3 μL of 1 mg/mL SaC-oligo in 1 mL of 3 % BSA/PBS was added to each dish, followed by incubation at 37 ^{o}C for 5 minutes. The biotin-streptavidin binding reaction is complete in under 1 minute, but the reaction can proceed longer without causing harm to the cells. **iii'**-SaC was used to address α cells and neurons; **ii'**-SaC was used to address β cells and astrocytes.
5. The culture dishes were then rinsed again with 3 % BSA/PBS 3 times to remove excess unbound SaC-oligo.
6. 3 mL of warm (37 ^{o}C) trypsin was added to each culture dish and allowed to incubate for 3 minutes at 37 ^{o}C (to detach cells), followed by 5 mL trypsin-neutralizing solution and 5 mL of media.
7. Each cell suspension was then centrifuged at ~150 RCF for 5 min in a 15 mL falcon tube. The supernatant was aspirated, and oligo-conjugated cells were resuspended at a concentration of 10 million cells / mL in 2 μM EDTA in 3 % BSA/PBS.

4.3.7 Cell culture

All cell cultures were incubated in a 37 ^{o}C humidity-controlled incubator with 5 % CO_2/95 % air. Mouse cell-line derived pancreatic α cells (alpha TC1 clone 6, ATCC, Manassas, VA) were cultured in DMEM (Invitrogen Cat. No. 31600-034) containing: 10 % FBS (heat-inactivated), 15mM HEPES, 0.1 mM non-essential amino acids, 0.02 % BSA, 1.5 g/L sodium bicarbonate, 3.0 g/L glucose. Mouse cell-line derived pancreatic β cells (Beta-TC-6, ATCC) were cultured in 15 % FBS/DMEM. Experiments were conducted a week after plating. Human Primary Neurons (ScienCell Research Labs, Carlsbad, CA) were cultured in Neuronal Medium (ScienCell), and used for experiments 2 days after plating. Human Primary Astrocytes (ScienCell) were cultured and continued to divide in Astrocyte Medium (ScienCell) and were used 4 days after plating.

4.3.8 Cell patterning

Serial Processing:

1. Two distinct experiments were carried out, one with neurons and astrocytes and one with α cells and β cells
2. 200 µL of a single oligo-conjugated cell type (2 million cells total) was pipetted onto a pre-blocked ultra-dense oligo-patterned slide, followed by incubation at 37 ^{o}C for 30 min.
3. The cell-patterned slide was then swirled lightly in 3 % BSA/PBS to remove non-specifically bound cells.
4. This procedure was then repeated on the same slide (either immediately or within a couple days) using the second oligo-conjugated cell type.

5. A dye-conjugated DNA reference marker (50 nM **i'**-Cy3) was added prior to patterning of the cells to assess whether the cells were binding to the correct squares (relative to the reference marker).

4.3.9 Cell binding specificity

To assess whether oligo-conjugated cells bind only to their cognate DNA spots requires either that the morphologies of the patterned cell types be sufficiently distinct to be discernable under conventional light microscopy, or that each cell type be labeled with a distinct (fluorescent) marker. In this case, neurons and astrocytes could be clearly distinguished based on morphology. Likewise, α and β cells could be easily distinguished based on morphology. However, if fluorescent labeling were desired, it could be accomplished prior to the cell-patterning step by labeling the two cell types with distinct membrane-permeable dyes (e.g. Blue, Yellow, or Red Cell-Labeling Solutions from Molecular Probes: DiO, DiI, and DiD). Based on the cells' positions relative to the reference square (on examination under a fluorescent confocal microscope), one can straightforwardly determine whether each cell type has bound to the correct squares. Multiple array units can be examined to statistically analyze patterning reliability.

4.3.10 Hydrogel encapsulation of cells[8]

1. A 10 % solution of PEG-DA (MW 3400) in DMEM was filtered through a filter membrane with 0.2 μm pores.
2. Separately, 30 mg of 2,2-Dimethoxy-2-phenylacetophenone (DMPA) photoinitiator was dissolved in 100 μL N-vinylpyrrolidone.

3. 10 µL of DMPA solution was then added to 1 mL of PEG-DA solution and vortexed.
4. 150 µm-thick polished glass coverslips were then placed on the cell-patterned polylysine slide on either side of the cell-patterned area. A third coverslip was positioned such that it bridged the first two, creating a channel in which the cell-patterned glass substrate served as the floor, and the 3 coverslips served as the walls and ceiling.
5. The PEG pre-polymer solution was then pipetted into this channel and cured for 5 minutes under a UV lamp at 4 mW/cm^2 to form a thin (50 µm) hydrogel layer encasing the cells. The hydrogel layer was then peeled off keeping the cell pattern within intact.
6. By stacking multiple such layers on top of each other either with or without alignment, a three-dimensional tissue-like structure could be created.
7. The single-layer tissue or 3-D tissue construct was then placed in a culture dish with media.

4.3.11 Cell function assessment

Approximately 200 µL of a 5 µg/mL **i'**-anti-insulin Ab (R&D Systems, Minneapolis, MN) DNA-antibody conjugate in 15 % FBS/DMEM media solution was added to an islet cell patterned slide and allowed to hybridize to the squares of **i** DNA, followed by incubation at 37 ^oC for 2 days to allow insulin from nearby β cells to bind the conjugate. The slide was then gently rinsed three times with media followed by addition of a 200 µL solution of 2 µg/mL biotinylated insulin detection antibody (GeneTex, Irvine, CA) in media, which was allowed to incubate at 37 ^oC for 1 hour.

Again, the slide was gently rinsed three times with media, followed by a 1 hour incubation at 37 ^{o}C of a 200 µL solution of 5 µg/mL streptavidin-Cy5 conjugate (eBioscience, San Diego, CA) for fluorescence detection. A final triple rinse with media was performed.

4.4 Discussion

The proper functioning of tissues depends on the precise architectural arrangement of various cell types, facilitating the types of cell-cell interactions necessary for cell growth, differentiation, survival, migration, and regulation of tissue function. Consequently, it is believed that by mimicking the cellular and extracellular microarchitectural arrangements found in native tissues and organs, it will be possible to engineer substitutes that exhibit the same or very similar functions. The ability to arrange cells and cell types at single-cell resolution, as shown here, would enable new opportunities to more accurately mimic complex microarchitectures, like those seen in pancreatic islets, nervous tissue, and other organs.

It would be beneficial to see the islet cell construct function as well as native islet tissue. For one thing, human pancreatic islets consist predominantly of β (60 %) and α cells (30 %), with δ and PP cells constituting a small minority[23]. The construct shown here contains a distinct cell type on each of 2 squares in a repeating 3 x 1 array to demonstrate the multiplexing capability of the platform. As a result, both cell types are found in equal densities. This also means that, whereas native tissue consists predominantly of β cell / β cell, α cell / α cell, and α cell / β cell interactions, both cells types in the tissue constructed here could always interact with each other. Another

consequence of having equal numbers of each cell type is that the number of insulin-secreting β cells per unit volume of tissue is lower than in the native tissue, which could impact the level of insulin secretion. Further diminishing the cell density per unit volume is the thickness of the hydrogel layers. Each 150 μm-thick hydrogel layer contains just a single layer of cells. Since the cells are about 10 μm in diameter on average, the resulting gap between cell layers in the 3-D construct is about 140 μm. This also results in intercellular contacts being possible only in the x-y plane but not in the z-direction.

To address these issues, there are various ways in which islet structure can be more closely mimicked. Since cellular arrangement is hypothesized to affect cell viability and insulin production, future experiments could examine the effects of varying the pattern and distribution of the various cell types. These variations could include: 1. a checkerboard pattern of α and β cells (somewhat like the human or monkey islet), with or without interspersed δ and PP cells at regular intervals; or 2. an inner core of β cells surrounded by an outer mantle of α cells, and to a lesser extent δ and PP cells, as in the "core-mantle" model of the mouse islet[23]. The number of cells in the core and mantle can be tuned by adjusting the feature sizes, or by increasing the number of spots in each grid unit.

Furthermore, methods of narrowing the spacing between layers could be explored so as to allow for cell-cell contacts in all three axes. The hydrogel layer thickness is determined by the thickness of the coverslips used as the templates. Once 10 μm-thick coverslips are attainable, the hydrogel layer thickness will permit cell contacts in all 3 axes. In principle, an alternative would be to run a cell/PEG-prepolymer solution through a 10 μm-high microfluidic channel over the DNA patterned glass surface. Once the cells

bind to their cognate squares, the PEG matrix around them would be cured under UV. The PDMS would then be peeled off, leaving a 10 μm-thick cell-laden hydrogel stacking layer. In addition, since islets tend to assume a spherical glandular structure, the various layers could be cut into circular sections of varying radii which, when stacked, form hemispherical or spherical structures. Alternatively, a 3-D construct created from equal-sized stacks could, upon completion, be cut or punched to produce numerous tiny cylinders, spheres, or hemispheres of tissue.

Additional experiments could also explore modifying the extracellular environment and vascularizing the constructs to extend tissue longevity. Covalent attachment of extracellular matrix proteins (collagen, laminin, fibronectin) or peptides (RGD, IKVAV) to the hydrogel matrix would more closely mimic the extracellular environment of islet cells and prevent anoikis (apoptosis due to lack of cell-cell or cell-ECM interaction). To create much larger stacks of patterned hydrogel layers would require some mechanism of adequately perfusing the various layers since diffusion becomes limiting in hydrogel systems within a few tens of microns. This might be accomplished by lithographically imprinting capillary-like microchannels in each PEG hydrogel layer. Inlet and outlet holes could then be punched at either end of the 3-D construct, allowing perfusion of the imprinted capillary bed and its adjacent cells. Alternatively, a multitude of spherically-cut tissue sections could be packed into a rigid, hollow casing (like beads in a column) which can be perfused with media or blood. If hooked up to an arterial supply, the blood would permeate through the micron-sized spaces between the beads much as it would through capillary beds in real tissues.

4.5 Conclusion

In summary, we have patterned ultra-dense DNA microarrays for multiplexed single cell resolution cell patterning with applications in tissue engineering. We created two tissue constructs, one made up of two human central nervous system cell types (neurons and astrocytes) and one consisting of two mouse pancreatic islet cell types (α and β cells). Cell viability was confirmed in both constructs, and cell function was established in the islet cell construct through the detection of insulin secretion. In addition, islet cells were successfully transferred into PEG hydrogels and assembled into 3D tissue structures. These results imply that this cell patterning technology has the potential to be utilized for tissue engineered implants in individuals with compromised organ function.

4.6 Future Outlook

In addition to enabling the engineering of constructs that mimic more complex native microarchitectures, this platform could also offer the unique opportunity to create customizable tissues with novel microarchitectures. In particular, this platform could facilitate precise positioning and contact between cells that might not ordinarily be found together in native tissues. For example, neurons could be patterned alongside stomach cells that produce obestatin – an appetite-suppressant protein – creating a tissue that could one day facilitate voluntary nervous system control over appetite suppression for obese individuals. Clearly, ligand and receptor modifications would have to be genetically engineered to allow for communication between cell types that ordinarily do

not communicate. Also, the numbers and ratios of cell types in an engineered tissue could be adjusted to optimize that tissue's performance. For example, the relative positions and ratios of oligodendrocytes and neurons patterned in a customized nervous tissue transplant could be adjusted to enable improved myelination, synaptic connections, and neuronal functionality.

Given the multiplexing resolution that this technology enables, the door would be opened to a broad spectrum of other applications outside of tissue engineering. For instance, it would be possible to conduct cell-cell communication assays involving detection of cytokines or other secreted proteins from different types of single cells. To illustrate, a single glioblastoma (GBM) cancer cell and a single macrophage could be positioned at diagonal corners of a 3 x 3 array unit. The other 7 squares within the array could be occupied by a series of anti-cytokine and anti-growth factor antibodies. The cells could be given a specified amount of time (48 – 72 hours) to communicate in the presence of a stimulatory factor (like LPS), after which point labeled detection antibodies would be introduced and the intensities of each secreted cytokine measured. As a control, the same experiments could be conducted on each cell separately (equivalent of a highly multiplexed ELISPOT) to compare the relative contributions of each single cell secretion profile to the secretion of the dual-cell system. Because each of these 3 x 3 array units are repeated hundreds of times on a single slide, large sample sizes are afforded for statistical analysis.

This platform could also open up new opportunities in cell-based sensing, drug testing, and drug discovery, as assays could be performed on multiple tissue types on the same slide. For example, one could bond a PDMS stamp containing 10 separate channels

on top of the densely patterned DNA array. Different cell types and combinations could then be introduced into each microfluidic channel, where the conjugated cells would localize to their cognate squares, resulting in a different tissue type within each channel. Once cultured for a few days within the channels (under constant flow of media), a test drug could be introduced into each channel, and the outflow medium as well as the cells themselves could subsequently be analyzed. In this manner, drug effects could be straightforwardly tested on a number of different cells, cell combinations, or tissues simultaneously.

Finally, this patterning technology could be used for whole-genome or whole-proteome analyses on minute sample sizes for research purposes or for point-of-care diagnostics (**Figure 4.8**). Considering the small feature sizes possible (10 μm squares with 30 μm pitch), a set of 40,000 genes or proteins could be profiled within a microfluidic channel that is 500 μm wide and a few centimeters long. Twice that number could be profiled in a channel with twice the length or width. Moreover, by varying the number of assay channels, multiple low-volume samples could each be assayed for thousands of genes or proteins on a single chip.

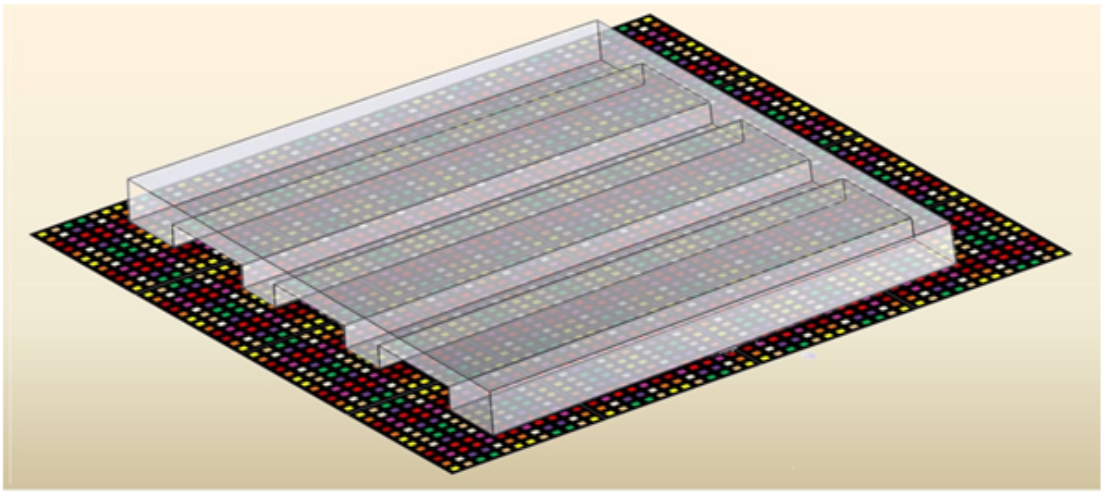

Figure 4.8. Scaled-up multiplexing. At the dimensions of the oligonucleotide squares (~10 μm resolution), hundreds or even thousands of distinct DNA strands could, in principle, be patterned within a single microfluidic channel, allowing for whole-genome and whole-proteome studies to be performed on extremely small (microliter) volumes within separate microfluidic channels.

4.7 References

1. Maemura, T.; Shin, M.; Sato, M.; Mochizuki, H.; Vacanti, J. A tissue-engineered stomach as a replacement of the native stomach. *Transplantation*, **2003**, 76, 61.

2. Grikscheit, T.; Ochoa, E.; Srinivasan, A.; Gaissert, H.; Vacanti, J. Tissue-engineered esophagus: experimental substitution by onlay patch or interposition. *J. Thorac. Cardiovasc. Surg.*, **2003**, 126, 537-544.

3. Vacanti, M. P.; et al. Tissue-engineered spinal cord. *Transplant Proc.*, **2001**, 33, 592-598.

4. Vacanti, J. P. Tissue and organ engineering: Can we build intestine and vital organs? *J. Gastrointest. Surg.*, **2003**, 7, 831-835.

5. Langer, R.; Vacanti, J. Tissue engineering. *Science*, **1993**, 920-926.

6. Boland, T.; Mironov, V.; Gutowska, A.; Roth, E.; Markwald, R. Cell and organ printing 2: fusion of cell aggregates in three-dimensional gels. *Anat. Rec. A Discov. Mol. Cell. Evol. Biol.*, **2003**, 272, 497-502.

7. Stegemann, J.; Kaszuba, S.; Rowe, S. Review: advances in vascular tissue engineering using protein-based biomaterials. *Tissue Eng.*, **2007**, 13, 2601-2613.

8. Albrecht, D.; Underhill, G.; Wassermann, T.; Sah, R.; Bhatia, S. Probing the role of multicellular organization in three-dimensional microenvironments. *Nat. Methods*, **2006**, 3, 369-375.

9. Tibbitt, M.; Anseth, K. Hydrogels as extracellular matrix mimics for 3D cell culture. *Biotechnol. Bioeng.*, **2009**, 103, 655-663.

10. Beck, J.; et al. Islet encapsulation: strategies to enhance islet cell functions. *Tissue Eng.*, **2007**, 13, 589-599.

11. Weber, L.; Hayda, K.; Anseth, K. Cell-matrix interactions improve β-cell survival and insulin secretion in three-dimensional culture. *Tissue Eng. A*, **2003**, 14, 1959-1968.

12. Ling, Y.; et al. A cell-laden microfluidic hydrogel. *Lab Chip*, **2007**, 7, 756-762.

13. Orive, G.; et al. Cell encapsulation: promise and progress. *Nat. Med.*, **2003**, 9, 104-107.

14. de Vos, P.; Marchetti, P. Encapsulation of pancreatic islets for transplantation in diabetes: the untouchable islets. *Trends Mol. Med.*, **2002**, 8, 363-366.

15. Weber, L.,; He, J.; Bradley, B.; Haskins, K.; Anseth, K. PEG-based hydrogels as an in vitro encapsulation platform for testing controlled [beta]-cell microenvironments. *Acta Biomater.*, **2006**, 2, 1-8.

16. Robitaille, R.; et al. Studies on small (< 350 μm) alginate-poly-L-lysine microcapsules. V. Determination of carbohydrate and protein permeation through microcapsules by reverse-size exclusion chromatography. *J. Biomed. Mater. Res. A*, **2000**, 50, 420-427.

17. Koh, W.; Revzin, A.; Pishko, M. Poly (ethylene glycol) hydrogel microstructures encapsulating living cells. *Langmuir*, **2002**, 18, 2459-2462.

18. Koizumi, S.; Fujishita, K.; Inoue, K. Regulation of cell-cell communication mediated by astrocytic ATP in the CNS. *Purinergic Signal*., **2005**, 1, 211-217.

19. Haydon, P. G. Glia: listening and talking to the synapse. *Nature Rev. Neurosci.*, **2001**, 2, 185-193.

20. Ransom, B.; Behar, T.; Nedergaard, M. New roles for astrocytes (stars at last). *Trends Neurosci.*, **2003**, 26, 520-522.

21. Jain, R.; Lammert, E. Cell–cell interactions in the endocrine pancreas. *Diabetes Obes. Metab.*, **2009**, 11, 159-167.

22. Le Marchand, S.; Piston, D. Glucose suppression of glucagon secretion. *J. Biol. Chem.*, **2010**, 285, 14389.

23. Cabrera, O.; et al. The unique cytoarchitecture of human pancreatic islets has implications for islet cell function. *P. Natl. Acad. Sci. USA*, **2006**, 103, 2334.

24. Shear, J.; et al. Single cells as biosensors for chemical separations. *Science*, **1995**, 267, 74.

25. Rider, T.; et al. AB cell-based sensor for rapid identification of pathogens. *Science*, **2003**, 301, 213.

26. Ziauddin, J.; Sabatini, D. Microarrays of cells expressing defined cDNAs. *Nature*, **2001**, 411, 107-110.

27. Beske, O.; Goldbard, S. High-throughput cell analysis using multiplexed array technologies. *Drug Discov. Today*, **2002**, 7, S131-S135.

28. Kleinfeld, D.; Kahler, K.; Hockberger, P. Controlled outgrowth of dissociated neurons on patterned substrates. *J. Neurosci.*, **1988**, 8, 4098.

29. Revzin, A.; Tompkins, R.; Toner, M. Surface engineering with poly (ethylene glycol) photolithography to create high-density cell arrays on glass. *Langmuir*, **2003**, 19, 9855-9862.

30. Cukierman, E.; Pankov, R.; Stevens, D.; Yamada, K. Taking cell-matrix adhesions to the third dimension. *Science's STKE*, **2001**, 294, 1708.

31. Singhvi, R.; et al. Engineering cell shape and function. *Science*, **1994**, 264, 696.

32. Chen, C.; Mrksich, M.; Huang, S.; Whitesides, G.; Ingber, D. Geometric control of cell life and death. *Science*, **1997**, 276, 1425.

33. Wilson Jr, W. & Boland, T. Cell and organ printing 1: protein and cell printers. *Anat. Rec. A Discov. Mol. Cell. Evol. Biol.*, **2003**, 272, 491-496.

34. Xu, T.; Jin, J.; Gregory, C.; Hickman, J.; Boland, T. Inkjet printing of viable mammalian cells. *Biomaterials*, **2005**, 26, 93-99.

35. Jiang, X.; Ferrigno, R.; Mrksich, M.; Whitesides, G. Electrochemical desorption of self-assembled monolayers noninvasively releases patterned cells from geometrical confinements. *J. Am. Chem. Soc.*, **2003**, 125, 2366-2367.

36. Lahann, J.; et al. A reversibly switching surface. *Science*, **2003**, 299, 371.

37. Ostuni, E.; Kane, R.; Chen, C.; Ingber, D.; Whitesides, G. Patterning mammalian cells using elastomeric membranes. *Langmuir*, **2000**, 16, 7811-7819.

38. Folch, A.; Jo, B.; Hurtado, O.; Beebe, D.; Toner, M. Microfabricated elastomeric stencils for micropatterning cell cultures. *J. Biomed. Mater. Res. A*, **2000**, 52, 346-353.

39. Rettig, J.; Folch, A. Large-scale single-cell trapping and imaging using microwell arrays. *Anal. Chem.*, **2005**, 77, 5628-5634.

40. Birkbeck, A.; et al. VCSEL arrays as micromanipulators in chip-based biosystems. *Biomed. Microdevices*, **2003**, 5, 47-54.

41. Dufresne, E.; Grier, D. Optical tweezer arrays and optical substrates created with diffractive optics. *Rev. Sci. Instrum.*, **1998**, 69, 1974.

42. Ozkan, M.; et al. Electro-optical platform for the manipulation of live cells. *Langmuir*, **2003**, 19, 1532-1538.

43. Rosenthal, A.; Voldman, J. Dielectrophoretic traps for single-particle patterning. *Biophys. J.*, **2005**, 88, 2193-2205.

44. Fan, R.; et al. Integrated barcode chips for rapid, multiplexed analysis of proteins in microliter quantities of blood. *Nat. Biotechnol.*, **2008**, 26, 1373-1378.

45. Erickson, D.; Li, D. Integrated microfluidic devices. *Anal. Chim. Acta*, **2004**, 507, 11-26.

46. Jo, B.; Van Lerberghe, L.; Motsegood, K.; Beebe, D. Three-dimensional micro-channel fabrication in polydimethylsiloxane (PDMS) elastomer. *J. Microelectromech S.*, **2000**, 9, 76-81.

47. Chandra, R.; Douglas, E.; Mathies, R.; Bertozzi, C.; Francis, M. Programmable cell adhesion encoded by DNA hybridization. *Angew. Chem. Int. Edit.*, **2006**, 45, 896-901.

48. Hsiao, S.; et al. Direct cell surface modification with DNA for the capture of primary cells and the investigation of myotube formation on defined patterns. *Langmuir*, **2009**, 25, 6985-6991.

49. Kwong, G.; et al. Modular nucleic acid assembled p/MHC microarrays for multiplexed sorting of antigen-specific T cells. *J. Am. Chem. Soc.*, **2009**, 131, 9695-9703.

50. Gard, A. L.; Pfeiffer, S. E.; Williams, I. Immunopanning and developmental stage-specific primary culture of oligodendrocyte progenitors (O4+ GalC) directly from postnatal rodent cerebrum. *Neuroprotocols*, **1993**, 2, 209-218.

51. Yang, P.; Hernandez, M. Purification of astrocytes from adult human optic nerve heads by immunopanning. *Brain Res. Protoc.*, **2003**, 12, 67-76.

52. Ingraham, C.; Rising, L.; Morihisa, J. Development of O4+/O1-immunopanned pro-oligodendroglia in vitro. *Dev. Brain Res.*, **1999**, 112, 79-87.

53. Yang, I. H.; Co, C.C.; Ho, C.-C. Spatially controlled co-culture of neurons and glial cells. *J. Biomed. Mater. Res.*, **2005**, 75, 976-984.

54. Fauci, A. *Harrison's Principles of Internal Medicine*. McGraw-Hill: New York, 2005.

55. Jones, P.; Courtney, M.; Burns, C.; Persaud, S. Cell-based treatments for diabetes. *Drug Discov. Today*, **2008**, 13, 888-893.

56. Burt, R. K.; Oyama, Y.; Traynor, A.; Kenyon, N. S. Hematopoietic stem cell therapy for type 1 diabetes: induction of tolerance and islet cell neogenesis. *Autoimmun. Rev.*, **2002**, 1, 133-138.

57. Liu, V. A.; Bhatia, S. N. Three-dimensional photopatterning of hydrogels containing living cells. *Biomed. Microdevices,* **2002**, 4, 257-266.

4.8 Appendix

To validate that the designed oligo set was truly orthogonal, cross-talk assays were performed on the twelve oligos. First, the twelve primary strands were array-spotted on a polylysine-coated glass slide, baked at 80 ^{o}C for 2 – 4 hours, rinsed briefly with DI water, and airgun dried. A thin slab of PDMS with 12 pre-cut square holes was then bonded to the spotted glass slide, forming 12 assay wells. The wells were then blocked with 3 % BSA/PBS for an hour. Twelve solutions, each containing 50 nM of a distinct dye-conjugated complementary strand in 3 % BSA/PBS, were prepared and pipetted into the wells, such that each well was incubated with a different complementary strand for an hour. An additional complementary oligo (also at 50 nM) with a distinct dye color was added at this step as a reference marker. The same reference marker was used in all twelve wells. The wells were then rinsed with 3 % BSA/PBS, the PDMS was peeled off, and the slide was rinsed with 1x PBS followed by DI water, then airgun dried. The slide was then scanned using a fluorescent microarray scanner to determine if more than one of the twelve spots fluoresced, suggesting cross-talk. If this occurred, the sequence assayed would be considered insufficiently orthogonal to the rest of the panel and would be replaced by a different sequence.

Our lab has previously validated a set of 12 orthogonal oligos, whose sequences (not including the 20-mer polyA tail) are shown below:

A	ATCCTGGAGCTAAGTCCGTA	A'	TACGGACTTAGCTCCAGGAT
B	GCCTCATTGAATCATGCCTA	B'	TAGGCATGATTCAATGAGGC
C	GCACTCGTCTACTATCGCTA	C'	TAGCGATAGTAGACGAGTGC
i	ATGGTCGAGATGTCAGAGTA	i'	TACTCTGACATCTCGACCAT
ii	ATGTGAAGTGGCAGTATCTA	ii'	TAGATACTGCCACTTCACAT
iii	ATCAGGTAAGGTTCACGGTA	iii'	TACCGTGAACCTTACCTGAT
iv	GAGTAGCCTTCCCGAGCATT	iv'	AATGCTCGGGAAGGCTACTC
v	ATTGACCAAACTGCGGTGCG	v'	CGCACCGCAGTTTGGTCAAT
vi	TGCCCTATTGTTGCGTCGGA	vi'	TCCGACGCAACAATAGGGCA
vii	TCTTCTAGTTGTCGAGCAGG	vii'	CCTGCTCGACAACTAGAAGA
viii	TAATCTAATTCTGGTCGCGG	viii'	CCGCGACCAGAATTAGATTA
ix	GTGATTAAGTCTGCTTCGGC	ix'	GCCGAAGCAGACTTAATCAC

The first 3 sequences (A, B, C) can serve as the anchor sequences, as follows:

2X A-3'-polyA

ATCCTGGAGCTAAGTCCGTAAAAAAAAAAAAAAAAAAAAATCCTGGAGCTAAGTCCGTAAAAAAAAAAAAAAAAAAAA

2X B-3'-polyA

GCCTCATTGAATCATGCCTAAAAAAAAAAAAAAAAAAAAGCCTCATTGAATCATGCCTAAAAAAAAAAAAAAAAAAAA

2X C-3'-polyA

GCACTCGTCTACTATCGCTAAAAAAAAAAAAAAAAAAAAGCACTCGTCTACTATCGCTAAAAAAAAAAAAAAAAAAAA

The complements to the anchors and the 9 remaining sequences can then be coupled together as follows:

A'-i TACGGACTTAGCTCCAGGATAAAAAAAAAAAAAAAAAAAAATGGTCGAGATGTCAGAGTA
B'-ii TAGGCATGATTCAATGAGGCAAAAAAAAAAAAAAAAAAAAATGTGAAGTGGCAGTATCTA
C'-iii TAGCGATAGTAGACGAGTGCAAAAAAAAAAAAAAAAAAAAATCAGGTAAGGTTCACGGTA
A'-iv TACGGACTTAGCTCCAGGATAAAAAAAAAAAAAAAAAAAAGAGTAGCCTTCCCGAGCATT
B'-v TAGGCATGATTCAATGAGGCAAAAAAAAAAAAAAAAAAAAATTGACCAAACTGCGGTGCG
C'-vi TAGCGATAGTAGACGAGTGCAAAAAAAAAAAAAAAAAAAAATGCCCTATTGTTGCGTCGGA
A'-vii TACGGACTTAGCTCCAGGATAAAAAAAAAAAAAAAAAAAAATCTTCTAGTTGTCGAGCAGG
B'-viii TAGGCATGATTCAATGAGGCAAAAAAAAAAAAAAAAAAAAATAATCTAATTCTGGTCGCGG
C'-ix TAGCGATAGTAGACGAGTGCAAAAAAAAAAAAAAAAAAAAGTGATTAAGTCTGCTTCGGC